UNIVERSITAT POLITÈCNICA DE VALÈNCIA

DEPARTAMENT DE COMUNICACIONS

Apodized Coupled Resonator Optical Waveguides: Theory, design and characterization

Ph.D. THESIS

by
José David Doménech Gómez

Valencia, July 2013

UNIVERSITAT POLITÈCNICA DE VALÈNCIA

DEPARTAMENT DE COMUNICACIONS

Apodized Coupled Resonator Optical Waveguides: Theory, design and characterization

José David Doménech Gómez
Optical and Quantum Communications Group.
iTEAM Research Institute
Universitat Politècnica de València.
Camí de Vera s/n, 46022 Valencia, SPAIN
jodogo@iteam.upv.es

Ph.D. Supervisors:
Dr. Pascual Muñoz Muñoz
Prof. José Capmany Francoy

Valencia, July 2013

To my family and friends.
In loving memory of Basilio.

La verdadera ciencia enseña,
sobre todo, a dudar y a ser ignorante.
Ernest Rutherford

Agradecimientos

En primer lugar mis agradecimientos van dirigidos al grupo de investigación en el que he realizado esta tesis doctoral. El grupo de comunicaciones ópticas y cuánticas de la Universidad Politécnica de Valencia. En este grupo no solo he conocido a grandes profesionales sinó a grandes personas y amigos. Tambien querria dar las gracias a mi co-director de tesis y director del grupo de investigación el catedrático José Capmany por la oportunidad que me ha brindado de formar parte de tan prestigioso grupo así como por su apoyo durante la realización de esta tesis.

Un agradecimiento muy especial va dirigido a la persona que me introdujo en el mundo de las comunicaciones ópticas allá por el año 2006, el Dr. Pascual Muñoz. El ha sido director y en gran parte responsable de todos mis logros académicos, desde el proyecto final de carrera, la tesina de master hasta finalmente esta tesis doctoral. Para mi no solo ha sido un mentor en el ámbito profesional sinó que a lo largo de los años también se ha convertido en un amigo más.

No querría dejar de agradecer también a toda mi familia por el apoyo que me han prestado a lo largo de todos estos años. A mis padres, hermanos, tios, primos, que siempre creyeron en mi y me lo demostraron día tras día. Por supuesto tambien he de agradecer a todos los amigos que me animaron a continuar con la investigación aunque a muchos de ellos no les quedara nunca claro a que me dedicaba en la universidad. Por último querría agradecer muy especialmente a mi mujer Alicia ya que sin ella nada de esto habría sido posible. Además de estar al pie del cañon durante todo este tiempo me ha dado lo más grande que me ha pasado en toda mi vida: nuestro hijo David.

Abstract

In this thesis we propose the apodization or windowing of the coupling coefficients of the unit cells conforming a coupled resonator device as a mean to improve the spectral response of these filters. In the same way, we have developed a synthesis algorithm for CROW devices, that given an objective response yields the coupling constants for every resonator within the array. We also have introduced a novel technique for the apodization of coupled resonator structures by applying a longitudinal offset between resonators in order to set the appropriate power coupling constant for obtaining a targeted response, which alleviates the technical requirements required for the production of these devices. We have demonstrated the design, fabrication and characterization of CROW structures employing the apodization through the aforementioned technique in Silicon-On-Insulator technology and validated the theoretical predictions. Lastly, we have explored the delay and phase characteristics of CROW devices and introduced a novel architecture for microwave signal processing in beamforming networks employing resonators as phase-shifting sections.

Resumen

En esta tesis, proponemos la apodización o enventanado de los coeficientes de acoplo de cada uno de los resonadores que conforman los dispositivos de múltiples cavidades resonantes acopladas con tal de reducir el nivel de los lóbulos secundarios en el caso de la configuración SCISSOR o el rizado en la banda pasante, presente en la configuración CROW. De la misma manera, hemos desarrollado un algoritmo de sintesis de dispositivos CROW en el que, dada una respuesta objetivo, obtenemos las constantes de acoplo necesarias para cada resonador del dispositivo. También hemos introducido una técnica novel para implementar la apodización de estructuras basadas en anillos resonantes acoplados mediante la aplicación de un offset longitudinal entre los resonadores con tal de modificar las contantes de acoplo de las cavidades, lo cual alivia los requerimientos técnicos para la fabricación de estos dispositivos. Hemos demostrado el diseño, fabricación y caracterización de estructuras CROW empleando la apodización a través de la técnica mencionada anteriormente en tecnologia de Silicon-On-Insulator (SOI) y validado las predicciones teóricas. Por último, hemos explorado las características de retardo y fase de los dispositivos CROW e introducido una nueva arquitectura para el procesamiento de señales de microondas en redes de conformado de haz empleando resonadores como elementos desfasadores.

Resum

En aquesta tesi, proposem l'apodització dels coeficients d'acoble de cada un dels ressonadors que conformen els dispositius de múltiples cavitats ressonants acoblades amb tal de reduir el nivell dels lòbuls secundaris en el cas de la configuració SCISSOR o l'arrissat en la banda passant, present en la configuració CROW. De la mateixa manera, hem desenrotllat un algoritme de síntesi de dispositius CROW en el que, donada una resposta objectiu, obtenim les constants d'acoble necessàries per a cada ressonador del dispositiu. També hem introduït una tècnica novell per a implementar l'apodització d'estructures basades en anells ressonants acoblats per mitjà de l'aplicació d'un òfset longitudinal entre els ressonadors amb tal de modificar les constants d'acoble de les cavitats, la qual cosa alleuja els requeriments tècnics per a la fabricació d'estos dispositius. Hem demostrat el disseny, fabricació i caracterització d'estructures CROW emprant l'apodització a través de la tècnica mencionada anteriorment en tecnologia de Silicon-On-Insulator (SOI) i validat les prediccions teòriques. Per ultim, hem explorat les caracteristiques de retard i fase dels dispositius CROW i introduït una nova arquitectura per al processament de senyals de microones en xarxes de conformat de feix emprant ressonadors com a elements desfasadors.

List of Acronyms

AFM Atomic Forces Microscope

APRR All-Pass Ring Resonator

AWG Arrayed Waveguide Grating

BB Building Block

BOX Buried Oxide

BPM Beam Propagation Method

CCTV Closed Circuit Television

CIFS Coupling Induced Frequency Shift

CMOS Complementary Metal Oxide Semiconductor

CROW Coupled Resonator Optical Waveguide

DBP Delay-Bandwidth Product

DBR Distributed Bragg Reflector

DC Directional Coupler

DE Deeply Etched

DSA Digital Serial Analyzer

DUT Device Under Test

DUV Deep Ultra Violet

EBL Electron Beam Lithography

EDFA Erbium Doped Fiber Amplifier

EM Electromagnetic

FBG Fiber Bragg Grating

FDTD Finite Differences in the Time Domain

FESEM Field Emission Scanning Electron Microscope

FOV Field Of View

FSR Free Spectral Range

FWHM Full Width Half Maximum

GB Gygabyte

GC Grating Coupler

GNU GNU is Not Unix

GPL General Public License

HPC High Performance Computing

ICP-RIE Inductively Coupled Plasma - Reactive Ion Etching

IDFT Inverse Discrete Fourier Transform

IIR Infinite Impulse Response

imec Interuniversity Microelectronics Centre

IMWP Integrated Microwave Photonics

LCD Liquid Crystal Display

MB Megabyte

MFLOPS Mega Floating Point Operations Per Second

MIT Massachusetts Institute of Technology

MPI Message Passing Interface

MPW Multi Project Wafer

MWP Microwave Photonics

MZI Mach Zehnder Interferometer

MZM Mach Zehnder Modulator

ODL Optical Delay Lines

OTS Optical Transmission System

PIC Photonic Integrated Circuit

PRBS Pseudo Random Binary Sequence

RF Radio Frequency

RR Ring Resonator

SCISSOR Side Coupled Integrated Spaced Sequence Of Resonators

SDH Synchronous Digital Hierarchy

SEM Scanning Electron Microscope

SH Shallowly Etched

SOA Semiconductor Optical Amplifier

SOI Silicon On Insulator

SSB Single Side Band

TE Transverse Electric

TM Transverse Magnetic

TMM Transfer Matrix Method

WDM Wavelength Division Multiplex

Contents

List of Figures

List of Tables

Chapter 1
Introduction

1.1 Background

Photonic technologies are enabling multiple applications nowadays, from fiber optic telecommunications, to biomedical devices and precise fibre sensors. Still, optical components like lenses or fibers tend to be bulky and expensive, and require complex stabilization and adjustments, especially when interfacing with electronics. Embedding some photonic functionalities into an integrated chip can solve most of these issues and dramatically decrease its costs when scaling up production. However, the cutting edge optical manufacturing technologies enabling such chip integration have been traditionally affordable only by large corporations due to the large investment required. Nowadays, generic photonic integration emerges as a new paradigm that provides cost-effective and high-performance miniaturized optical systems for a wide range of applications and markets. However, the state-of-the-art of integrated optics is still far behind its electronic counterpart. Today, only a few basic devices are commercially available. Though, there exists a growing interest in the development of integrated optical devices with increasing complexity.

Specifically, in optical filtering applications one can find integrated devices like Mach-Zehnder Interferometers (MZI) [1], Array Waveguide Gratings (AWG) [2], Fabry-Perot filters [1] and ring resonators [3]. This doctoral thesis focus its body of research on the integration of the latter, from a design and fabrication point of view. The field of guided-wave optical devices incorporating such resonator and microresonator cavities [4] has experienced a considerable increase in the quantity and quality of research contributions over the last ten years.

Ring resonators are devices that provide compact, narrow band and large free spectral range optical periodical band pass/rejection filters. The resonator's response is periodic in frequency and the frequency spanning a single period is named free spectral range (FSR), which is inversely related to the round trip time T within the resonator. The basic ring resonator configuration is the one depicted

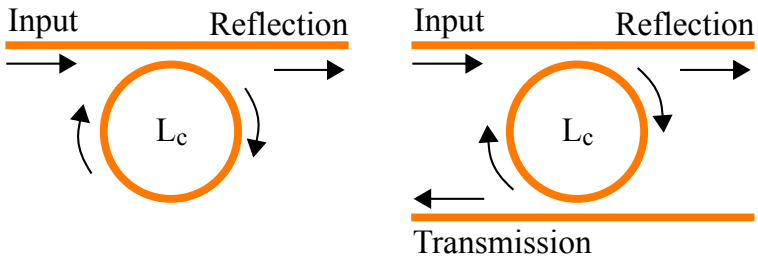

(a) (b)

Figure 1.1: Schematic description of a single (a) and dual-bus (b) coupled microring resonator. L_c represents the cavity length.

in Fig. 1.1-a and is a single bus coupled ring resonator, also called all-pass ring resonator [5]. It is a two port structure and the ports are labelled as *input* and *reflection* in the Fig. 1.1-a. Another configuration widely employed is the dual-bus coupled ring resonator also called add-drop configuration represented in Fig. 1.1-b. It is a four-port device where typically only three ports are used: the input, the transmission and the reflection ports. By cascading serially or in parallel a number of microring resonators, more complex structures can be formed known as coupled resonators. Devices composed of single or multiple ring resonator cavities can be exploited in a wide variety of classical applications including, among others: channel filtering in WDM systems [6], microwave signals processing [7], linear and nonlinear digital optics [8], optical buffering [9], modulation [10], dispersion compensation [11] and switching [12]. Furthermore, their range of applications is currently being extended to encompass the emergent field of quantum information processing [4].

Amongst the devices composed of multiple resonators there are two configurations of special interest for filtering applications. The first one is the so-called Side Coupled Integrated Spaced Sequence Of Resonators (SCISSOR) configuration [13], shown in Fig. 1.2-a, where the resonators are not mutually coupled but are periodically coupled to two side waveguides. Their operation is similar to that of distributed feedback filters. The second configuration is known as the Coupled Resonator Optical Waveguide (CROW) configuration [14], where the rings are mutually coupled in a linear cascade and the array is coupled to an input and output bus waveguides as shown in Fig. 1.2-b. In this case, the operation resembles to a stack of dielectric mirrors. In both cases, they can be treated as Infinite Impulse Response (IIR) filters [15] and design techniques similar to the ones used in digital signal processing can be employed.

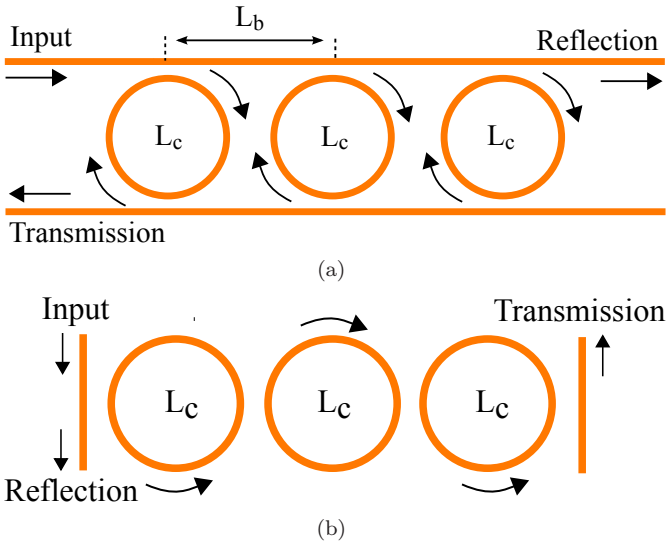

Figure 1.2: Schematic view of a SCISSOR (a) and a CROW (b).

1.2 Fabrication technologies

Multiple material technologies have been used along the years to achieve optical integration into a monolithic chip, each of them more suited for a certain type of devices: lithium niobate for modulators [16], silica (also known as planar lightwave circuit, PLC) for passive devices like couplers [17], splitters [18], gratings [19] and AWGs [20], or indium phosphide for active components like amplifiers, lasers and photodetectors, as well as other passive devices (couplers and filters) [21]. While all these technologies have been researched and already taken intro production since approximately 20 years ago [22], it is silicon photonics that has gained a lot of interest now, due to the opportunity of implementing it into semi-standard complementary metal oxide semiconductor (CMOS) processes, with the large cost reductions this implies, and the corresponding increase in production volumes, system scalability and complexity. Moreover, this also allows for an easier integration of silicon photonic components along with electronic control functions [23]. There are currently several international photonic foundries offering their services through stand alone, dedicated wafer runs, or as part of what is known as multi-project wafer runs (MPW), where wafer space is shared among multiple users to decrease cost, at the expense of a tight fabrication schedules. Process standardization has allowed for a business ecosystem that is quickly evolving to mimic that of the electronics world, where end users and independent design houses alike submit their chip designs to generic foundries. A summary of the generic Photonic Integrated Circuit (PIC) platforms, with operational and technical details, is given in Fig. 1.3. The table contains platforms supplying MPW, shared

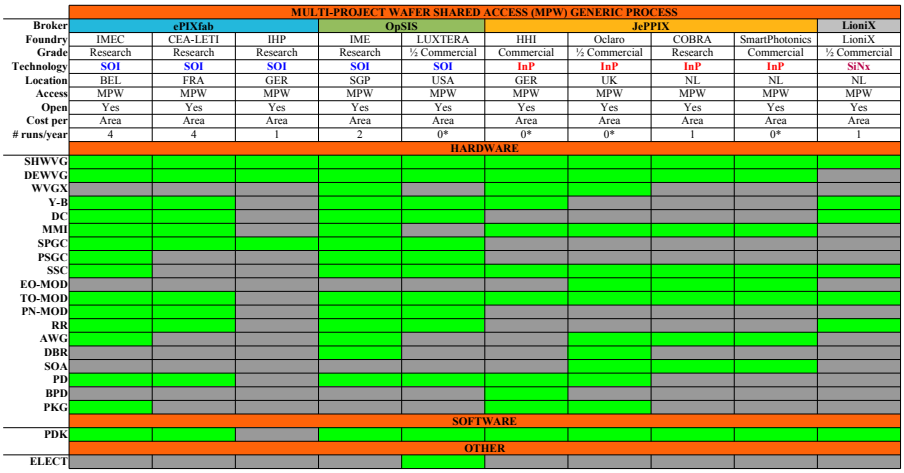

Figure 1.3: Generic foundries matrix. Color code: Green=Available / Possible, Grey=Not Available / Possible. Abbreviations, organization: 0* runs not yet issued, planned within 2013. Abbreviations, technology: SHWVG Shallow waveguide, DEWVG Deeply etched waveguide, WVGX Waveguide crossing, Y-B Y-branch, DC Directional coupler, MMI Multi-Mode Interference coupler, SPGC Single Polarization Grating Coupler, PSGC Polarization Splitting GC, SSC Spot-Size Converter, EO-MOD Electro-Optic Modulator, TO-MOD Thermo-Optic Modulator, PN-MOD PN Junction Modulator, RR Ring Resonator, AWG Arrayed Waveguide Grating, DBR Distributed Bragg Reflector, SOA Semiconductor Optical Amplifier, PD Photo-Detector, BPD Balanced PD, PKG Packaging, PDK Photonic Design Kit, ELECT Merge with Electronics.

fabrication access to a frozen generic process. The MPW platforms are usually accessed through a broker umbrella organization, such as ePIXfab [24] and OpSIS [25] for Silicon photonics and JePPIX [26] for InP photonics. Nonetheless, LioniX [27] for SiNx (TriPleX ^{TM}) technology is an independent company doing the brokering and fab itself. Under the brokering organization, several fabs may exists, supplying research, semi-commercial or commercial grade services. Note that Silicon photonics offers significantly a bigger number of runs per year than the two other technologies. The color matrix in Fig. 1.3 shows the available, or possible, photonic building blocks within each platform. There is a variety of tools for designers, the Photonic Design Kits (PDK), available in most of the platforms. PDK's allow to perform in a, ideally seamlessly, integrated software environment both the photonic simulation and the mask layout, incorporating photonic process information from the foundries. The tools by PhoeniX Software [28] are the de facto standard in Europe. Other platforms as OpSIS use a mix of software packages and tools from different suppliers to cover the full design and manufacturing tool chain. In the latter case, the communication between designers and fab is at the layout file (GDS) level. Finally, back-end processes as packaging are being

offered as well by some of the brokers and foundry players, as ePIXfab and JePPIX. The packages developed are generic as well, hence there are fixed locations for the input/output RF and optical connections, which may well constrain the design. However the advantage is packaging can be reused amongst very different PIC designs, minimizing non-recursive engineering costs.

The devices presented in this work have been fabricated in MPW runs through the SOI ePIXfab platform. ePIXfab offers prototyping access to silicon photonic integrated circuits technologies to fabless customers, and promotes the take-up of silicon PIC technology. In this way, it plays a vital role in bringing silicon photonics from research to the market. ePIXfab is funded by the European Union and started as a collaboration between imec [29] in Belgium and CEA-LETI [30] in France and lately IHP [31] in Germany was incorporated to the consortium.

The refractive index contrast between Silicon ($n_{Si} = 3.5$) and Silica ($n_{SiO2} = 1.46$) is $\Delta n = 1.4$. Due to the high index contrast, waveguides with small cross-section and high confinement can be fabricated. This high confinement allows for ultra-reduced bending radius. Sharp bends have two advantageous effects: a dramatic scaling of the device footprint that enables high density integration on a single chip and a very broad maximum achievable free spectral range, that enables the realization of filters with both large bandwidth and high selectivity. Another reason for the election of this technology was that by the time this thesis was conducted, the SOI platform was one of the most accessible technologies for fabless people in terms of price and schedule.

1.3 Objectives

The thesis presented has three objectives:

1. To develop the theory describing the operation (analysis) and the procedure to design (synthesis) and optimize (apodization) the SCISSOR and CROW filters response.

2. To propose design techniques that account for and overcome manufacturing limitations.

3. To fabricate and demonstrate experimentally the devices to validate the developed theory.

1.4 Contents

This thesis is structured in the following chapters:
Chapter 2 provides the framework and formulation employed to describe the unit cells as well as the final devices in both configuration of coupled resonators reported: the side-coupled integrated spaced sequence of resonators (SCISSOR) and the coupled resonator optical waveguides (CROW). The formalism employed for the analysis will be the transfer matrix method (TMM). Next, a technique for

improving the spectral response of both configurations through the apodization of the coupling constants of the devices will be introduced. Then, an analysis of several apodized and non-apodized SCISSOR and CROW devices will be reported. To conclude the chapter, a novel synthesis method based in the layer aggregation algorithm will be described in detail.

Chapter 3 reports a novel technique for setting the coupling constants in the SCISSOR and CROW structures. This technique is employed to overcome the technological limitations on the fabrication processes when manufacturing coupled resonator devices. The formulation and the main advantages of the technique are reviewed in detail. To conclude the chapter, an extensive sensitivity analysis through simulations is introduced.

Chapter 4 presents the design, fabrication and characterization of CROW devices in Silicon-On-Insulator (SOI) technology, making use of the techniques introduced in previous chapters. The design process is described step by step from the basic constituent components, referred as building blocks (BB), to the final CROW device. The fabrication process employed as well as the foundry and access mechanism to the same are also introduced. To conclude, the results of two fabrication runs will be discussed in detail.

Chapter 5 discusses two specific applications implemented with the fabricated devices. The first one is the use of CROWs as optical buffers and their main drawbacks. The main application shown is a microwave photonic beamforming network based in ring resonators. The principle of operation of the beamformer as well as the formulation employed are introduced. Then the fabrication and characterization of a basic beamforming network is reported.

Finally, in **Chapter 6** conclusions about the results achieved in the present work and considerations on future work are presented.

Chapter 2

Serial and parallel coupled resonator optical waveguides

2.1 Introduction

In this chapter the modelling of coupled resonator structures introduced in Chapter 1 is presented. Firstly, a transfer matrix method (TMM) model is developed to analyze these structures, assuming the coupling coefficients are all equal. Secondly, the theoretical modelling, and response is given, for different coupling coefficients within one SCISSOR/CROW. The last part of the chapter is devoted to the development of techniques in which the filter response can be improved. These techniques consist on the adjustment of the coupling coefficients between the resonators, and are commonly known as apodization in optics, or windowing in signal processing. The apodization is employed in SCISSOR structures as a means to reduce the level of secondary sidelobes and in CROW structures to reduce the passband ripples. This technique is regularly employed in the design of digital filters [32] and has been applied as well in the design of other photonic devices such as corrugated waveguide filters [15] and fiber Bragg gratings [33]. On the other hand, a novel synthesis algorithm for CROW structures which is based on the layer aggregation technique [34] previously proposed for the synthesis of fiber Bragg grating filters is presented. In this case the filter is reconstructed by successive cavity aggregations. Starting from the frequency transfer function, the method yields the coupling constants between the resonators. The convergence of the algorithm developed is examined and the related parameters discussed.

2.2 Transfer Matrix Method model of coupled resonator structures

The analysis of coupled resonator structures with the Transfer Matrix Method (TMM) [6] provides a flexible and device-independent way to calculate the transfer functions of these compound devices, and allows to solve complex structures concatenating basic ones without solving a high number of equations. Another advantage of this method is that it can be easily implemented as a computer program. Coupled resonator devices can be decomposed in small sections that can be modelled by simpler transfer matrices. In the next subsections, the transfer matrices of the basic building blocks forming a coupled resonator will be derived.

2.2.1 Directional coupler

The first basic building block introduced is the directional coupler [35]. The couplers are based in the exchange of power between guided modes of adjacent waveguides that in this case will be formed between rings or either between a ring and a bus waveguide. Figure 2.1 shows the nomenclature employed for the travelling waves in a coupler.

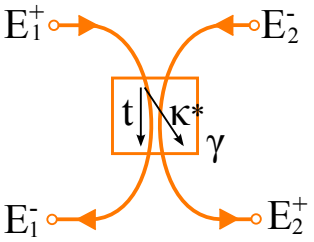

Figure 2.1: Schematic description of travelling waves in a coupler. The direct and cross coupling coefficients are t and κ respectively. The losses in the coupler are represented by γ.

E_i^k will designate the frequency domain electric field amplitude, where $i = 1, 2$, will represent the port location with respect to the system (1 for ports located at the left part of the system, and 2 for ports located at the right part of the system), and k $= +, -$ will represent the field's direction of propagation (+ for right going waves, and - for left going waves). The equations that describe the coupler are [36]:

$$\begin{bmatrix} E_1^- \\ E_2^+ \end{bmatrix} = \begin{bmatrix} t & \kappa \\ -\kappa^* & t^* \end{bmatrix} \cdot \begin{bmatrix} E_1^+ \\ E_2^- \end{bmatrix} \tag{2.1}$$

where t is the direct-coupled coefficient and κ is the cross-coupled coefficient. The asterisk in t^* and in κ^* represents the complex conjugate. Equation 2.1 relates the input and output fields, but they can be rearranged in such a way so that the

fields in the right part of the coupler are related to the fields in the left part by:

$$\begin{bmatrix} E_2^+ \\ E_2^- \end{bmatrix} = [P] \cdot \begin{bmatrix} E_1^+ \\ E_1^- \end{bmatrix} \tag{2.2}$$

$$[P] = \frac{1}{\kappa} \cdot \begin{bmatrix} -\gamma & t^* \\ -t & 1 \end{bmatrix} \tag{2.3}$$

where

$$\begin{aligned} t &= \sqrt{1-K} \\ k &= j \cdot \sqrt{(K)} \end{aligned} \tag{2.4}$$

$$\gamma = |t|^2 + |\kappa|^2 \tag{2.5}$$

with K being the power coupling ratio of the coupler and γ the coupler excess losses.

2.2.2 The waveguides

A waveguide can be modelled as a two port device (Fig. 2.2-(a)) where the fields at the input and at the output are related through the equation:

$$E_1^+ = E_2^+ \cdot e^{\alpha L_a} \cdot e^{-j\beta L_a} \tag{2.6}$$

where α represents the power propagation loss of a waveguide in Np/m and β the propagation constant. L_a is the waveguide length. The propagation of the fields in the waveguide imply attenuation and a phase change proportional to the length of the waveguide. For the devices reported in this work, another useful basic element is a four port device conformed by two waveguides as depicted in Fig. 2.2-(b).

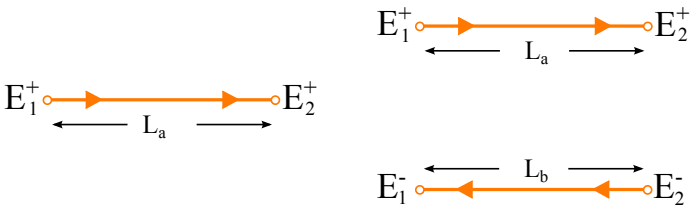

Figure 2.2: Schematic description of travelling waves in a 2 port waveguide channel (a) and in a 4 port waveguide channel (b). L_x is the total length of each section.

The fields in the four port configuration are related through the matrix:

$$\begin{bmatrix} E_1^+ \\ E_1^- \end{bmatrix} = [Q] \cdot \begin{bmatrix} E_2^+ \\ E_2^- \end{bmatrix} \tag{2.7}$$

where

$$[Q] = \begin{bmatrix} e^{\alpha L_a} \cdot e^{-j\beta L_a} & 0 \\ 0 & e^{-\alpha L_a} \cdot e^{j\beta L_b} \end{bmatrix} \tag{2.8}$$

β is the waveguide propagation constant and L_a and L_b the waveguide's length.

2.2.3 Ring resonator

The model of a ring resonator can be described by the combination of two couplers joined by a couple of waveguides as depicted in Fig. 2.3:

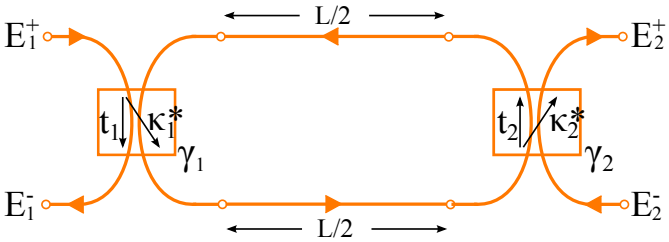

Figure 2.3: Schematic description of travelling waves in a ring resonator. This structure is obtained by a coupled concatenation of a coupler, a four-port waveguide channel and finally another coupler.

All-pass ring resonator

The well known all-pass ring resonator configuration [11] can then be modelled as a concatenation of two matrices: P and Q. In this case the last coupler is removed and the upper waveguide is connected directly to the lower waveguide. The ring resonator perimeter is defined as L. Therefore each branch of the four-port waveguide channel should have a length $L_a = L/2$ and $L_b = L/2$. The relationship of the fields at the input and at the output is given by:

$$[T] = [P \cdot Q] = \frac{1}{\kappa} \cdot \begin{bmatrix} -\gamma \cdot e^{\alpha \frac{L}{2}} \cdot e^{\frac{-j\beta L}{2}} & t^* \cdot e^{-\alpha \frac{L}{2}} \cdot e^{\frac{j\beta L}{2}} \\ -t \cdot e^{\alpha \frac{L}{2}} \cdot e^{\frac{-j\beta L}{2}} & e^{-\alpha \frac{L}{2}} \cdot e^{\frac{j\beta L}{2}} \end{bmatrix} \tag{2.9}$$

Dual-bus coupled ring resonator

In this case the matrix describing the resonator is the following:

$$[T] = [P_1 \cdot Q \cdot P_2] \tag{2.10}$$

where P_1 and P_2 correspond to equation 2.3 where κ, t and γ can be different for each coupler.

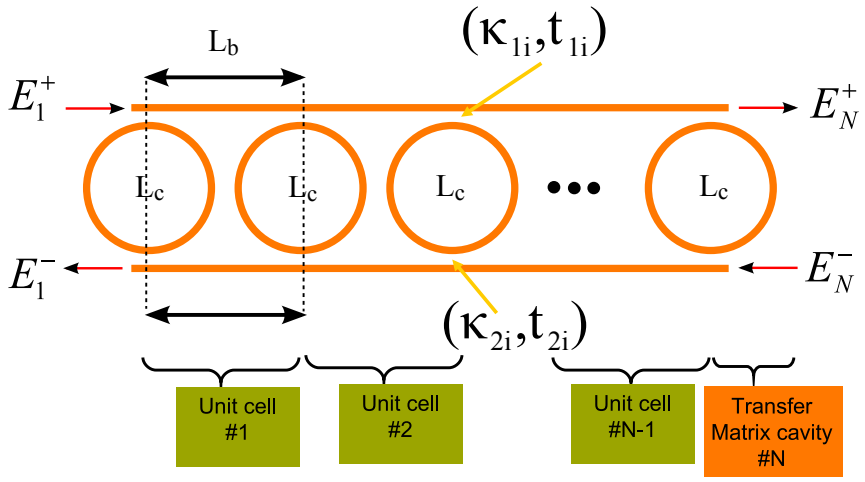

Figure 2.4: SCISSOR structure layout.

2.3 Apodization

2.3.1 Apodized SCISSORs

SCISSORs as defined in [37] are considered. The general structure of the apodized SCISSOR composed of N uncoupled rings with equal length L_c each one coupled to an *in* (upper) and a *drop* (lower) waveguide is shown in Fig. 2.4, where the individual unit cells are identified. Here in each unit cell "i" different coupling values to the *in* and the *drop* waveguides are allowed. Also, the coupling values can change from one cell to another as a result of the apodization. The same nomenclature as that employed in [36] for the cross and direct coupling parameters of each coupling region is followed. Also shown in the figure is the ring separation parameter L_b and the electric field convention employed in the section where the "+" superscript labels the fields propagating from left to right and the "-" superscript labels the fields propagating from right to left.

The transfer matrix method [6] [38] to analyse the structure which is composed on N-1 unit cells and a closing ring cavity is used. The layouts of an arbitrary unit cell and the closing cavity are shown in Fig. 2.5.

The transfer matrices of the arbitrary unit cell M_{UCi} (i=1,2,..N-1) and the closing cavity M_{CN} are given respectively by:

$$M_{UCi} = \frac{1}{R_{2i}} \begin{pmatrix} (R_{1i}R_{2i} - T_{1i}T_{2i})\, e^{j\Delta} & T_{2i}e^{j\Delta} \\ -T_{1i}e^{-j\Delta} & e^{-j\Delta} \end{pmatrix} \tag{2.11}$$

$$M_{CN} = \frac{1}{R_{2N}} \begin{pmatrix} R_{1N}R_{2N} - T_{1N}T_{2N} & T_{2N} \\ -T_{1N} & 1 \end{pmatrix} \tag{2.12}$$

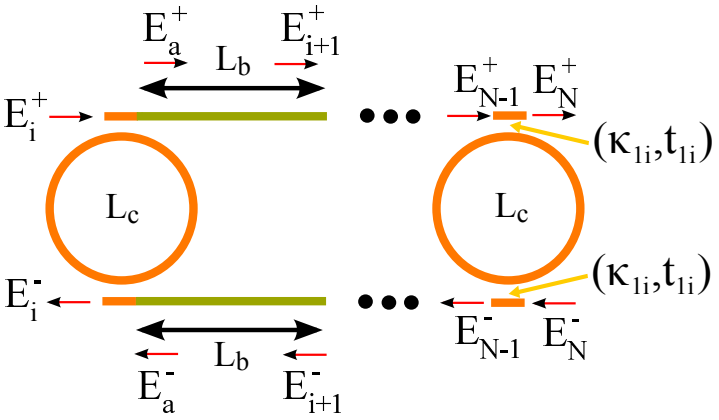

Figure 2.5: SCISSOR unit cell and closing cell.

where:

$$R_{1i} = \frac{t_{1i} - t_{2i}^* \left(|t_{1i}|^2 + |\kappa_{1i}|^2 \right) \tau_i e^{j\delta}}{1 - \tau_i t_{1i}^* t_{2i}^* e^{j\delta}} \tag{2.13}$$

$$R_{2i} = \frac{t_{2i} - t_{1i}^* \left(|t_{2i}|^2 + |\kappa_{2i}|^2 \right) \tau_i e^{j\delta}}{1 - \tau_i t_{1i}^* t_{2i}^* e^{j\delta}} \tag{2.14}$$

$$T_{1i} = -\frac{\kappa_{1i}^* \kappa_{2i} \sqrt{\tau_i} e^{j\delta/2}}{1 - \tau_i t_{1i}^* t_{2i}^* e^{j\delta}} \tag{2.15}$$

$$T_{2i} = -\frac{\kappa_{2i}^* \kappa_{1i} \sqrt{\tau_i} e^{j\delta/2}}{1 - \tau_i t_{1i}^* t_{2i}^* e^{j\delta}} \tag{2.16}$$

and the physical parameters related to the cavity round trip phase shift and losses and the inter-cavity phase shift are given respectively by:

$$\delta = \beta L_c \tag{2.17}$$

$$\tau = e^{(-\alpha L_c)}$$

$$\Delta = \beta L_b \tag{2.18}$$

with α and β representing the waveguide attenuation and propagation constants. The frequency response of the SCISSOR structures is periodic with period δ/π. The overall transfer matrix of the SCISSOR structure is then given by:

$$\begin{pmatrix} E_N^+ \\ E_N^- \end{pmatrix} = \begin{pmatrix} T_{11} & T_{12} \\ T_{21} & T_{22} \end{pmatrix} \begin{pmatrix} E_1^+ \\ E_1^- \end{pmatrix} \tag{2.19}$$

$$M_T = \begin{pmatrix} T_{11} & T_{12} \\ T_{21} & T_{22} \end{pmatrix} = M_{CN} \prod_{i=N-1}^{1} M_{UCi} \tag{2.20}$$

from which the relevant transmission and reflection transfer functions are obtained:

$$T = \left.\frac{E_N^+}{E_1^+}\right|_{E_N^-=0} = \frac{1}{T_{22}} \qquad (2.21)$$
$$R = \left.\frac{E_1^-}{E_1^+}\right|_{E_N^-=0} = -\frac{T_{21}}{T_{22}}$$

The apodization is impressed in this case over the cross-coupled coefficients according to a specified window function [15] [33] $w[i]$ i=0,1,2...N-1. For SCISSOR structures several options are possible: apodizing only the cross coupled coefficients in the *in* bus ($\kappa_{1i} = \kappa w[i]$), apodizing only the cross coupled coefficients in the *drop* bus ($\kappa_{2i} = \kappa w[i]$) or apodizing the cross coupled coefficients in both buses ($\kappa_{1i} = \kappa_{2i} = \kappa w[i]$). In the following the first and third cases are considered and the effects of apodization using standard windowing functions employed in signal processing applications [32] are explored.

The formulation above includes the general case of coupling losses. However, the simulations presented are for the case of a loss-less coupler, where t and κ are related through equations 2.4.

To compare the performance of the different apodization windows one has to choose a reference metric for the effective number of rings of the SCISSOR device. Then one should compare apodized SCISSOR structures with the same number of effective rings. The effective number of rings in the apodised SCISSOR structure is defined by:

$$N_{eff} = N\frac{\sum_{i=0}^{N-1}|i|w[i]}{\sum_{i=0}^{N-1}|i|} \qquad (2.22)$$

The effective number of rings for the apodized SCISSOR in Figs. 2.6, 2.7 and 2.8 is displayed in the upper part of each graph. Obviously, for uniform (i.e non apodized) CROWs N=Neff (in this case Neff=10). In each case, as the apodization parameter is increased the value of Neff decreases.

Fig. 2.6 shows the results obtained for the reflection transfer function when using a Gaussian apodization function in a 10 ring SCISSOR with $L_b = 0.5 \cdot L_c$.

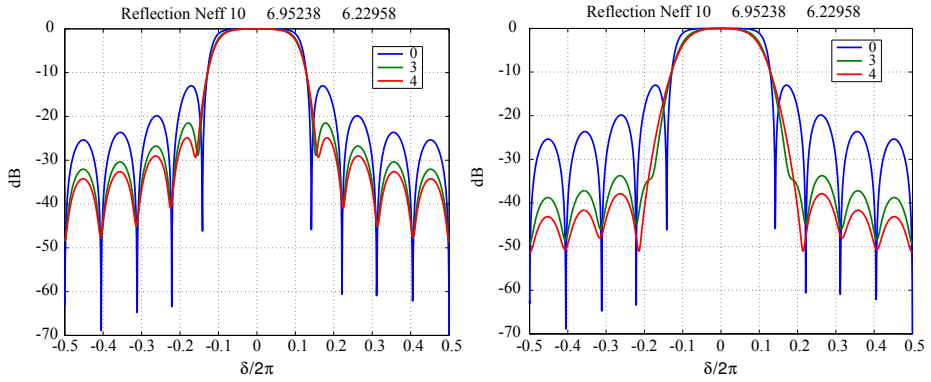

(a) Apodized in 1 bus (b) Apodized in 2 buses

Figure 2.6: SCISSOR reflection transfer function for Gauss window apodization (parameter G=0, 3 and 4) on (a) one bus and (b) two buses

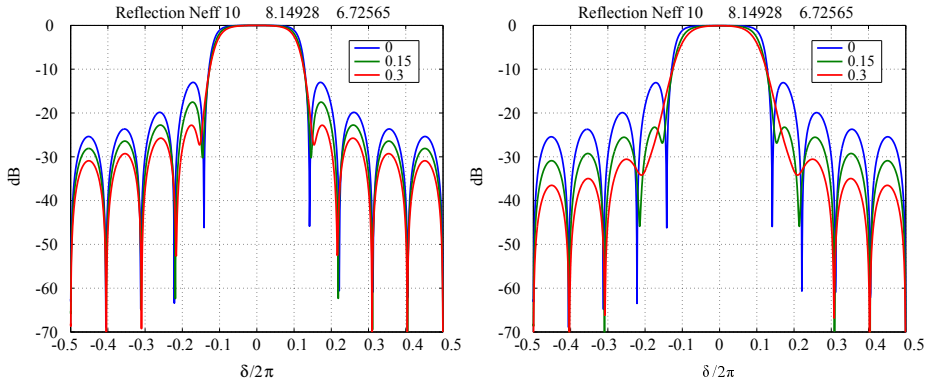

(a) Apodized in 1 bus (b) Apodized in 2 buses

Figure 2.7: SCISSOR reflection transfer function for Hamming window apodization (parameter H=0, 0.15 and 0.3) on (a) one bus and (b) two buses

The apodization window is given by [33]:

$$\begin{aligned} w[i] &= e^{\left(-G\left(\frac{i-N/2)}{N}\right)^2\right)} \\ i &= 0, 1, ..., N-1 \\ K &= 0.1 \\ G &= 0, 3, 4 \end{aligned} \tag{2.23}$$

The left part shows the case of a single bus apodization while the right part illustrates the effect of apodizing both buses.

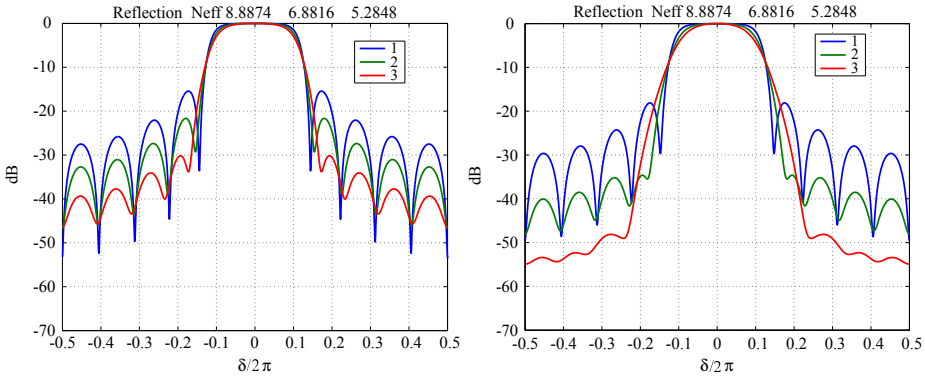

(a) Apodized in 1 bus (b) Apodized in 2 buses

Figure 2.8: SCISSOR reflection transfer function for Kaiser window apodization (parameter β_k=1, 2 and 3) on (a) one bus and (b) two buses

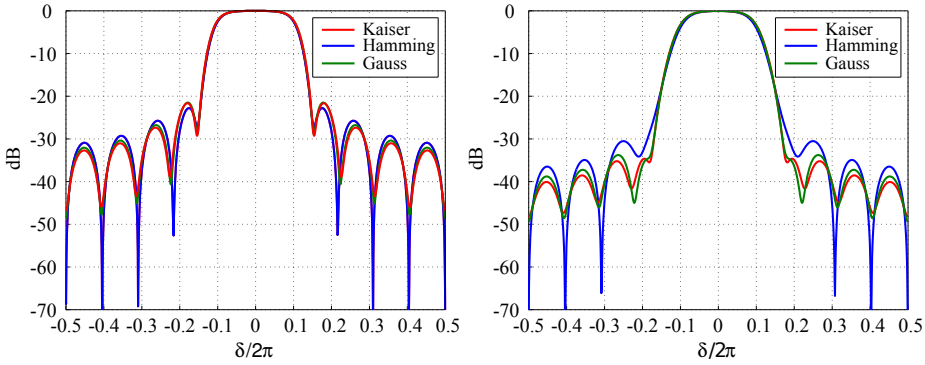

(a) Apodized in 1 bus (b) Apodized in 2 buses

Figure 2.9: SCISSOR reflection transfer comparison for Gauss, Hamming and Kaiser window apodisation (effective number of rings 6.9), on (a) one bus and (b) two buses

The effect of sidelobe reduction due to the apodization of the cross-coupling coefficients can be observed in both cases as compared to the case of no apodization (G=0) which is also depicted in blue colour trace for reference. Higher reductions are obtained for the case where the cross coupled coefficients are apodized in both buses. In fact this result is obtained for all the different apodization windows that have been considered.

For example, in Figs. 2.7 and 2.8 similar results as those of Fig. 2.6 are plotted, when Hamming and Kaiser windowing functions and $L_b = 0.5 \cdot L_c$ are employed.

For the Hamming window [33], the following apodization function is implemented:

$$\begin{aligned} w[i] &= \frac{1 + H\cos(2\pi n)}{1 + H} \\ i &= 0, 1, ..., N-1 \\ K &= 0.1 \\ H &= 0, 0.15, 0.3 \end{aligned} \tag{2.24}$$

where the case H=0 is equivalent to no apodization. Again, sidelobe reduction is observed for both cases with a better performance for the case where the cross coupled coefficients are apodized in both buses. For the Kaiser apodization window [15]:

$$\begin{aligned} w[i] &= \frac{\beta_k}{\sinh(\beta_k)} I_0\left(\beta_k\sqrt{1-4n^2}\right) \\ i &= 0, 1, ..., N-1 \\ n &= [i - N/2]/N \\ K &= 0.1 \\ \beta_k &= 1, 2, 3 \end{aligned} \tag{2.25}$$

Again, sidelobe reduction is observed for both cases with a better performance for the case where the cross coupled coefficients are apodized in both buses. Apparently, the Kaiser window function provides the best performance regarding sidelobe suppression. However, one must be careful when comparing the performance of the different apodization functions as it will now be explained. Apodizing the cross coupling coefficients is in effect equivalent to reducing the number of rings in the SCISSOR device. The argument is equivalent to that provided in [15] to demonstrate that the effective length of an apodized grating is lower than that of an uniform device.

In Fig. 2.9, the performance of the three windows for a SCISSOR device with (N=10), $L_b = 0.5 \cdot L_c$ and the same effective number of rings $Neff = 6.9$ is compared. It can be observed that the performance of the three apodization windows is quite similar when the number of effective rings is the same.

Regarding the delay response, τ_d of the SCISSOR, it can be obtained using the following expression:

$$\frac{\tau_d}{T_c} = -\frac{\partial\phi(\delta)}{\partial\delta} \tag{2.26}$$

where T_c is the round trip time in a single ring and $\phi(\delta)$ is the phase of the reflection response in eq. 2.21. The round trip time of each resonator is related to the perimeter of each section and to the group velocity as:

$$T_c = \frac{L_c}{v_g} \tag{2.27}$$

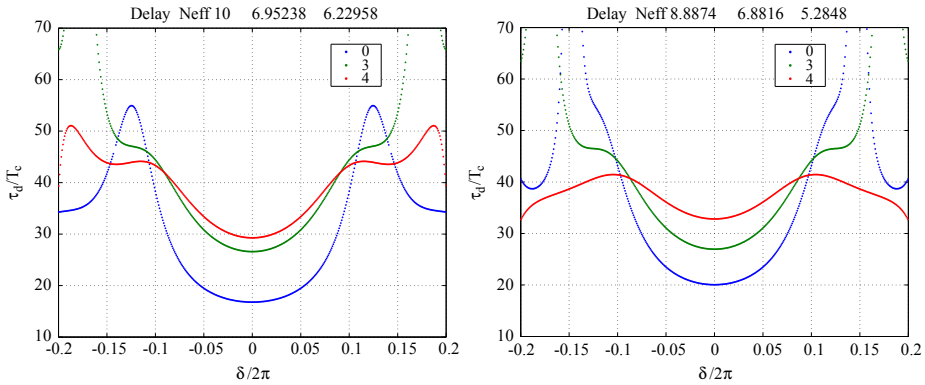

(a) Gauss window, G=0, 3 and 4 (b) Kaiser window, β_k=1, 2 and 3

Figure 2.10: SCISSOR reflection normalised delay for Gauss and Kaiser window apodization

The results are shown in Fig. 2.10 for Gaussian and Kaiser apodization. As expected, more delay on the centre of the pass band is obtained for smaller bandwidth responses, i.e. a bigger degree of apodization, which is in good agreement with resonator theory [39].

2.3.2 Apodized CROWs

In this section, CROWs as defined in [40] are analyzed. The structure consists on a set of coupled rings between two regular waveguides, as shown in Fig. 2.11. An N ring CROW structure is the composed of N-1 unit cells closed by an opening and a closing section which connect them to the input and output waveguides respectively. Figure 2.12 shows the layouts of the unit cell and the input and output closing sections. The unit cell transfer matrix is, using the same symbol convention as above:

$$M_{UCi} = \frac{1}{\kappa_i}\begin{pmatrix} -\tau_i^{1/2}\left(|\kappa_i|^2+|t_i|^2\right)e^{j\delta/2} & t_i^* \\ -t_i & \tau_i^{-1/2}e^{-j\delta/2} \end{pmatrix} \tag{2.28}$$

The matrix corresponding to the input and output coupling sections of the CROW, (Fig. 2.12) opening and closing sections respectively, OS and CS, are the following:

$$M_{OS} = \frac{1}{\kappa_0}\begin{pmatrix} -\left(|\kappa_0|^2+|t_0|^2\right)\tau_0^{1/4}e^{j\delta/4} & t_0^*\tau_0^{1/4}e^{j\delta/4} \\ -t_0\tau_0^{-1/4}e^{-j\delta/4} & \tau_0^{-1/4}e^{-j\delta/4} \end{pmatrix} \tag{2.29}$$

$$M_{CS} = \frac{1}{\kappa_N}\begin{pmatrix} -\left(|\kappa_N|^2+|t_N|^2\right)\tau_N^{1/4}e^{j\delta/4} & t_N^*\tau_N^{-1/4}e^{-j\delta/4} \\ -t_N\tau_N^{1/4}e^{j\delta/4} & \tau_N^{-1/4}e^{-j\delta/4} \end{pmatrix} \tag{2.30}$$

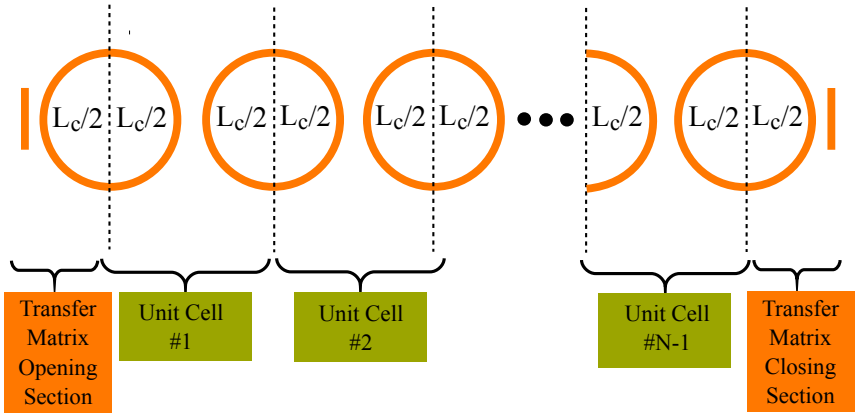

Figure 2.11: CROW structure layout.

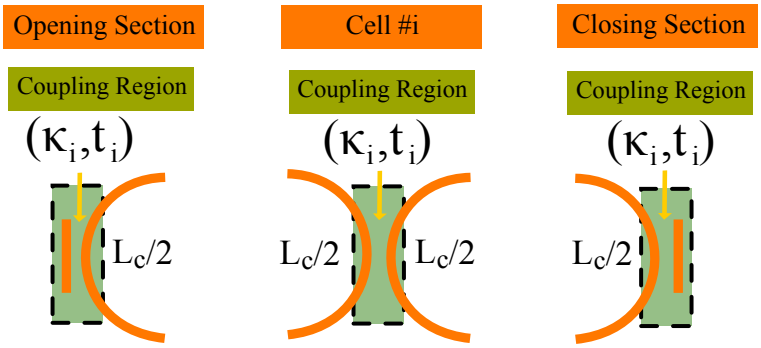

Figure 2.12: CROW unit cell, opening and closing sections.

Hence, the overall transmission and reflection responses can be obtained as for SCISSORs, through equations 2.19 and 2.21, but using the following transfer matrix instead of equation 2.20:

$$M_T = M_{CS}\left[\prod_{i=N-1}^{1} M_{UCi}\right] M_{OS} \tag{2.31}$$

The response of SCISSORs and CROWs are complementary, that is, while for SCISSORs the transmission and reflection from eq. 2.21 are band-reject and band-pass respectively, for CROWs the transmission and reflection are band-pass and band-reject.

In the case of CROWs the apodization is impressed on the direct coupling coefficients, t_i, therefore $t_i = tw[i]$, where the window functions are given by eqs. 2.24- 2.26. The results are shown in Fig. 2.13. The apodization reduces the ripples in the passband, at a cost of an increase in the filter bandwidth. In Fig.

2.13-(a) comparison of the three windowing functions for a fixed effective number of rings, (eq. 2.22), of 6.6 is shown.

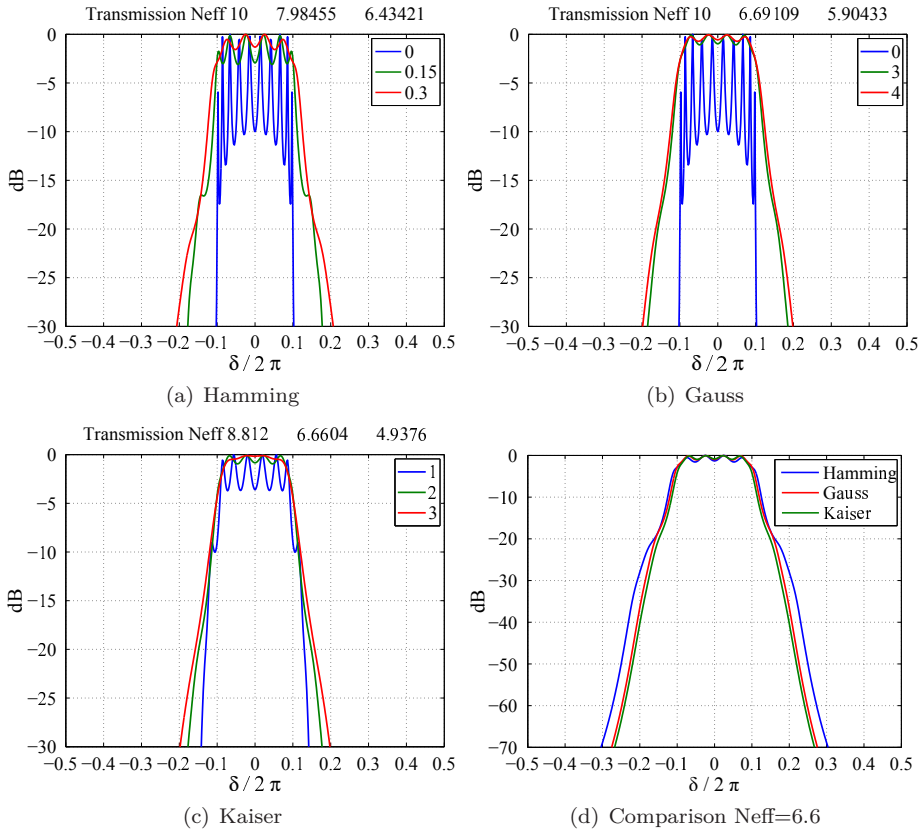

Figure 2.13: CROW transmission transfer function for (a) Hamming, (b) Gauss, (c) Kaiser window apodization (window parameters as in Figs. 3-5) and (d) comparison for an effective number of rings 6.6.

To summarize, the main outcomes of the analysis model have been:

- A TMM model of CROWs and SCISSORs has been developed.
- The apodization of both structures has been analyzed through the TMM model developed.
- A comparison between different apodization windows in terms of bandwidth and group delay has been made.

This model will be used as the basis for all the designs shown in the following chapters.

In the next section, a novel synthesis method for CROWs based in the layer aggregation algorithm will be presented.

2.4 Synthesis of coupled resonator optical waveguides by cavity aggregation

Coupled resonators fell into the category of distributed feedback devices. There is an extensive literature [34, 41–46] related to the synthesis of these devices and, in particular, of layer peeling/aggregation algorithms for fiber and waveguide Bragg gratings [34, 41, 42, 44]. In these devices the scattering of the fundamental mode is produced in a continous way along the entire device length. While these devices have widespread application and advantages, especially in fiber format, it has been recently shown by several researchers [14,37,38,47,48] that coupled resonator optical waveguide (CROW) structures are more suitable for small footprint integrated devices. In CROW devices the scattering of the fundamental mode is produced at discrete locations within the structure in coincidence with the positions of the directional couplers. Several algorithms have been proposed for CROW synthesis including, for instance, those based on Butterworth and Chebyshev responses [49] and those based on the definition of a polynomial whose roots are the zeros of the channel-dropping transmittance characteristic [50].

In this section, a novel synthesis algorithm for CROW structures is proposed. The algorithm is based on the layer aggregation technique [34] previously proposed for the synthesis of fiber Bragg grating filters.

2.4.1 Layer aggregation method

Consider the CROW structure shown in Fig. 2.14-(a). The coupling constant can be equal for all the couplers (uniform CROW) or different by applying a windowing function (apodized CROW) as described in the previous section. For the couplers in Fig. 2.14, Eq. 2.1 is taken and adapted to describe them. A loss-less coupler is assumed hereafter, i.e. $\gamma = |t_i|^2 + |\kappa_i|^2 = 1$. In practical devices, all the resonators have the same perimeter. Hence, the impulse response of the filter is composed of impulses, or samples, of different amplitudes happening at times multiples of the ring resonator round trip time, T_c. In this case it is convenient to use a discrete time notation [32], i.e. $h[n] = h(nT_c)$. The layer aggregation method is based upon the analysis of the filter contributions to the impulse response time samples. The approach followed is similar to that developed for Fiber Bragg gratings in [34]. Referring to Fig. 2.14-(b)(c), at time $n = 0$ the impulse response is solely due to the first coupler of the device, while at time $n = 1$ the response is due to the first two couplers:

$$\begin{aligned} h[0] &= t_0 \\ h[1] &= -t_1|\kappa_0|^2 \end{aligned} \tag{2.32}$$

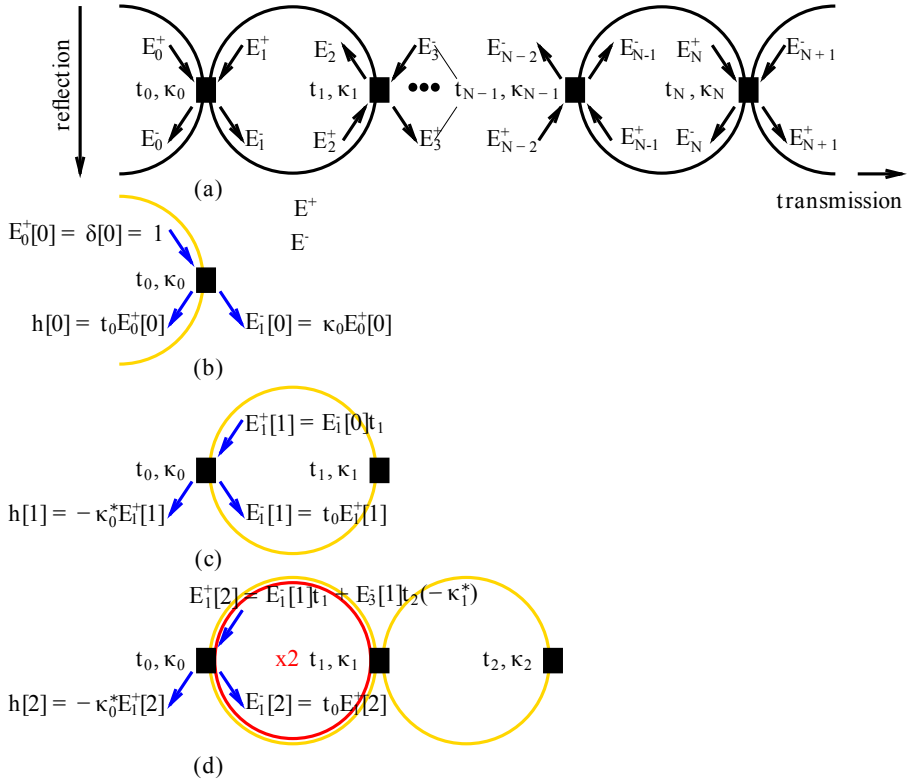

Figure 2.14: CROW (a) naming convention, and layer aggregation for $h[n]$ (b) $n = 0$, (c) $n = 1$ and (d) $n \geq 2$

.

In both cases the paths followed by the light within the CROWs are non-recursive, i.e. a waveguide section of the device is only traversed one time. For $n \geq 2$, $h[n]$ is formed by two contributions, one recursive and one non-recursive, as illustrated in Fig. 2.14-(d) for $n = 2$, with yellow and red lines respectively. In this particular case, the recursive contribution is due to the first resonator (two turns, marked in red as 'x2'), while the non-recursive comes from the direct reflection from coupler number 2. Generalizing, for $n \geq 2$:

$$h[n] = h_r[n] + h_{nr}[n] \tag{2.33}$$

where the recursive part at time n is given by the corresponding sample of the impulse response of the CROW with $n-1$ resonators, and the non-recursive part can be derived from the figures:

$$h_{nr}[n] = (-1)^n t_n \Pi_{i=0}^{n-1} |\kappa_i|^2 \tag{2.34}$$

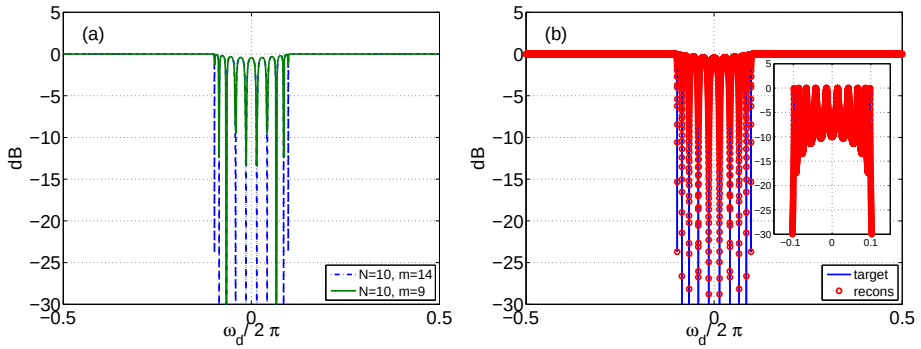

Figure 2.15: CROW (a) target TMM calculated response for $m = 9$ and $m = 14$ and (b) synthesized and target responses (inset transmission response)

2.4.2 Reconstruction procedure

The input for the reconstruction procedure described in this section is the (reflection) transfer function of a uniform, or apodized, CROW. The transfer function can be expressed as a function of the radian frequency normalized by the round trip time, i.e. $H(\omega_d)$ with $\omega_d = \omega T_c$. Hence, $\omega_d \in [0, 2\pi[$. The starting point for the reconstruction is a sampled version of $H(\omega_d)$, $H[k]$ for $k = 0, .., M-1$, where the index k corresponds to the set of discrete frequencies taken from ω_d every $\omega_d/2\pi M$, and M a power of 2, $m = \log_2 M$, to use fast Fourier algorithms. The reconstruction steps are:

1. Given $H[k]$, calculate its inverse discrete Fourier transform, IDFT,$h[n] = \text{IDFT}_M\{H[k]\}$
2. For $n = 0$ and $n = 1$ use eq. (2.32) to solve for (t_0, κ_0) and (t_1, κ_1).
3. For every $n \geq 2$ iterate using the set $\{(t_i, \kappa_i)\}$ $i = 0, ..., n-1$ and the method in [34] to find the impulse response of a CROW with $n-1$ rings, corresponding to $h_r[n]$, and eqs. (2.33)(2.34) to obtain (t_n, κ_n).

2.4.3 Reconstruction results

As a first example, the reconstruction is applied for the target transfer functions corresponding to uniform CROW devices with $K = 0.1$ with $N = 5$ and $N = 10$ rings. The target transfer functions were calculated using the TMM from the previous section. Fig. 2.15-(a) shows the response for $N = 10$ sampled with 2^m points ($m = 9$ and $m = 14$). The coupling constants K_i, $i = 0, ..., N$ obtained through reconstruction are shown in Fig. 2.16-(a)(b), for 5 and 10 rings respectively, for different number of samples in $H(\omega_d)$. The procedure converges when more samples are used, and for smaller M when less rings are used. This can be understood from Fig. 2.15-(a), where the differences in $|H(\omega_d)|$ are shown for

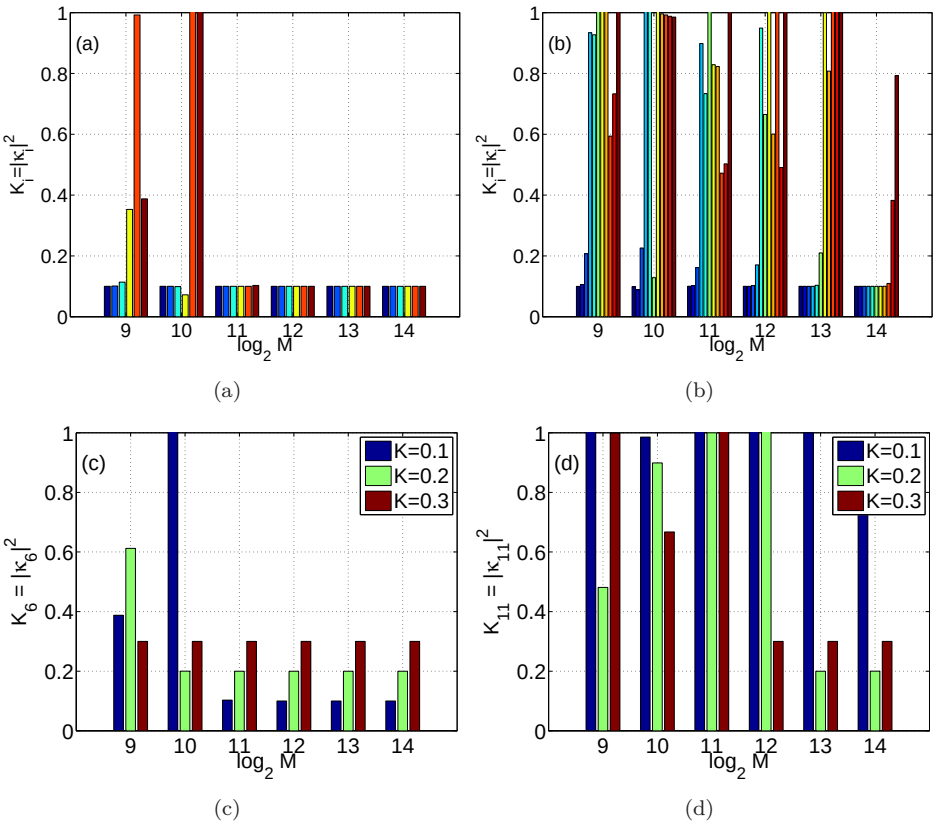

Figure 2.16: Reconstructed K_i values for (a) $N = 5$ and (b) $N = 10$ rings for a uniform CROW with $K = 0.1$ vs. IDFT number of points M used. K_6 (c) and K_{11} (d) for $N = 5$ and $N = 10$ rings uniform CROWs respectively, with K 0.1, 0.2 and 0.3 vs. IDFT number of points M used.

$m = 9$ and $m = 14$. A small number of samples does not reproduce the transitions from peaks to nulls in $|H(\omega_d)|$. The steepness of these transitions is related to K and N, being smoother for bigger K and/or when apodization is used and for smaller number of rings. Therefore, all the results presented are worst case. The differences between samples of $h[n]$, using $m = 9$ and $m = 14$, are of the order of 10^{-4}. Note that all this is ultimately related to eq. (2.34), from which (t_n, κ_n) are calculated for every n, $t_n = (-1)^n(h[n] - h_r[n])/\Pi_{i=0}^{n-1}|\kappa_i|^2$, so the lack of precision when calculating $h[n]$ and $h_r[n]$ using the TMM and the IDFT$_M$, besides the multiplication of small K values in the denominator, can make the reconstruction procedure divergent. The convergence for uniform CROWs with different K values, 0.1, 0.2 and 0.3, is shown in Fig. 2.16-(c)(d) for $N = 5$ and $N = 10$ rings respectively. The graphs show the value of the coupling constant

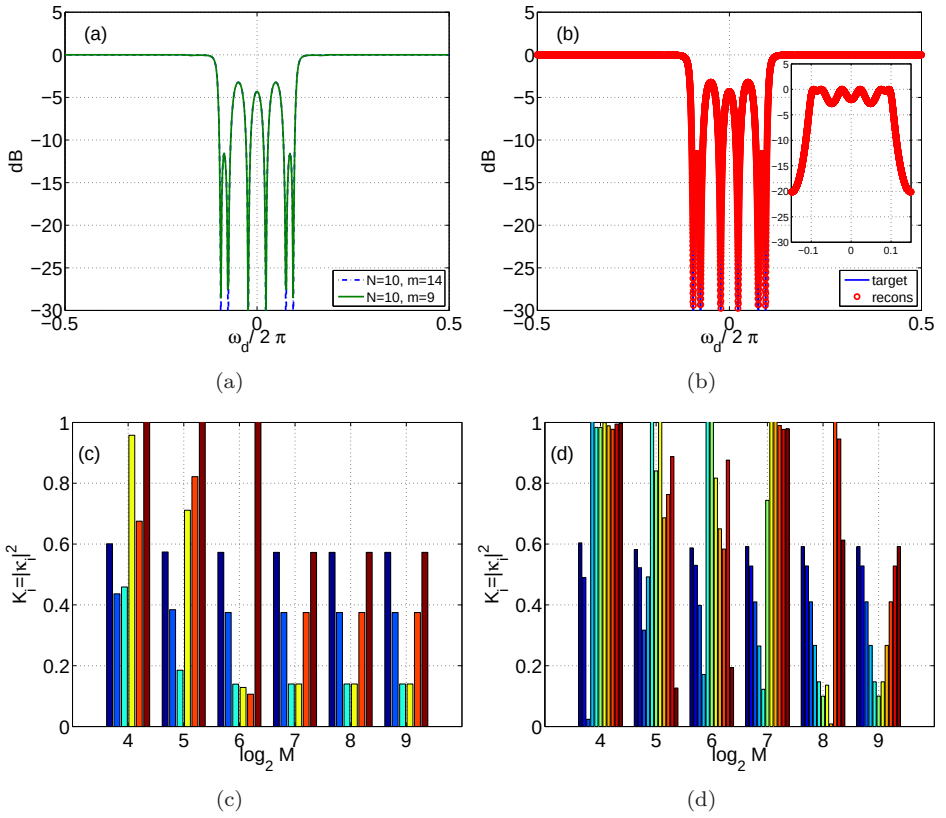

Figure 2.17: Hamming (H=0.2) apodized CROW with nominal $K = 0.1$ (a) target TMM calculated response for $m = 9$ and $m = 14$, (b) synthesized and target responses (inset transmission response) and reconstructed K_i values for (c) $N = 5$ and (d) $N = 10$ rings, all vs. IDFT number of points M used.

for the last coupler in the CROW, K_N. For 5 rings, convergence is achieved for $K = 0.2$ and $K = 0.3$ with $m \geq 10$, while $K = 0.1$ requires $m \geq 11$. The convergence worsens for 10 rings, where $m \geq 12$ and $m \geq 13$ are needed for $K = 0.2$ and $K = 0.3$ respectively, while $K = 0.1$ needs $m > 14$.

The reconstruction was also applied to a CROW device with apodized coefficients, where the t_i values are modified following a weight (window) function. Starting with a nominal coupling constant $K = 0.1$, a Hamming window with parameter $H = 0.2$ was used as described in section 2.3. Using equation 2.25 that describes the Hamming windowing, with $\gamma = 1$, the t_i coefficients are:

$$t_i = \sqrt{1-K}\,\frac{1 + H\cos\left(2\pi\frac{i-0.5(N-1)}{N}\right)}{1+H}, i = 0, ..., N$$

that correspond to $K_i = \{0.5728, 0.3750, 0.1397, 0.1397, 0.3750, 0.5728\}$ and $K_i = \{0.5919, 0.5280, 0.4101, 0.2668, 0.1470, 0.1000, 0.1470, 0.2668, 0.4101, 0.5280, 0.5919\}$ for 5 and 10 rings respectively. The TMM calculated target responses, sampled with the same points as in the uniform case of Fig. 2.15-(a), are shown in Fig. 2.17-(a). The smoothness produced by the apodization reveals that $m = 9$ is enough in this case. This results in less error on the impulse response approximation, since the differences between the samples of $h[n]$, using $m = 9$ and $m = 14$, are of the order of 10^{-14}. The convergence of all the coupling constants vs m is shown in Fig. 2.17-(c)(d) for 5 and 10 rings respectively. As outlined before, lower sampling is required for the apodized cases, since for theses cases convergence is achieved for $m \geq 7$ and $m \geq 9$, for 5 and 10 rings respectively. Finally, the responses calculated using the reconstructed coupling coefficients and TMM, are compared with the targeted responses in Figs. 2.15-(b) and 2.17-(b). An inset shows also the reconstructed transmission response. In both cases, uniform and apodized, the match between target and reconstructed responses is excellent.

2.5 Conclusions

The apodization or windowing of the coupling coefficients in the unit cells of serial and parallel coupled resonator waveguide devices as a means to reduce the level of secondary sidelobes in the bandpass characteristic of their transfer functions has been proposed and analysed. This technique which is regularly employed in the design of digital filters has also been applied as well in the past for the design of other photonic devices such as corrugated waveguide filters and fiber Bragg gratings. The apodization of both SCISSOR and CROW structures has been discussed for several windowing functions and sidelobe/ripples suppression in both structures demonstrated. In SCISSOR structures the cross coupling coefficient is apodized and windowing can be applied either to one bus or the two in the structure with the second option giving an increased performance in terms of secondary sidelobe suppression. The effectiveness of the different windowing functions must be compared using an independent metric and for this purpose the effective number of rings has been defined. Windows with a similar value of effective number of rings in the CROW structure yield a similar performance as far as sidelobe suppression is concerned.

Also the layer aggregation method for the synthesis of multilayer structures has been adapted to coupled resonator optical waveguides. A procedure to link the contribution of each cavity to the impulse response at every time has been derived. The procedure has been applied to the synthesis of CROWs, starting from targeted transfer functions. The procedure convergence has been examined in terms of the related parameters. An excellent match between the targeted and synthesized responses has been demonstrated for worst case convergence parameters.

Chapter 3

Longitudinal offset technique for apodization of CROWs

3.1 Introduction

In this chapter, the existing CROW apodization techniques are reviewed, and a novel method is proposed which allows for apodization in resolution limited fabrication processes. In coupled resonator structures, the adjustment of the coupling constants is typically done by changing the distance between the waveguides on the coupler [51], d in Fig. 3.1. This is technologically challenging, since the resolution step required in the 'x' direction (Fig. 3.1-a) can be well below the fabrication step resolution. Moreover, it is also technologically challenging to fabricate parallel waveguide couplers with small distance d, which is required to get strong coupling with short effective lengths, and therefore small footprint devices. In this chapter, a technique in which the coupling constant value K is changed by imposing an offset between the coupled waveguides (Fig. 3.1-b) is proposed. The offset shown in Fig. 3.1-b is imposed in the longitudinal direction 'y', while the distance between the waveguides, d, in the 'x' direction is kept fixed. The offset implies a reduction in the coupler effective length. The technique allows for both increasing and decreasing the value of K starting from a nominal value as will be shown in next sections.

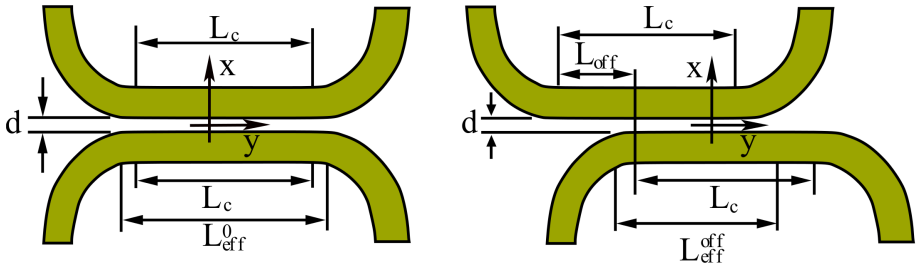

Figure 3.1: Directional coupler schematics for (a) gap and (b) offset control of the coupling. The offset is applied in the horizontal axis whilst the vertical distance is kept fixed.

3.2 Coupling constant control through the offset technique

The power exchange between waveguides in a directional coupler can be obtained from the power coupling constant [52]:

$$K = \kappa^2 = sin^2\left(\frac{\pi}{2}\frac{L_c}{L_b}\right) \tag{3.1}$$

where L_c is the effective coupler length and L_b the beat length of the coupler defined as the physical length where the power is completely transferred from one waveguide to another. The effective coupling length is longer than the straight coupling length for the most common integration technologies [53, 54] and this extra length is dependent on the separation between waveguides and the bend radius of the access waveguides. The effective coupling length is given by [55]:

$$L_c = L_s + 2 \cdot R \cdot arccos\left(1 - \frac{d_c - d}{2 \cdot R + w}\right) \tag{3.2}$$

where L_s is the straight coupling section, R the bend radius, d is the gap between resonators, w is the waveguide width and d_c is the distance between waveguides where light starts to couple in the bent section.

The combination of the coupling length and the distance between the waveguides provide different coupling constants and conditions the range of variation of the coupling constant when changing the offset or the gap. If the waveguides are too close, there are three direct undesired effects: the first one is related to the lithography and the proximity effect in the fabrication processes [56]. This effect reduces the targeted gap between the parallel waveguides and therefore changes the designed coupling constant. The second one is the mode conversion loss [55]. This loss comes from a non-adiabatical change of the even and odd supermodes of

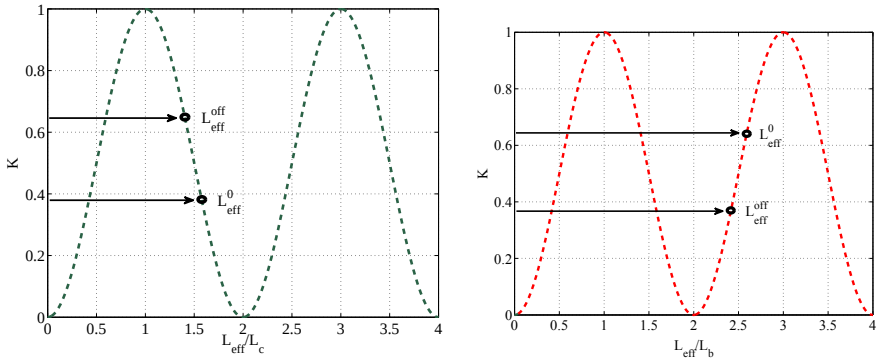

Figure 3.2: Illustration of the coupling constant change as the effective coupling length changes. In the first case (a) a reduction in the effective coupling length implies an increase in the coupling constant. In the second example (b) a reduction of the effective coupling length implies a decrease in the coupling value.

the device between the coupling section and the curves. When the air gap between the waveguides decreases, the mode shape difference between sections increases, and hence the mode conversion loss increases. Therefore the loss parameter of the coupler introduced in equation 2.5 is no longer $\gamma = 1$. The last one is the coupling-induced resonance frequency shifts (CIFS) [57]. Depending on the resonators geometry and their coupling scheme, CIFS can strongly distort the filter response. The CIFS effect in CROWs appears as an asymmetry in the spectra. In coupled resonator structures, the frequency shift is related to phase perturbations in the couplers. Depending on the technology, the CIFS effect can be minimized by employing the appropriate gaps in the coupler sections.

The proposed longitudinal offset technique allows for both increasing and decreasing the value of K, starting from a nominal value. This is shown in Fig. 3.2-a and Fig. 3.2-b respectively. In both figures, L^0_{eff} is the coupling effective length without offset, as in Fig. 3.1-a, while L^{off}_{eff} is the coupling effective length with offset, as in Fig. 3.1-b. In Fig. 3.2-a, L^0_{eff} is such a way that the starting K value is at a negative slope over coupler transfer function vs. effective length. Therefore, a reduction in the effective length, down to L^{off}_{eff}, will imply an increase in the K value. In Fig. 3.2-b, L^0_{eff} is such a way that the starting K value is at a positive slope over coupler transfer function vs. effective length. Therefore, a reduction in the effective length, down to L^{off}_{eff}, will imply a decrease in the K value. Each of these two mentioned techniques can be applied for the apodization of SCISSORs as well as for CROWs, as already shown in the previous chapter.

3.3 Coupling constant sensitivity analysis

The analysis shown is focused in the fabrication imperfections in Silicon-On-Insulator (SOI) technology using photolithographic processes, which is the technology used in the fabricated devices presented in this thesis, as motivated in Chapter 1. The resolution of the lithography equipments is in the order of five to ten nanometers but can be increased by post-processing the mask [58]. An important characteristic of the photolithographic processes is the exposure dose. In the fabrication process, this dose can be changed progressively from left to right of the wafer covering a deviation from the nominal thickness of the features in the mask [59]. In this section, a detailed analysis of the coupling in the directional couplers employed for the CROW structures will be shown. The coupling values have been numerically determined with the Beam Propagation Method (BPM) [60]. All the simulations have been carried out in 3 dimensions with a spatial resolution of 1x1x1 nm^3. The simulated layer stack recreates SOI wafers manufactured by SOITEC employed in the ePIXfab fabrication platform [24], 220 nm height Silicon core on top of 2 micrometers of SiO_2. The coupler lengths shown in the next sections have been chosen to show two different case studies: in the first case, the coupler length is 53.3 μm and the distance between the waveguides is d = 150 nm, hence the starting K value is at a negative slope over coupler transfer function, and therefore a longitudinal offset implies an increase in the coupling constant; in the second case a coupler length of 20 μm and waveguide separation of d = 100 nm are used, being the starting K value at a positive slope over coupler transfer function, and hence an offset implies a decrease in the coupling constant.

3.3.1 Gap apodized CROWs

For the CROW structures where the control of the coupling constant value is set by changing the lateral spacing between waveguides, the fabrication process resolution is a limitation [61]. Figs. 3.3-a and 3.3-b show the results of the 3D BPM simulations of a directional coupler with nominal length of 53.3 μm and 20 μm respectively. The distance between centres (d_0 in Figs. 3.3-a and 3.3-b) is kept constant for each sweep of the waveguide width (from 480 to 520 nm) in order to recreate the variation of the exposure dose in the fabrication process. The vertical axis represents the variation in the coupling constant as d_0 increases. In both cases, an increase of d_0 represents a decrease in the coupling constant. From Figs. 3.3-a and 3.3-b can be extracted that a small variation in d_0 (below the fabrication resolution) implies a significant change in the coupling constant. On the other hand, the horizontal axis reveals that for variations in the features sizes given by an over/down-exposure, the change in the coupling values is much less significant in the range studied. The latter effect can be explained as a compensation between the change of the distance between waveguides, d ($d = d_0 - w$), and the change in the confinement of the evanescent tails of the electric field related to a change in the waveguide width. Therefore, in this kind of couplers, to accurately set the desired coupling constants a resolution of nanometers in the fabrication process is

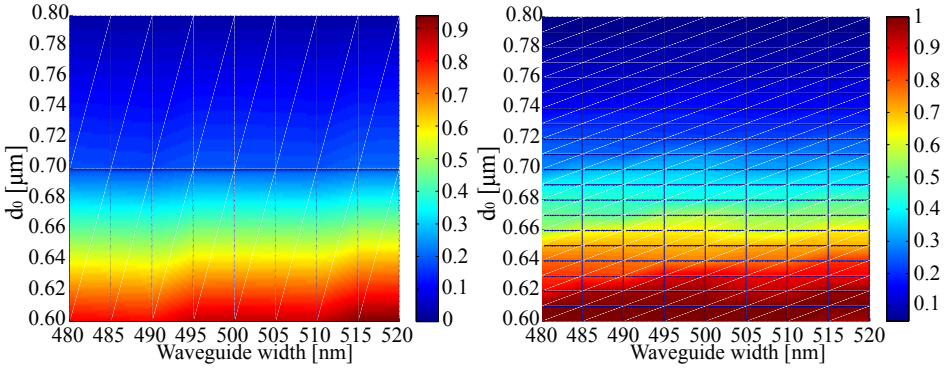

Figure 3.3: Coupling constant (K) vs waveguide width and distance between waveguides centers (d_0) for a nominal waveguide width $w = 500$ nm and a coupler length of 53.3 μm (a) or 20 μm (b).

needed, which is technologically challenging nowadays.

The resolution required for the fabrication of gap apodized CROWs can be achieved by means of electron beam lithography (EBL). The resolution achieved by direct-writing techniques can be well below 10 nm [62]. Even though EBL can allow accurate dimensional control [63], it is slow, complex, expensive and, due to the small writing area, it is unsuitable for mass production. The state-of-the-art photolithography equipments employed for photonics are using 193 nm Deep-Ultra-Violet (DUV) illumination [64]. The resolution that can be achieved with such a wavelength is in the order of 5 to 10 nm for isolated lines but undesired effects as Optical Proximity Effect [56] can affect the fabrication performance. When an isolated line comes in close proximity with another line (e.g., in an optical coupler), the line widths of both lines reduce as a function of the distance between them. There are techniques to correct these effects but the corrections required for gaps below 200 nm are much more important than for the gaps above 200 nm. In both cases, the final resolution will be given by a combination of the lithography technique plus the etching process employed. The etching process typically employed in SOI foundries is the inductively coupled plasma-reactive ion etching (ICP-RIE) [64].

3.3.2 Offset apodized CROWs

BPM analysis of the directional coupler with offsets is performed as well and the results are shown in Figs. 3.4-a and 3.4-b. The vertical axis here represents the variation of the coupling constant as the longitudinal offset increases/decreases. In this case, the variation of the coupling constant is controlled by changing the waveguides position in steps of micrometers or of hundreds of nanometers, a more relaxed condition than in the case of varying the gap. On the other hand, in the

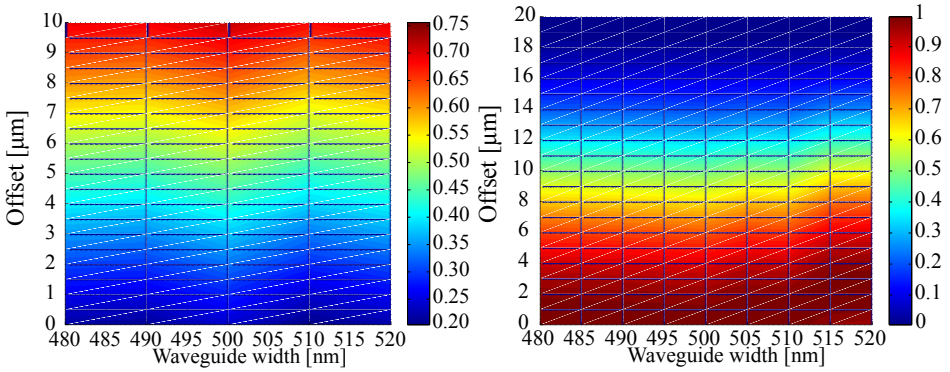

Figure 3.4: Coupling constant (K) vs waveguide width and longitudinal offset between the coupler waveguides for a nominal waveguide width $w = 500$ nm and a coupler length of 53.3 μm (a) or 20 μm (b).

horizontal axis the waveguides width change as the exposure doze varies is plotted. Figs. 3.4-a and 3.4-b show the calculated coupling constants for coupler lengths of 53.3 μm and 20 μm respectively. This two coupler lengths have been chosen to illustrate the two cases previously exposed in Fig. 3.2: the longitudinal offset can imply an increase of the coupling constant as in Fig. 3.4-a or a decrease as shown in Fig. 3.4-b.

Looking carefully at the scales of the vertical axis in Fig. 3.3, in the gap control of coupling, in order to obtain a change in the coupling constant of 0.5 a variation of tens of nanometers is required in the gap, whilst in the offset case (Fig. 3.4) for a similar variation, an offset of several microns is needed. Therefore the sensitivity of the offset technique is significantly higher compared with the gap case, and hence the control of the coupling becomes an easier task. The robustness of this technique will be demonstrated in the next section through several examples of CROWs for which spectral response has been calculated by the Transfer Matrix Method.

3.4 Transfer Matrix analysis

The frequency response of several CROWs has been calculated through the TMM formalism derived in Section 2.3.2 in order to compare the performance of both methods presented for the control of coupling constants in CROWs. Two CROWs with 3 and 5 racetrack resonators for each coupling scheme have been studied: uniform (non-apodized), gap apodized and offset apodized. The value of the coupling constants has been extracted from the BPM simulations presented in the previous section. Fig. 3.5 shows the ideal spectrum calculated with Matlab^{TM}for the 3 and 5 racetracks CROWs for the uniform and apodized cases. The spectra

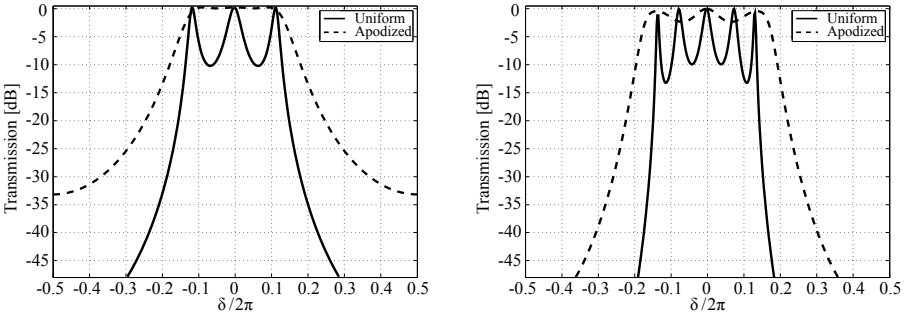

Figure 3.5: Transmission for 3 (a) and 5 (b) racetracks CROW. The uniform response (K=0.2 in all couplers) is depicted in continuous line and the apodized response (K values from the table) is depicted with the dashed line.

shown are limited to a single FSR expressed in normalized units of $\delta/2\pi$, being δ as introduced in equation 2.17:

$$\delta = \beta L_c = \frac{2\pi}{\lambda} \cdot c \cdot n_g \cdot L_c \tag{3.3}$$

with L_c the optical path length of a single cavity, c the speed of light in vacuum and n_g the group index of the waveguides defined as:

$$n_g = n_{eff} - \lambda \cdot \frac{\partial n_{eff}}{\partial \lambda} \tag{3.4}$$

where n_{eff} is the modal effective index.

Tables 3.1-(a) and 3.1-(b) summarize the coupling constants and the gaps or offsets required by design in order to obtain the ideal (lossless) apodized response calculated through the Transfer Matrix Method and depicted in Fig. 3.5. The offsets and gaps presented have been extracted also from the BPM simulations for both coupler lengths of 53.3 μm and 20 μm. All the spectra shown, are under the assumption that fabrication is done with infinite resolution, so the gaps and offsets required for the apodization can be accurately achieved. In practice this is limited by the fabrication process, leading to restrictions in the designs.

Table 3.1: 3 and 5 racetrack gap and offset apodized CROW

(a) 3 racetrack CROW

Hamming window apodization					
		[Lc=53.3 μm]	[Lc=20 μm]	[Lc=53.3 μm]	[Lc=20μm]
Coupler #	K_n	Gap [nm]	Gap [nm]	Offset [μm]	Offset [μm]
1	0.70616	124.90	147.90	9.858	7.122
2	0.30449	183.90	210.10	1.464	12.480
3	0.30449	183.90	210.10	1.464	12.480
4	0.70616	124.90	147.90	9.858	7.122

(b) 5 racetrack CROW

Hamming window apodization					
		[Lc=53.3 μm]	[Lc=20 μm]	[Lc=53.3 μm]	[Lc=20μm]
Coupler #	K_n	Gap [nm]	Gap [nm]	Offset [μm]	Offset [μm]
1	0.74065	119.80	141.00	10.650	6.612
2	0.52663	151.30	173.10	6.080	9.540
3	0.24870	192.10	216.70	0.193	13.290
4	0.24870	192.10	216.70	0.193	13.290
5	0.52663	151.30	173.10	6.080	9.540
6	0.74065	119.80	141.00	10.650	6.612

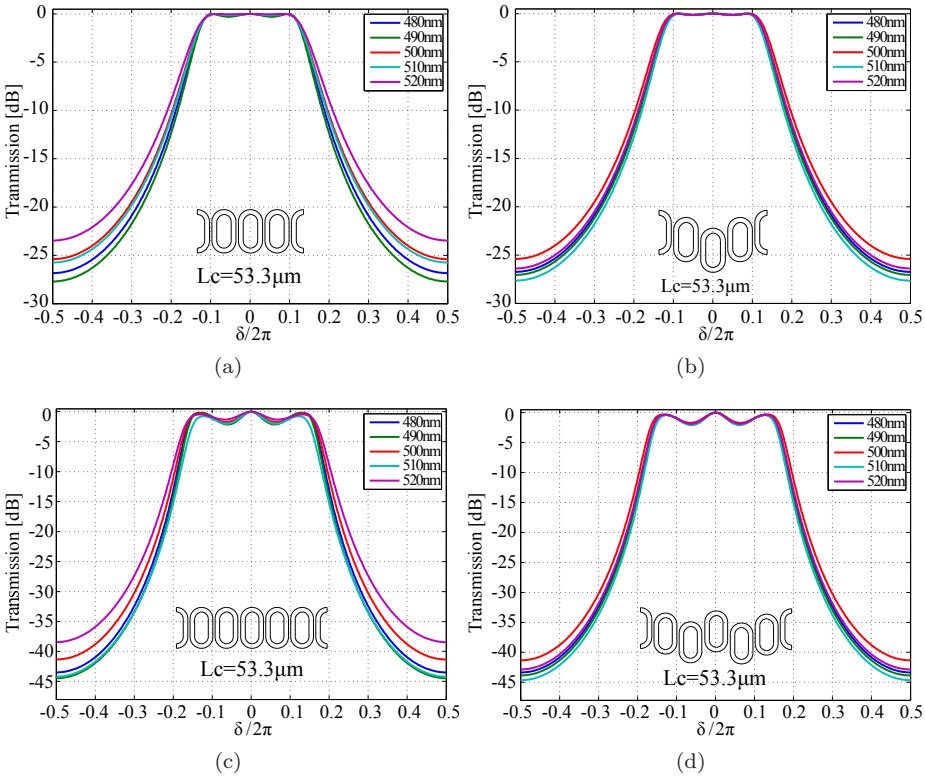

Figure 3.6: Transmission spectrum for 3 (a)(b) and 5 (c)(d) racetrack gap (a)(c) and offset (b)(d) apodized CROWs vs several waveguide widths simulating the variation in the exposure dose. The nominal width employed in the designs is w = 500 nm and the coupler length is 53.3 μm.

Fig. 3.6 shows the simulation of two gap apodized CROW and two offset apodized CROW of 3 and 5 cavities respectively with a straight section of 53.3 μm in the couplers. The coupling constants have been extracted from the BPM simulations shown in Figs. 3.3 and 3.4. The coloured lines represent a variation in the waveguide width whilst keeping constant the nominal distance between centres. These variations in the waveguides width represent the effect of the variation in the exposure doze that can be applied in the photolithographic process. This variation will be explained with more detail in the next chapter. Comparing the 3 racetrack resonators CROW for the gap (Fig. 3.6-a) and for the offset (Fig. 3.6-b) apodization cases, the ripples in the pass-band and the bandwidth of the filter present lower variations in the offset case than in the gap case. The results are similar for the 5 racetrack resonators case (Fig. 3.6-c vs Fig. 3.6-d). In the gap apodization case, the 3 and 5 racetrack resonators CROW response starts to deviate from the target showing an increased spectral width and a reduced out-of-band rejection.

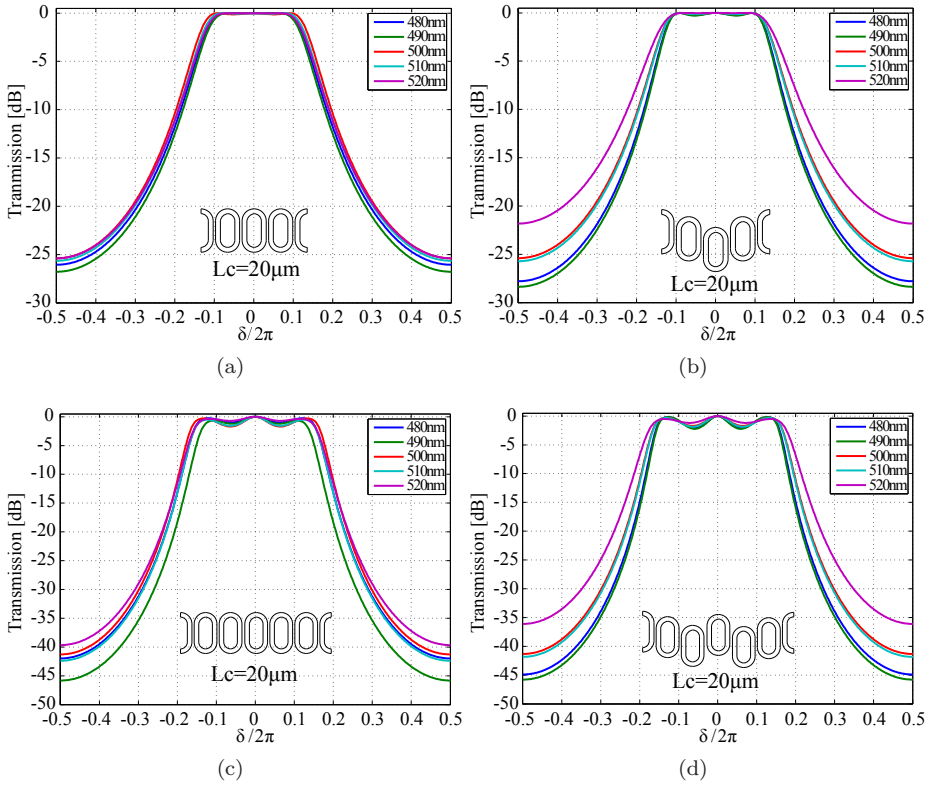

Figure 3.7: Transmission spectrum for 3 (a)(b) and 5 (c)(d) racetrack gap (a)(c) and offset(b)(d) apodized CROWs vs several waveguide widths simulating the variation in the exposure dose. The nominal width employed in the designs is w = 500 nm and the coupler length is 20 μm.

Fig. 3.7 shows the same comparison as in the previous example of Fig. 3.6 but in this case the straight coupling section has been reduced to 20 microns. In this example, the comparison of Fig. 3.7-a vs Fig. 3.7-b and Fig. 3.7-c vs Fig. 3.7-d appears to be better for the gap case than for the offset case. In any case the variations presented in the spectra are small enough to fit the design requirements. Despite the results can be interpreted as if both methods present similar robustness against fabrication imperfections this is not true. In most cases, the required gap changes are below the fabrication resolution or close to its limit. On the other hand, employing the longitudinal offset apodization technique, the offsets required for setting the coupling constants are well above the resolution limit of the fabrication processes. This will lead to distorted or out of target responses in the fabricated devices for the gap case and not for the offset case. In the next chapter, the experimental demonstration of this longitudinal offset technique for the apodization of CROW devices is shown.

3.5 Conclusions

A novel technique for controlling the coupling between racetracks in SCISSOR or CROW structures has been presented. This technique allows a better control of the coupling typically limited by the fabrication resolution. The sensitivity is increased critically by using the longitudinal offset technique despite the increase in the footprint of the final devices. It has been demonstrated through simulation, how the apodization of Coupled Resonator Optical Waveguides through the longitudinal offset technique is as effective as with conventional techniques, reducing the accuracy required for fabrication. As expected, the ripples within the passband transmission and group delay are reduced through apodization.

The main benefits of the longitudinal offset apodization technique are:

- Allows for an accurate setting of the coupling constant in the unit cells of CROW and SCISSOR devices
- Reduces the tight fabrication requirements for coupled resonator devices
- Allows for the use of mass production techniques in the fabrication of coupled resonator devices
- Can be employed in CROWs, SCISSORs or any device containing directional couplers

Via the Universitat Politècnica de València (UPV) Technology Transfer Office, the longitudinal offset technique has been patented at a national level (Patent Number P200901145 - 4/23/09). The patented technology has been licensed to the UPV Spin-Off company VLC Photonics S.L. for its exploitation.

Chapter 4

Design and fabrication of Coupled Resonators in Silicon On Insulator

4.1 Introduction

In this chapter the design, fabrication and characterization of CROWs in Silicon On Insulator (SOI) technology will be studied in detail. The design of CROW devices through its conforming sub-structures analysis and characterization will be reported, from simple waveguides to the basic unit cell of CROWS: the ring resonator. The experimental results obtained will be compared to the theoretical predictions calculated with the models developed in the previous chapters. The CROW devices described in this chapter implement the longitudinal offset technique for setting the coupling constants that has been introduced and developed in the previous chapter.

4.2 Fabrication details

Silicon photonics is one of the most promising technologies for the future photonic integrated circuits [23]. The Silicon Photonics technology platform offers passive light manipulation at a very small footprint, allowed by the relative high contrast index of silicon. Such small chip size, its cheaper base material and its CMOS fabrication compatibility also results in a lower chip price. However, no light amplification is possible at the time other than hybrid integration [65], meaning that integration with other technologies will be required for some active functionalities. In the following subsections, the fabrication technology will be introduced as well as the access scheme employed for the prototyping in the selected technology.

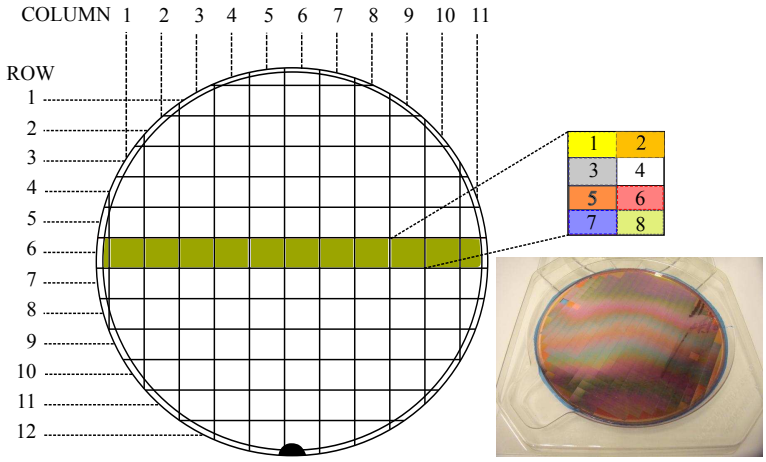

Figure 4.1: Schematic of the wafer partitioning and exposure. The wafer is divided in rows and columns to conform the dies containing the users designs. The notch in the bottom of the wafer indicates its crystallographic orientation and it is used as a reference for positioning the bottom side of the wafer. The inset on the top right part shows how a single die is divided into sub-dies that can be filled with designs from different users. The picture from the bottom right inset shows one of the fabricated wafers.

Multi-Project-Wafer runs

Several sets of CROWs with and without apodization have been fabricated in Silicon On Insulator technology during the realization of this thesis. The fabrication runs have been carried out in several Multi Project Wafer (MPW) runs within the ePIXfab platform [24]. In these MPW runs, the users can share fabrication costs by means of sharing process steps and wafer space. The wafer is divided in dies limited in size by the step and repeat lithography equipment. The maximum die size is approximately 25 x 25 mm^2 because of commonly available CMOS machinery employed for fabrication, in the case of ePIXfab, the equipment is the ASML PAS5500/1100 step-and-scan system. Every die is sub-divided in smaller sub-dies that are filled with the designs of individual users and every user receives a fixed number of dies. The dies can be diced individually for each user to receive its own design or one can choose to receive a full die. The intellectual property is protected by employing a laser process to remove other customers' integrated circuit designs from the MPW while leaving specified designs intact. Fig. 4.1 shows the partitioning of the wafer in dies and the inset at the right shows how each die is divided into smaller sub-dies allocatable to different users. The wafer is hence divided in columns/rows. Although the designs within a die may well be different (designs come from distinct users) the fabrication process is the same. Nonetheless, the exposure doze can be varied per column. The exposure dose is the intensity of DUV light per area unit that is applied to the photoresist on top of

the wafer. The variation in the exposure dose introduces variations in the features sizes. A low exposure dose makes the waveguides wider and the gaps narrower and a high exposure dose makes the waveguides narrower and the gaps wider. Typically this exposure dose is varied from left to right incrementally. The left and right parts can be distinguished with the help of the notch in the wafer indicating the bottom part as shown in Fig. 4.1. During the fabrication process, at some specific steps, measurements of critical dimensions in the designs are made with scanning electron microscopy. For instance, after every etching level, the width of the waveguides is controlled. The users can define a set of critical dimensions in their designs that will be monitored and reported after the fabrication. A critical dimension is a measurement of a feature in the design (i.e. a waveguide width). These values are used as reference for checking the fabrication process.

Fabrication Technology

The devices reported in this thesis were fabricated in the CMOS line of imec (the Inter University Microelectronics Center), Leuven, Belgium. The access to the fabrication runs was possible through the ePIXfab [24] service. ePIXfab organizes MPW shuttles in silicon photonics technologies. This allows researchers/engineers to prototype silicon photonic ICs at affordable cost. For the users, this fabless scheme allows them to focus on device and application ideas, design and characterization. The technologies that ePIXfab offers are high-end wafer scale CMOS-type fabrication technologies. Setting up and maintaining a fab with such a complex technology is only possible for a few companies and research institutes in the world. All ePIXfab fabrication is done on production-type tools. The fabrication is carried out on 200 mm SOI wafers, manufactured by SOITEC, processed with 193 nm deep Ultra Violet (DUV) lithography and dry etching. Details of the fabrication processes employed can be found in [59, 64].

4.3 Building blocks design

In these fabrication runs several building blocks (BB) were designed and fabricated, as waveguides, directional couplers and racetrack resonators amongst others, to conform the CROW devices under study in this work. For the design of these building blocks, the most relevant parameters were scanned through multi-parametric (computer-aided) analysis. For instance the geometry of the waveguides when computing the propagating modes, the wavelength dependency of the refractive indices of the materials and also the wavelength dependency of the coupling constant in the parallel waveguides couplers.

The waveguides

The fundamental BB for all the structures is the waveguide. Optical waveguides in SOI technology should provide low propagation losses and small bending ra-

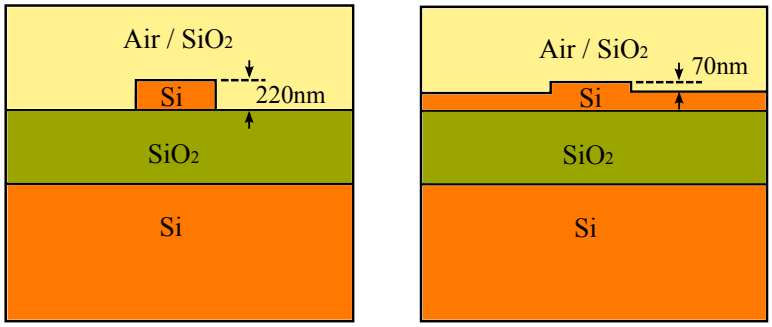

Figure 4.2: Deeply (a) and Shallowly (b) etched waveguide cross-sections in a typical SOI layerstack. The top cladding can be different depending on the application. The typical etching levels for the two configurations shown are 220 nm and 70 nm.

dius whilst ensuring single mode propagation and polarization independence. The transverse electric (TE) and transverse magnetic (TM) modes have very different effective index and propagation loss. Polarization independency is very hard to achieve, although it is possible to change this by altering the core form factor [66]. The waveguides height is defined in the wafer fabrication process. The guiding Silicon layer thickness for photonic applications is in the range between 220 nm to 5 microns. Depending on this thickness, and in combination with the width and the Buried Oxide (BOX) substrate thickness, the waveguide will support a different amount of propagating modes. The standard Silicon height adopted by most of the SOI foundries running MPW runs is 220 nm on top of 2 microns BOX. This thickness provides tight confinement and moderate propagation losses, and together with the appropriate etching levels also allows for ultra small bending radius. This combination of properties makes possible the creation of miniaturized photonic circuits. From the designer point of view, there are only two free design parameters regarding the waveguides: the width and the etching. The etching levels are also predefined by the foundry and there are typically two etching levels to conform the deep (DE) and shallowly (SH) etched waveguides. In the case of imec, the etching levels are 220 nm and 70 nm for the DE and the SH waveguides respectively. Fig. 4.2 shows the cross-section of the deep and shallowly etched waveguides in SOI. The difference between SH and DE waveguides is the optical confinement. Confinement has impact in both the propagation loss for straight waveguides, and the minimum bend radius for bent waveguides. Propagation loss is mainly due to surface roughness, which is felt by the mode propagating within the waveguide. DE waveguides sidewalls are hence more prone to roughness due to etching all down the film. Therefore, the propagation loss for DE waveguides is larger than for SH waveguides. Typical values for DE waveguides are in the range from 2 to 3 dB/cm [67] and for the SH from 0.5 to 1.5 dB/cm [68]. One

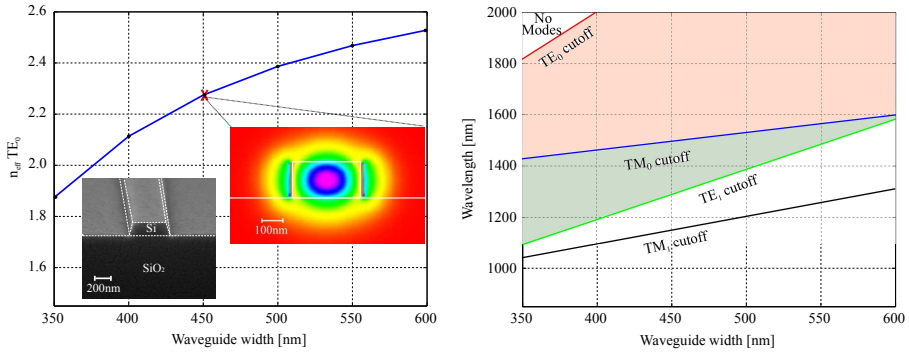

Figure 4.3: (a) TE_0 effective modal index (n_{eff}) as a function of the waveguide width at a wavelength of $\lambda = 1.55\mu m$ for a deep-etch waveguide with air cladding. The right inset shows the TE_0 mode profile for a width of 450 nm. The left inset shows a Scanning Electron Microscope image of the cross-section of a 450 nm width SOI waveguide. (b) Cut-off wavelength of a DE waveguide for the two lowest order TE and TM modes as a function of the waveguide width. The pink area shows single-mode support for TE and the blue area for TM polarization.

of the techniques employed for loss reduction in air or Silica cladding waveguides is a thermal oxidization step after the etching. With this technique, the surface roughness is reduced at a cost of loosing some nanometers of the Silicon guiding layer that are transformed in Silicon Dioxide. The minimum bend radius is dependent on the confinement. In the SH waveguides the modes are less confined in the core than in the DE waveguides due to the reduced index contrast, this allows to employ smaller bend radius in the DE waveguides. In the case of SOI, bend radius down to 1.5 microns have been demonstrated [69]. The cladding in both configurations can be either Silicon Oxide or just air. The main difference arises from the index contrast and therefore is reflected in the confinement. Waveguides that have a Silicon Oxide cladding present a slightly reduced index contrast than unclad waveguides but are less exposed to external agents like temperature, humidity, etc. For biosensing applications, waveguides without cladding (i.e. air) are most suitable [70].

In the devices presented in this work, the waveguides have no cladding (air) and are deeply etched. In order to choose the appropriate width, a commercial mode solver based on Finite Differences (FieldDesigner^{TM}) from Phoenix Software [28] has been employed. The effective index of the first transverse-electric (TE) mode for a wavelength of 1.55 μm has been calculated for waveguide widths varying from 350 to 600 nm as shown in Fig. 4.3-(a). The insets of the figure show the TE mode profile for a waveguide width of 450 nm and a SEM image of a fabricated waveguide. For the devices presented in this thesis, widths of 500 nm and 450 nm

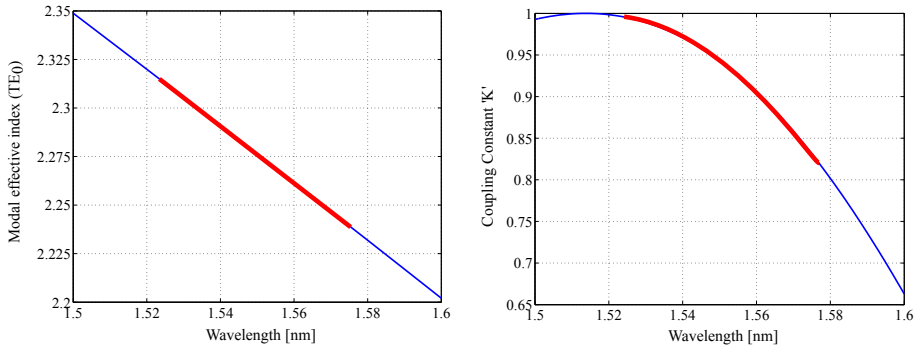

(a) (b)

Figure 4.4: Modal effective index (a) numerically calculated for a waveguide geometry of 220 x 450 nm^2 and power coupling constant (b) numerically calculated for a directional coupler with the same waveguide geometry and a separation of 200 nm between waveguides. Both graphs have been calculated for SOI technology employing PhoeniX software .

have been employed in two different fabrication runs. As shown in Fig. 4.3-(b), these widths allow for TE monomode propagation at the working wavelength of 1550 nm. The cut-off wavelengths shown in Fig. 4.3-(b) have been calculated with the MIT software MPB [71] following the methodology described in [72]. Fig. 4.4-a shows the calculated effective index of the first TE mode propagating in the waveguide and its wavelength dependency for a DE waveguide of 220 x 450 nm.

The couplers

The second BB under test has been the directional coupler (DC). The DC is well known [35] and it consists of two waveguides running in parallel. When the lateral distance between them is such that the tails of the individual modes overlap, the waveguides are coupled. This is also known as evanescent field coupling. The power is exchanged periodically between the waveguides. At a distance called the beat length the power is transferred completely from one waveguide to another as explained in section 3.2. Figure 4.5-a shows the SEM images of two of the fabricated and measured devices. The first one is a symmetric directional coupler and the second one is a directional coupler with a longitudinal offset. The couplers physical parameters are: a cross-section of 220 x 450 nm, a straight coupling section of 15μm, 5μm bend radius and a gap between waveguides of 200 nm. The coupler shown in the bottom of Fig.4.5-a also includes a longitudinal offset of 3μm.

Figure 4.5-b shows the measured power coupling constant (K) for the two directional couplers depicted in Fig. 4.5-a. The measurements have been carried out in the following way: first a reference straight waveguide is measured for normalization purposes. Later the spectra from the two outputs is captured when

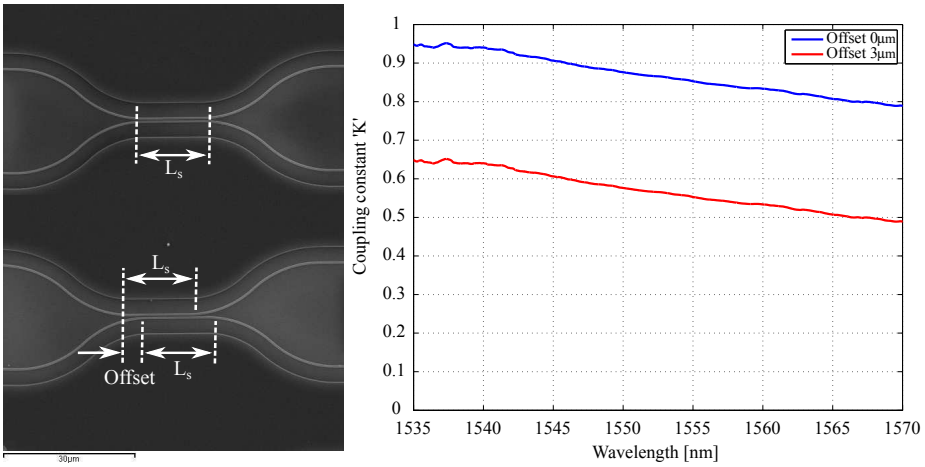

(a) (b)

Figure 4.5: (a) SEM images of fabricated symmetric directional couplers and with a longitudinal offset. (b) Measured coupling constant for both couplers. The blue line refers to the symmetric directional coupler and the red line represents the measured data for the directional coupler with a longitudinal offset of 3 μm

injecting light from one of the input ports. The power coupling constant K is then calculated as the power measured in the cross port divided by the total power (in this case calculated as the sum of the power detected at the two output ports). The measurements obtained from both output ports are normalized with the reference measurement to eliminate the effect of the grating couplers. The graph shows the wavelength dependency of the coupling constant for the chosen coupler geometry following equation 3.1. The blue line corresponds to the uniform coupler and the red line corresponds to the coupler with a longitudinal offset. As presented in section 3.2, for a given coupler length, the introduction of a longitudinal offset can either increase or decrease the coupling constant in a directional coupler. In this case by applying an offset of 3 μm and therefore reducing the effective coupling length, the coupling constant is decreased as can be derived from the measurements shown in Fig. 4.5-b.

Racetrack resonators

The basic unit cell of the CROW structures designed in this work are the racetrack resonators. CROW structures are typically conformed either by ring resonators or racetrack resonators. In this work, racetrack resonators have been employed given that these structures allow to better implement the longitudinal offset technique for setting the coupling constants in the CROW device. Rings can also be used but control would be uncertain. Fig. 4.6-a shows a SEM picture of a dual-bus

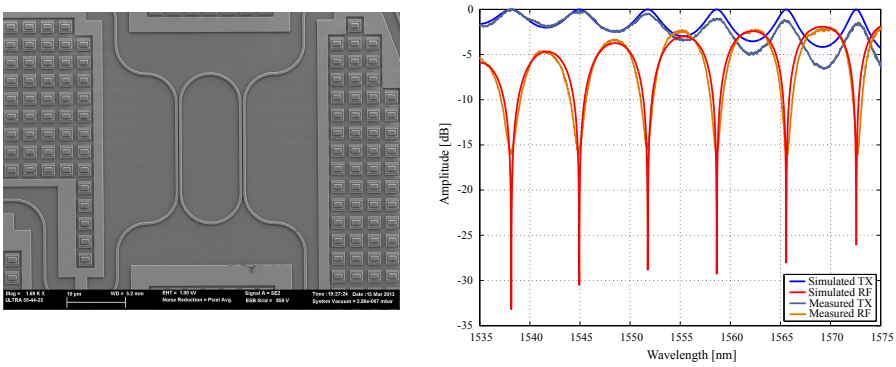

(a) (b)

Figure 4.6: (a) SEM image of a dual-bus coupled single racetrack resonator and (b) simulated and measured spectra.

coupled single racetrack resonator. The racetrack has a radius of $5\mu m$ and a straight coupling section of 15 μm. The gap between the racetrack and the access waveguides is 200 nm.

Figure 4.6-b shows that the measured and simulated responses of the single cavity resonator are in good agreement. In order to model the response of the single racetrack resonator the TMM formalism developed in section 2.2 has been employed. From equation 2.9 the transmission and reflection responses of a single resonant cavity can be extracted. The effective indices and the coupling constants have been extracted from the data calculated in section 4.3 and introduced in the model for an accurate fitting. The transmission spectrum is pass-band and the reflection spectrum is band-reject as described in [3]. The depth of the notches in the reflection and out-of-band in transmission is given by a combination of the coupling and losses in the resonator as explained in [73]. The spectra in transmission and in reflection grows towards right due to the wavelength dependency of the coupling constant and refractive indices.

4.4 Experimental results

4.4.1 First fabrication run

This run will be referred as Run #1 along the text. For the Run #1, the silicon photonic wire waveguides, on top of a 2 μm thick BOX layer, is 500 nm wide by 220 nm thick in order to ensure Transversal Electric (TE) monomode propagation as can be extracted from Fig. 4.3-(a). The left inset shows the cross-section of one of the fabricated waveguides. Notice the slightly slanted walls due to the etching process employed during the fabrication.

In Run #1, the wavelength dependency of the material refractive indices and

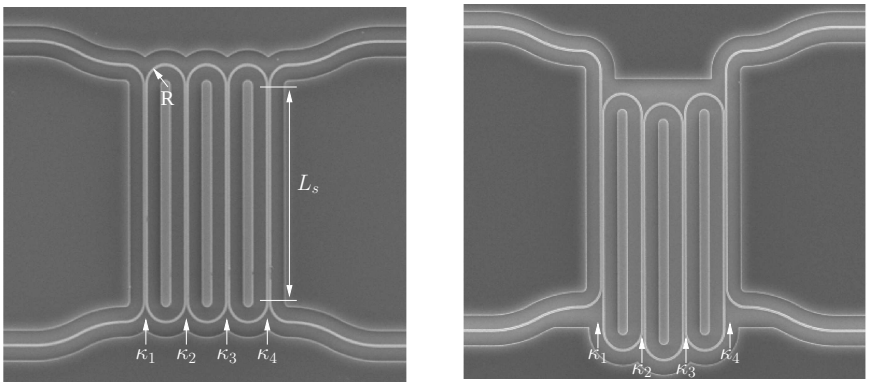

(a) (b)

Figure 4.7: SEM images of a three racetrack uniform CROW (a) and three racetrack apodized CROW (b)

coupling constants was not taken into account. When neglecting the wavelength dependency of n and K the results are only valid in a small range of wavelengths. In this case the fitting of the measurements and simulations are accurate in a single FSR. In SOI waveguides, the group index n_g exceeds the refractive index of bulk silicon, clearly indicating that in case of photonic wires with strong optical confinement the propagation constant of the waveguide is dominated by the waveguides' geometry and not by material properties [72]. Regarding the coupling constant, the wavelength dependency affects to the individual resonances within each resonator in the CROW device. That is directly translated to a different response for each FSR. Figures 4.7-(a) and 4.7-(b) show Scanning Electron Microscope (SEM) images of the uniform and apodized CROW devices, respectively. The racetracks have a bend radius R = 5 μm and a straight section $L_s = 53.3$ μm in both devices. The measured linear propagation loss in such photonic wires is 3 ± 1 dB/cm. The group index around 1.55 μm wavelength is $n_g \simeq 4.25$. It has been derived from the measured Free Spectral Range (FSR) of the CROW devices. The gaps between cavities in the uniform and apodized CROWs were set to 150 nm. The spectral measurements presented in this section belong to the selected devices whose gaps were closest to the design gap. The devices were selected by performing SEM and Atomic Forces Microscope (AFM) measurements on several dies. In the fabrication process at imec, the guaranteed minimum gap was 120 nm and that is why 150 nm was chosen, to be on the safe side. For the uniform CROW, all the racetracks have the same coupling length and therefore the same coupling constant that is $K_1 = K_2 = K_3 = K_4 = 0.48$. The couplings in the apodized CROW have been set symmetrically: the longitudinal offset applied to the first and last racetrack is the same and the resulting coupling constants have a value of $K_1 = K_4 = 0.86$ and a different offset has been applied to the central racetrack, and as a result $K_2 = K_3 = 0.54$ as proposed in the previous chapter. Translating

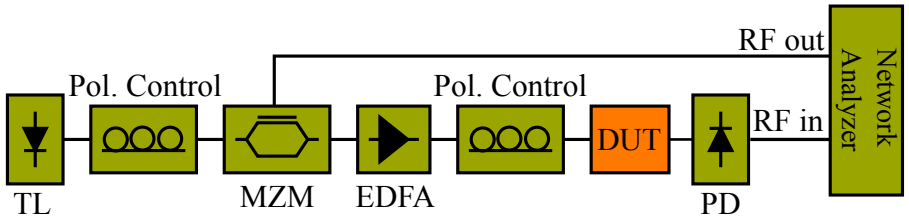

Figure 4.8: Group delay characterization setup. Continuous lines represent optical signals and dashed lines electrical signals.

the coupling values to physical parameters it is found that for a straight coupling section of 53.3 μm, the actual coupling length is even longer and is given by Eq. (3.2). Apodization requires $K_1 = K_4 = 0.86$ and $K_2 = K_3 = 0.54$ as outlined below. This translates to a longitudinal offset of 10.56 μm and 2.42 μm respectively. Conversely the same apodization through a change of the coupler gap would require gaps of 153 nm and 170 nm, for fixed L_c. Comparing the required changes with both techniques it is clear that the longitudinal offset technique requires less precision and it is less sensitive when setting the coupling constants.

Power and Group Delay Measurements

The power and group delay transfer function were measured for the devices in Fig.4.7 employing the setup shown in Fig.4.8 and the results are presented in Fig.4.9. A tunable laser (ANDO AQ4321D, $\lambda = 1520 - 1620$ nm) was externally modulated with a 100 MHz signal [74]. At the output of the modulator, the light was amplified with an Erbium Doped Fiber Amplifier (EDFA). The polarization was controlled both at the input of the modulator and at the input of the chip. The signal must be re-polarized because grating couplers [75] are used for in/out coupling light into the device under test (DUT) and have been optimized for TE propagation. At the output of the chip, the signal was then photodetected. Central in this setup is the Microwave Networks Analyzer (Agilent, E8364A), which drives the modulator and receives the signals from the photodetector. It measures the amplitude and phase of the signal. The group delay is expressed in terms of the phase as follows [74]:

$$\tau_g(\lambda) = \frac{\phi_d(\lambda) + \phi_0}{\omega_m} \tag{4.1}$$

where $\phi_d(\lambda)$ is the measured phase of the signal, ϕ_0 is a constant phase term introduced by the setup in the absence of resonant structures and ω_m is the modulation angular frequency. The term ϕ_0 has been obtained by averaging several measures done on straight waveguides employing the same setup.

Fig.4.9 shows the measured amplitude and group delay (red lines) of the devices compared with the theoretical responses (blue lines) calculated with the TMM described in chapter 2, where losses and the coupler length were taken into account.

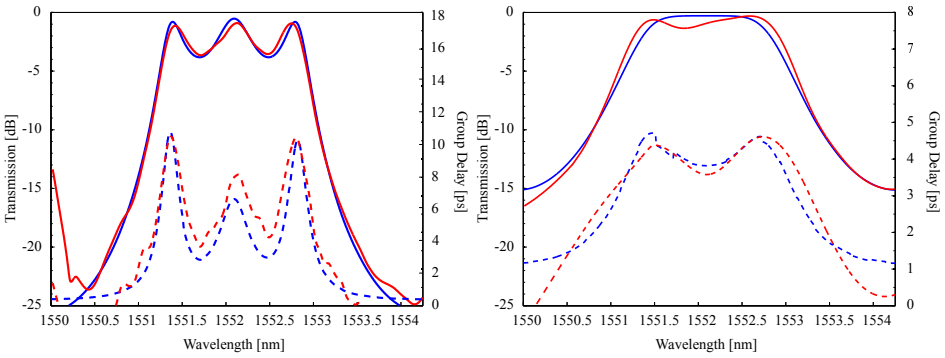

Figure 4.9: Power transmission and group delay responses of a 3 racetrack resonator uniform CROW (a) and offset apodized (b). Blue lines (continuous for the amplitude and dashed for the group delay) represent the theoretical responses and red lines represent the measured responses.

In the case of the uniform CROW, Fig. 4.9-(a), the measured transmission passband exhibit big ripples that have natural correspondence in the group delay. These ripples are due to the fact that all the coupling constants are equal [76]. This was fully described by the theory in Chapter 2 and shown in Fig. 2.13 in there. A mean delay of 5 ps has been measured with ripples of ± 3 ps in a 3 dB bandwidth of 1.6 nm, as predicted by the transfer matrix calculations. For the offset apodized CROW, Fig.4.9-(b), a flat response in transmission, due to the apodization of the structure, has been measured and a delay in the passband of about 4 ps with reduced ripples of ± 0.5 ps in a 3 dB bandwidth of 1.4 nm.

4.4.2 Second fabrication run

In this fabrication run our designs contain, amongst other test structures, a set of CROWS with 3, 5, 7, 11, 21 and 31 racetrack resonators with and without apodization. This run will be referred as Run #2. Fig. 4.10 shows the SEM images of CROWs with 11 racetrack resonators. The images correspond to uniform and longitudinal offset apodized CROW devices. The standard waveguide cross-section chosen was 450 x 220 nm^2 and the minimum bend radius 5 μm. In the case of the racetracks, the gap between cavities has been set to 200 nm and the radius fixed to 5 μm. The straight coupling section of the resonators chosen was 15 μm. The election of the straight coupling length was made to demonstrate the second case change in the coupling constant presented in Section 3.2 and illustrated in Fig. 3.2-(b). In this case a decrease in the effective coupling length will result in a reduction of the coupling constant.

In Run #2, dose sweep was applied during the lithography step, in order to vary the feature size from the left side to the right side of the wafer (Fig. 4.1)

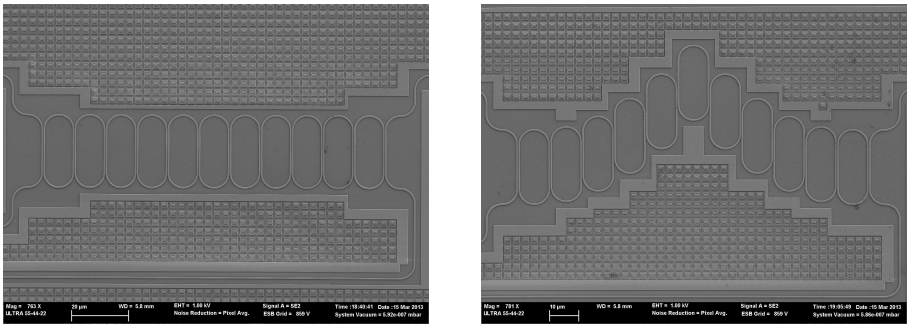

(a) (b)

Figure 4.10: SEM images of a 11 racetrack resonator uniform CROW (a) and apodized with the longitudinal offset technique (b).

as described in Section 4.2. As mentioned previously, during the fabrication, a dose sweep has been applied in the lithography step and therefore the features will change from one side to the other of the wafer. Fig. 4.11 shows the effect of this variation in the dose. Figs. 4.11-a and 4.11-b show Field-Emission Scanning Electron Microscope (FESEM) images from the couplers of a test single racetrack resonator from a die within the first column. Figs. 4.11-c and 4.11-d show FESEM images from the couplers of a test single racetrack resonator from a die within the last column.

In the Run #1 was demonstrated how through the apodization, in the case of CROWs of the direct coupling coefficients, the ripples in the passband of the CROW devices are reduced, but this happens at the cost of an increase in the filter bandwidth as explained in Chapter 2.

In Run #2, the wavelength dependency of the n_{eff} and K haven't been neglected. At long wavelengths the group index experiences a linear increase and the coupling constant starts to decrease as was shown in section 4.3. When this wavelength dependency is considered, the resonances of the CROW devices start to overlap due to an increase in the filter passband and a change in the FSR. This increase in the passband is due to the change in the coupling constant. A slight change in the filter periodicity can be observed as well and is mainly due to the group index change. When the response of the filter starts to overlap, the out of band rejection starts to decrease. The cross coupling coefficients of the CROW devices have been apodized in this run to increase the out-of-band rejection and have more selective filters at a cost of course of reducing the filter bandwidth. An apodization window that allows to increase the roll-off of the filters while keeping the passband ripples at an acceptable level has been applied. Figure 4.12 shows the simulated and measured group index of the fabricated CROWs. The group index has been derived from the FSR of the CROWs as in the previous sections but in this case for three different wavelengths. The measurements show small deviations from the simulation. These deviations arise from the fact that the measured FSR

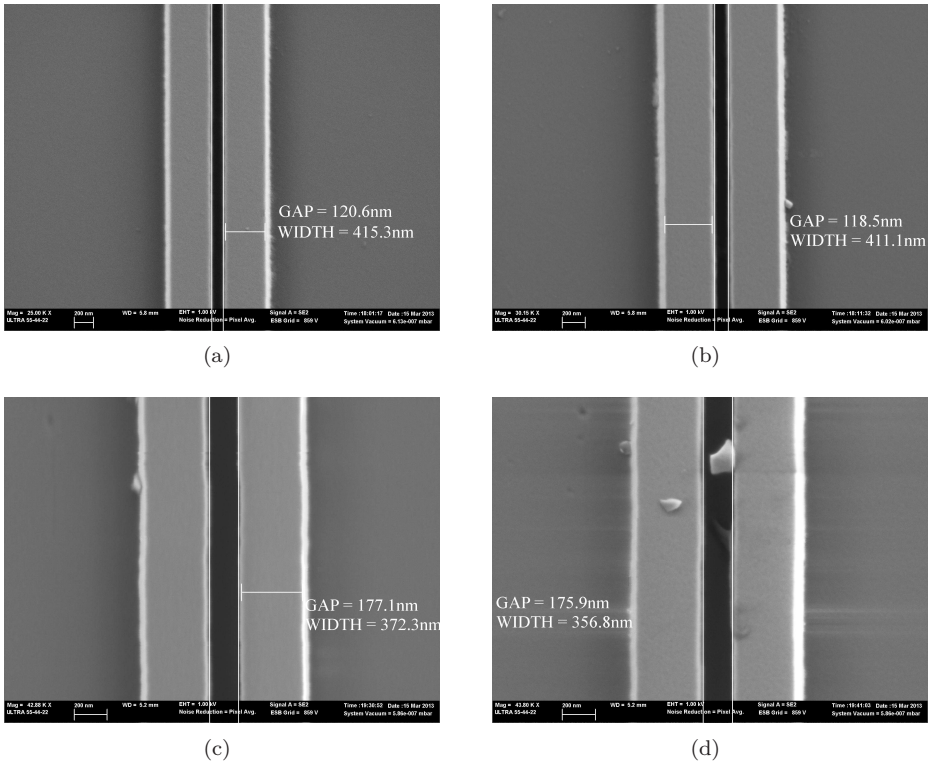

Figure 4.11: FESEM images of two directional couplers from a die within the middle column of the wafer (a-b) and a die coming from the last column of the wafer (c-d). Both dies have been overexposed and therefore the waveguide widths are out of target (450 nm). The variation on the exposure doze is reflected in the change of waveguide and gap widths.

employed to derive the group index may contain errors as well, given the difficulty of accurately determine the FSR because of the non-uniform shape of the spectral responses. As expected, the group index n_g is higher than in the fabrication Run #1 due to the reduced core size of the waveguides.

Figures 4.13 to 4.18 show the normalized TE simulated and measured spectra for the uniform and apodized CROW structures with 3, 5, 7, 11, 21 and 31 racetracks. Sub-figures (a) and (c) show the transmission responses whilst in (c) and (d) the reflection responses are shown. The fitting between simulation and measurement is excellent for all the CROW devices, either uniform or apodized.

There exist two important differences between the theoretical and experimental results. First is the asymmetry of the spectrum response produced by the CIFS. The CIFS effect, introduced in Chapter 3, was accounted for when designing the CROW devices by introducing a gap between cavities big enough to minimize this undesired effect. Even though, for some of the devices this effect is still present as

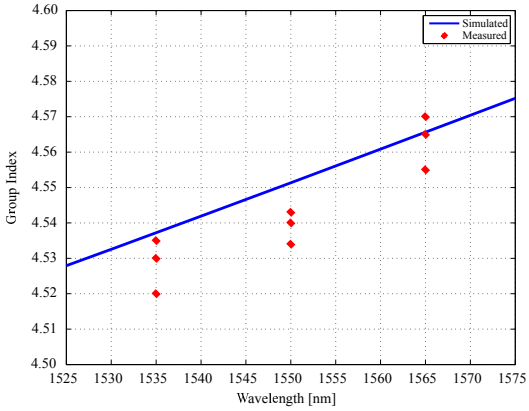

Figure 4.12: Simulated and measured group index for the fabricated CROW devices. The blue line depicts the calculated group index from the simulation data presented in Section 4.3. The red dots indicate the measured group indices from three different fabricated devices.

can be shown in Figs. 4.13-(c) and 4.13-(d) for instance. The measured transmission and reflection for the apodized CROW present an important asymmetry. In the higher order CROW devices, this effect is almost negligible.

Regarding the non-apodized CROWs, there are two important features in theoretical spectrum responses with increasing number of resonators which are confirmed by experimental results. As the number of the resonators increases, first, out-of-band rejection increases. This effect can be observed in Figs. 4.13 to 4.18 in the transmission spectrum of the uniform CROWs (a). Given the nature of the coupling in the designed structures, the effect is more pronounced for shorter wavelengths. Second, rising and falling edges of the spectra become steeper. The difference is clear between Fig. 4.13-(a) and Fig. 4.16-(a). There is a third feature that is not reflected in the graphs because of the amplitude normalization, the peak resonance intensity at the transmission port decreases due to enhanced loss.

In the case of the apodized CROWs, given the inverse apodization employed in this fabrication run, the first two effects mentioned before are more remarkable. The out-of-band rejection increases dramatically, in some cases more than 40 dB. This is the case for the 11 racetrack CROW. Comparing the out-of-band rejection from the uniform case in Fig. 4.16-(a) and the apodized in Fig. 4.16-(c), an increase of more than 40 dB for longer wavelengths can be observed. In fact the increase might be greater, but the measurements are limited by the dynamic range of the instrumentation employed. Also the rise and falling edges become stepper but in the 31 racetrack resonators CROW. The degradation in the response of the largest number of resonators CROW can be due to the backscattering effect [77] induced by waveguide sidewall roughness. Coherent backscattering, originated by multiple round trips in the resonators, increases with the square of the effective group index of the cavity and can dramatically affect the behaviour of the CROW devices.

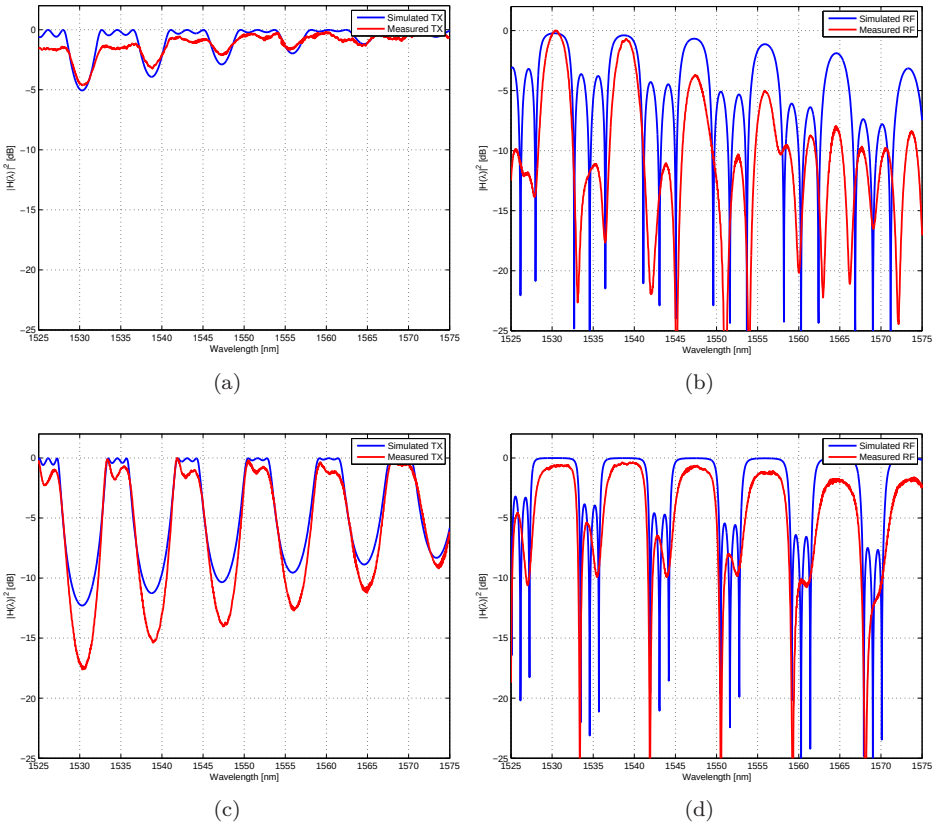

Figure 4.13: Simulated (blue) and measured (red) spectra of a 3 racetrack resonator uniform CROW (a)(b) and apodized with the longitudinal offset technique (c)(d). The transmission responses are depicted in (a) and (c) and the reflection responses in (b) and (d)

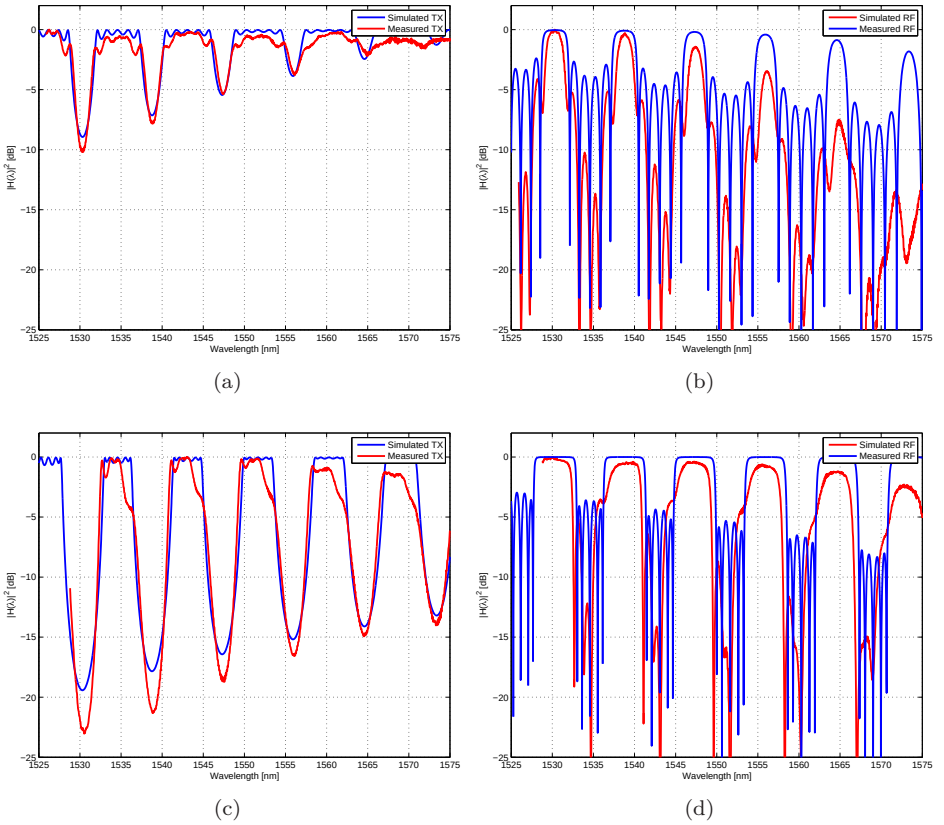

Figure 4.14: Simulated (blue) and measured (red) spectra of a 5 racetrack resonator uniform CROW (a)(b) and apodized with the longitudinal offset technique (c)(d). The transmission responses are depicted in (a) and (c) and the reflection responses in (b) and (d)

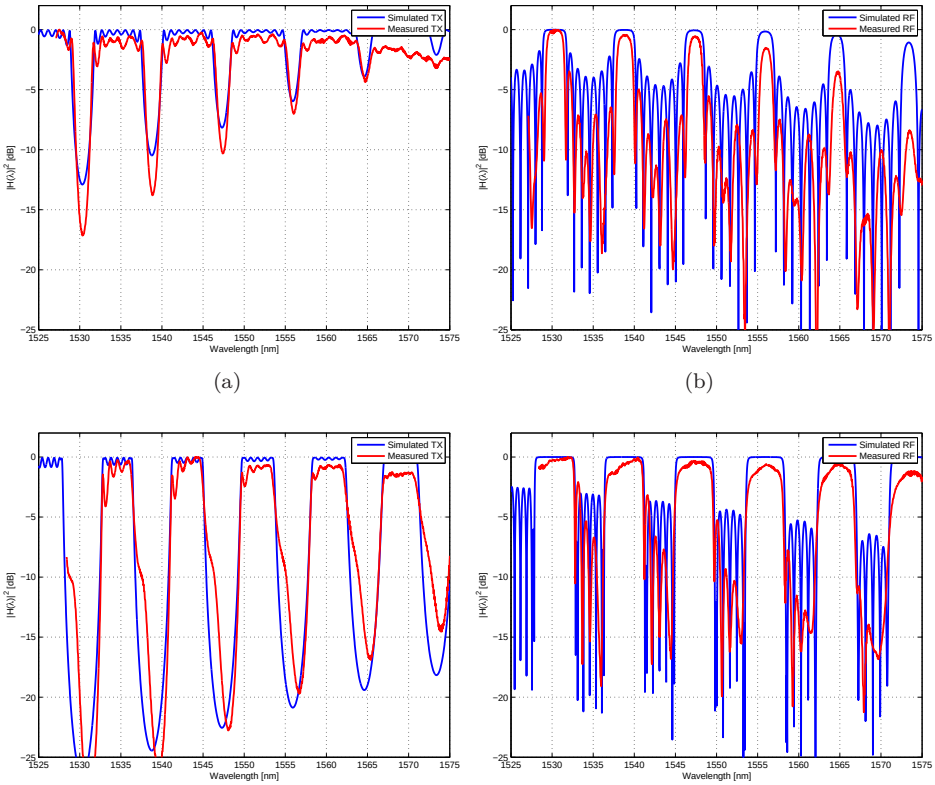

Figure 4.15: Simulated (blue) and measured (red) spectra of a 7 racetrack resonator uniform CROW (a)(b) and apodized with the longitudinal offset technique (c)(d). The transmission responses are depicted in (a) and (c) and the reflection responses in (b) and (d)

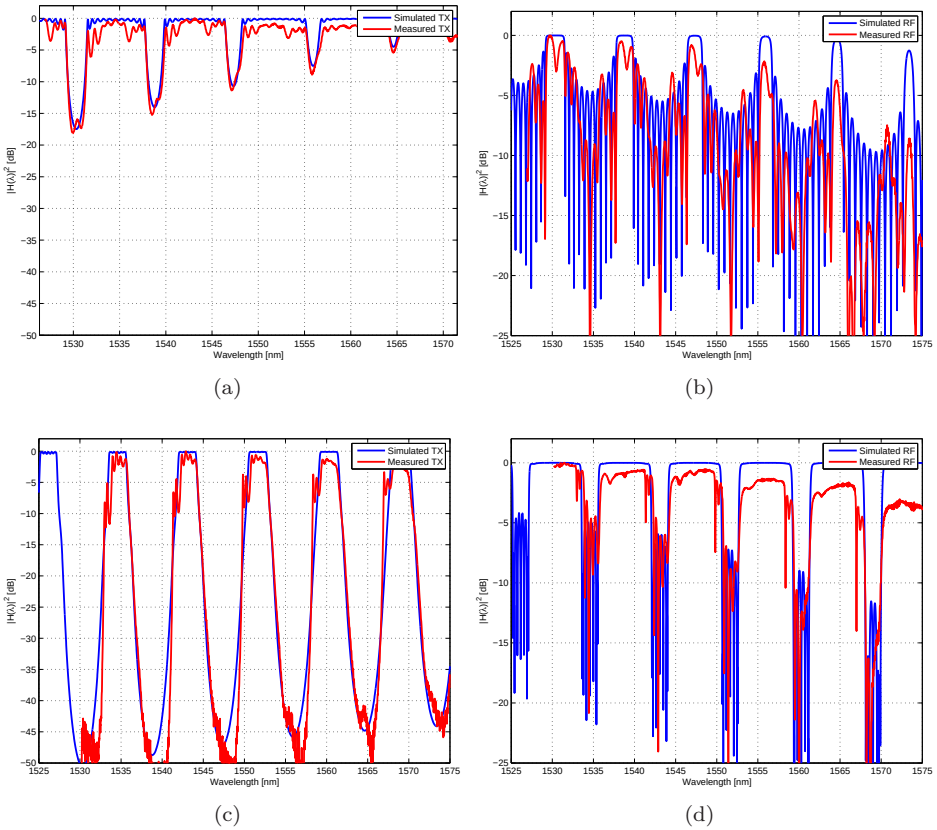

Figure 4.16: Simulated (blue) and measured (red) spectra of a 11 racetrack resonator uniform CROW (a)(b) and apodized with the longitudinal offset technique (c)(d). The transmission responses are depicted in (a) and (c) and the reflection responses in (b) and (d)

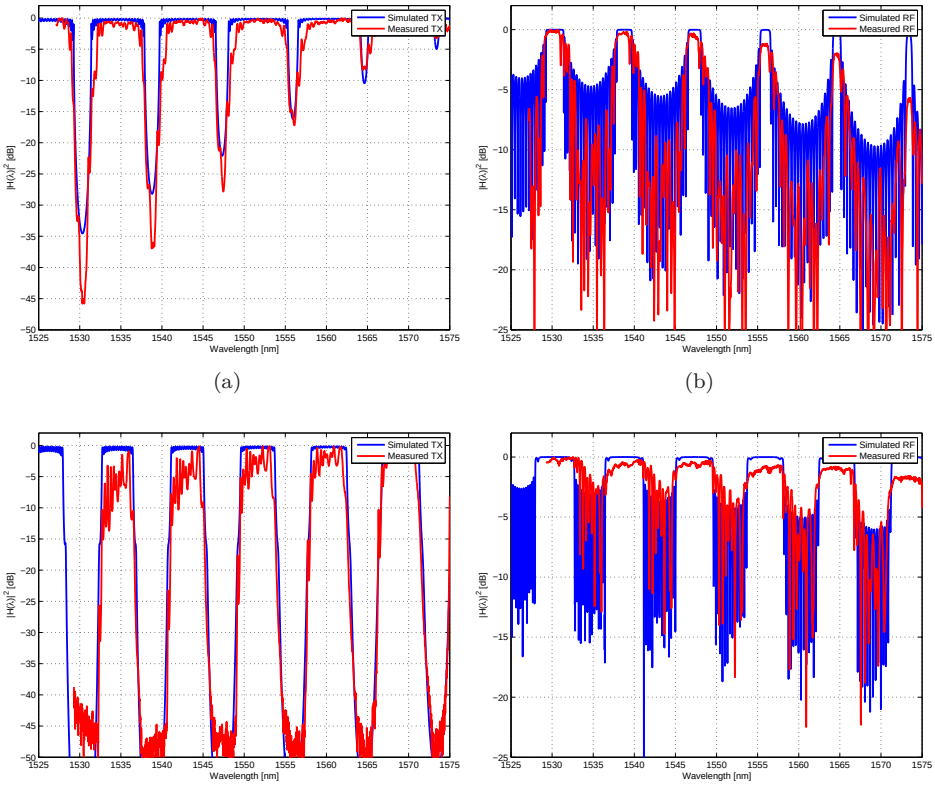

Figure 4.17: Simulated (blue) and measured (red) spectra of a 21 racetrack resonator uniform CROW (a)(b) and apodized with the longitudinal offset technique (c)(d). The transmission responses are depicted in (a) and (c) and the reflection responses in (b) and (d)

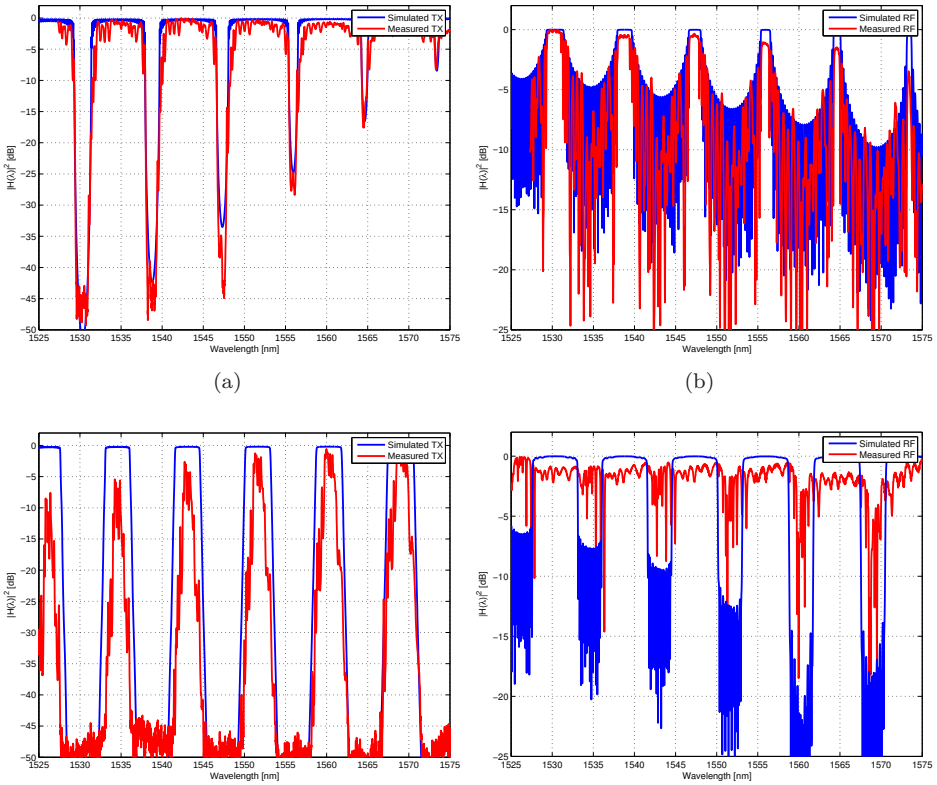

Figure 4.18: Simulated (blue) and measured (red) spectra of a 31 racetrack resonator uniform CROW (a)(b) and apodized with the longitudinal offset technique (c)(d). The transmission responses are depicted in (a) and (c) and the reflection responses in (b) and (d)

4.5 Conclusions

In this chapter, the design, fabrication and characterization of CROW devices has been presented. The design methodology has been described from the basic building block, the waveguide, to the final CROW device. The designed building blocks have been presented together with fabrication results. The results of the fabricated devices characterization have been compared with the theoretical predictions and they are in excellent agreement. CROW devices from two different fabrication runs have been presented: in the first run the apodization of the CROW devices has been applied to the cross coupling coefficients; in the second run the apodization has been impressed on the direct coupling coefficients. The results presented have shown that in the first run the ripples on the transmission passband of the CROW devices have been reduced through the apodization. The group delay characterization method and results have been also presented. The results from the second run showed the transmission and reflection characterization of CROW devices composed of up to 31 racetrack resonators. The fitting between simulation and measurement showed an excellent agreement. As predicted by theory, the out of band rejection has been increased in more than 40 dB in some cases at a cost of reducing the filter's passband.

Chapter 5
Applications

5.1 Introduction

The ability to engineer the dispersion properties of a CROW and especially the ability to realize ultra-slow group velocities paves the way for various applications such as delay lines, optical buffers and all-optical switching [78]. The group delay can be increased almost arbitrarily by increasing the perimeter of each resonator in the CROW and reducing the coupling between the resonators. The impact of these parameters on the group delay is as follows: reducing the coupling coefficient between adjacent resonators increases the time it takes for the light to tunnel from one resonator to its neighbour; increasing the perimeter, which is equivalent to elongating the optical path in the resonator, increases the roundtrip time. Both actions effectively increases the pulse life-time in each resonator, giving rise to a slower propagation velocity. The significant slowing down of light that can be achieved by reducing the FSR and the coupling constant is not accomplished without drawbacks. Reducing the coupling (or increasing the radius) decreases the available bandwidth of the pass-band. A smaller coupling ratio implies that the light circulates longer in each resonator and thus a stricter tolerance is imposed on the deviation of the optical frequency from the resonance frequencies of the resonators. In addition to reducing the usable bandwidth, reducing the coupling (or the FSR) may increase the overall loss in the CROW. The more times light circulates in each resonator the larger the loss experienced by the pulse as it propagates along the CROW.

Optical buffers

There have been few progresses in the field of optical buffers employing CROWs: In the work of Tucker et al. [79], the capabilities and fundamental limitations of CROW based optical buffers were introduced. Vlasov et al. demonstrated a 100 resonator CROW [9] where group delays exceeding 500 ps were achieved in a

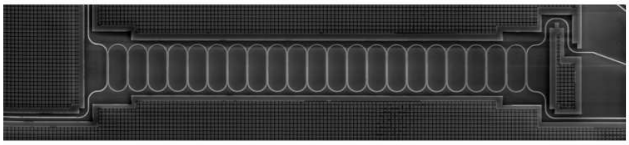

(a)

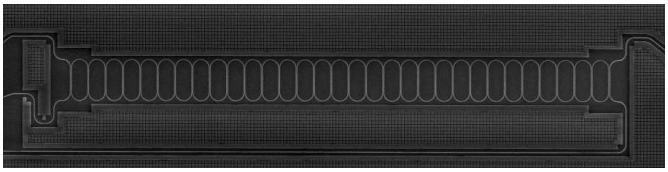

(b)

Figure 5.1: SEM images of a 21 racetrack resonators uniform CROW (a) and a 31 racetrack resonators uniform CROW.

device with a footprint below 0.09 mm^2 and a fractional group delay exceeding 10 bits for bit rates as high as 20 Gbps [80]. Ideally, an optical buffer should have not only a large delay, but the delay should be constant over a broad bandwidth with low insertion loss. However, there is a constant delay-bandwidth product determined by the physical mechanism underlying the delay [81]. The delay-bandwidth product is a measure of the number of bits that can be stored in the buffer. For buffers based on resonators the delay-bandwidth product is typically less than one. The delay increases linearly with the number of resonators but losses increase as well. This is the main limitation when employing CROW devices as optical buffers.

Despite the limitations found by previous studies, an experimental demonstration of the optical buffering with CROWs was carried out. The CROWs shown in Fig. 5.1 were designed, fabricated and characterized. The experimental setup was the following: An optical transmission system (OTS) from Tektronix (Tektronix OTS9000) to generate a 10Gb/s PRBS SDH frame has been employed. The PRBS signal has been introduced in 3 different structures: A straight waveguide, a 21 racetrack uniform CROW and a 31 racetrack uniform CROW. Figures 5.1-a and 5.1-b show the CROW devices employed in this experiment. The resulting signal has been captured in a digital sampling oscilloscope provided with an optical sampling module. The experimental setup is shown in Fig.5.2. The PRBS signal is first coupled in and out the chip through the grating couplers, afterwards the output signal is amplified with an EDFA and photodetected in the DSA. The recorded traces in the 3 structures are shown in Fig.5.3. The straight waveguide is used as reference for measuring the relative delay introduced by the CROW structures. The delay introduced by the 21 racetrack CROW is 14 ps and in the case of the 31 racetrack CROW is 20 ps. This results are in good agreement with the theoretical predictions

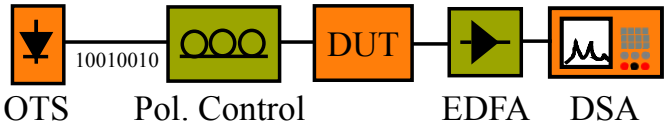

Figure 5.2: Schematic of the employed elements.

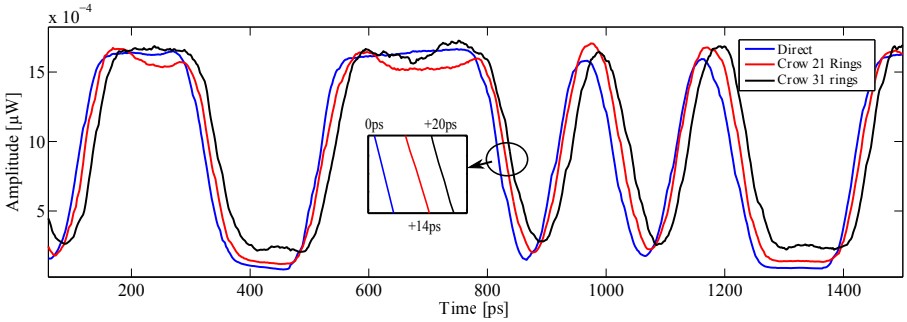

Figure 5.3: Measured digital traces.

Nevertheless, there are other fields of application where the delay characteristics of CROW devices can be exploited, i.e. the Microwave Photonics field [82].

Microwave Photonics

Microwave photonics (MWP), a discipline which brings together the worlds of radio-frequency engineering and optoelectronics, has attracted great interest from both the research community and the commercial sector over the past 30 years and is set to have a bright future. The added value that this area of research brings stems from the fact that, on the one hand, it enables the realization of key functionalities in microwave systems that either are complex or even not directly possible in the radio-frequency domain and, on the another hand, that it creates new opportunities for information and communication (ICT) systems and networks [83]. For the last 25 years, MWP systems and links have relied almost exclusively on discrete optoelectronic devices and standard optical fibers and fiber-based components which have been employed to support several functionalities like RF signal generation, distribution, processing and analysis. These configurations are bulky, expensive and power-consuming while lacking in flexibility. A second generation, termed as Integrated Microwave Photonics (IMWP) and which aims at the incorporation of MWP components/subsystems in photonic circuits, is crucial for the implementation of both low-cost and advanced analog optical front-ends. With photonic integration, one can achieve a reduction in footprint, inter-element coupling losses, packaging cost as well as power dissipation since a single cooler can be used for multiple functions. Thus, the MWP functionalities can be brought a step closer towards real applications and subsequently commercial marketplace.

Reconfigurable optical delay lines (ODL) and wideband tunable phase shifters have primary importance in a number of MWP signal processing applications like optical beamforming and MWP filters. The simplest way for generating delay in the optical domain is through physical length of optical fibers. However, this can become rather bulky. For this reason, integrated photonic solutions are used. A number of approach have been reported over the years. For example, optical switches can be used to provide discretely tunable delay by means of selecting waveguides with different propagation length. This approach has been demonstrated using devices in silica [84] and in polymer [85]. Others proposed tunable delay based on optical filters [86]. For example cascaded ORRs have been demonstrated for tunable delays in silica [87], TriPleX [88], silicon oxynitride (SiON) [89], and SOI [90, 91].

Besides delay, phase shifting is also attractive for a number of signal processing applications. For narrowband phase shift, SOI ring resonators have been used as widely tunable RF phase shifters [7, 92]. Others used semiconductor waveguides in SOAs [93, 94], or a microdisk in hybrid III-V/SOI platform [95]. To have a complete signal processing capabilities, it is attractive to obtain both delay and phase shift at different signal frequency components. This is widely known as the separate carrier tuning (SCT) scheme, proposed by Morton and Khurgin [96]. Chin et al. demonstrated this functionality in optical fiber using the stimulated Brillouin scattering (SBS) effect [97]. Burla et al. [98] demonstrated the SCT scheme together with optical single sideband filtering monolithically integrated in a single chip.

The delay and phase shifting are the basis for applications like filtering and beamforming. In the next section, the design, fabrication and characterization of the core components conforming a narrow bandwidth beamformer in Silicon on Insulator technology are shown.

5.2 Microwave photonics beamformer based on ring resonators and AWGs

Phased-array antennas have been the subject of intense development due to a number of advantages over mechanically steered antennas such as steering speed and reliability [99]. However, conventional phased-array antennas have been hampered by issues of size, weight, cost and complexity. Due to these and other factors, there has been an increased effort to implement some of the subsystems of a phased-array antenna optically. The last developments in optical beamforming networks have been accomplished employing state of the art integration technologies that allow for miniaturization of the devices.

Several approaches exist in the literature for optically controlled tunable beamformers, amongst them some using all-pass ring resonators. In the work by Adams et al. [100] tunability is achieved by means of the thermo-optic effect with heaters. Chang et al. [101] use the thermal nonlinear effect of Silicon. However, despite the change in refractive index with the temperature can be large (for instance in

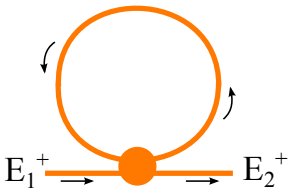

Figure 5.4: All-pass ring resonator schematic. E_1^+ and E_2^+ represent the input and output electric fields respectively

Silicon $\partial n/\partial T = 1.86 \cdot 10^{-4} K^{-1}$ [102]), the response times are not better than 1 μs [103]. The approach presented in this section is based in our previous work [104] where the phase shift is accomplished by changing the frequency of a tunable laser within a resonance of a ring resonator. This approach is limited by the switching speed of the tunable lasers, which are well below the nanosecond scale [105].

5.2.1 All-pass ring resonator based microwave phase shifter

An all-pass ring resonator is schematically shown in Fig. 5.4. Using the formulation from chapter 2, the field transfer function can be expressed as:

$$H(\beta L) = \frac{E_2^+}{E_1^+} = \frac{t - \gamma e^{-(\alpha/2 + j\beta)L}}{1 - t^* e^{-(\alpha/2 + j\beta)L}} \tag{5.1}$$

Consider a single-side band (SSB) optical signal, with optical carrier frequency f_c and radio frequency (RF) f_{RF}. The signal is filtered using an all-pass ring-resonator, hence a relative phase shift is induced between the optical carrier and the RF sub-carrier frequencies [5] [11]. To derive the device induced phase shift, and power penalty, a transmitter model where modulation is linear, as in [106] will be assumed for simplicity. The expression for the optical electric field amplitude (arbitrary power) at the input of the resonator is given by:

$$E_1^+(t) = e^{-j\omega_o t} + m e^{-j(\omega_o + \omega_{RF})t} \tag{5.2}$$

as the ring-resonator is a linear and temporal invariant system:

$$E_2^+(t) = H(\omega_o) e^{-j\omega_o t} + m H(\omega_o + \omega_{RF}) e^{-j(\omega_o + \omega_{RF})t} \tag{5.3}$$

Assuming a photodetector with unit responsivity:

$$\begin{aligned} i(t) &= E_2^+(t) E_2^{+*}(t) = |H(\omega_o)|^2 + m^2 |H(\omega_o + \omega_{RF})|^2 \\ &+ m\ H(\omega_o) H^*(\omega_o + \omega_{RF}) e^{j(\omega_{RF})t} \\ &+ m\ H^*(\omega_o) H(\omega_o + \omega_{RF}) e^{-j(\omega_{RF})t} \end{aligned} \tag{5.4}$$

Defining $\Delta\phi_{RF} = \angle H(\omega_o) - \angle H(\omega_{RF})$ the RF terms can be grouped in:

$$i_{RF}(t) = m\, |H(\omega_o)|\, |H(\omega_o + \omega_{RF})| \cos(\omega_{RF} t + \Delta\phi_{RF}) \tag{5.5}$$

The ring resonator response is periodic, hence the phase shift depends on both the position of the optical carrier within the spectral period (Free Spectral Range) and the relative difference between the optical carrier and RF sub-carrier frequencies. The response of a ring resonator limited to a FSR span is shown in Fig. 5.5-(a) for several round trip losses values, where δ is defined as:

$$\delta = \frac{f - f_0}{FSR} \tag{5.6}$$

with f the frequency in Hz, and f_0 the resonator resonance frequency. Fig. 5.5-(b) is a zoomed version of the phase illustrating the phase shifting principle with the black and blue arrows. For a given optical carrier (circle lines in the figure) δ_c and accompanying RF sub-carrier (arrow lines in the figure) $\delta_c + \delta_{RF}$, by tuning the former, the relative phase shift changes, due to the shape of the phase response of the all-pass ring resonator. A power penalty takes place, due to the non-flat power transfer function in practical devices as in Fig. 5.5-(a). The penalty depends on the RR coupling constant and round trip losses. In the following section, the beamformer device and the design methodology is described.

5.2.2 Tunable beamformer concept

The beamformer device is depicted in Fig.5.6 and consists of N tunable lasers multiplexed by an Nx1 AWG. The lasers are externally modulated by a dual-drive Mach-Zehnder Modulator (MZM), filtered with an all-pass ring resonator and then demultiplexed by an 1xN AWG. The phase shift for each antenna can be selected by tuning the corresponding laser in the range allowed by the passband of the AWG, and within the ring resonator FSR. The spectral response of the all-pass ring resonator is periodic with period FSR:

$$FSR = \frac{c}{n_g L_c} \tag{5.7}$$

where c is the speed of light in vacuum, n_g is the group refractive index of the waveguides and L_c the RR cavity length. By tuning each laser within the FSR of a different resonance, the phase shift for each antenna is set. For the phase shifter design it is useful to partition the ring resonator FSR as shown in Fig. 5.7. The maximum phase shift ($\Delta\phi_{max}$ in the figure) is given by both a) the spectral separation of the optical and RF signals and b) the phase response slope. From the figure, to be able to change $\Delta\phi$ in the range [0,$\Delta\phi_{max}$] by tuning the laser, $\Delta\delta_1 \leq \delta_{RF} \leq \Delta\delta_2$. The pair $\Delta\phi_{max}$ and $\Delta\delta_1$ depends on the slope of the phase transfer function around resonance. This slope depends on the power coupling constant K between the ring and the access waveguide. The lower the K value, the higher the slope, and the wider the flat regions in the phase transfer, out of resonance [13]. A steep slope turns into a small fraction of the FSR ($\Delta\delta_1$) needed to attain the targeted maximum phase shift ($\Delta\phi_{max}$). The maximum achievable phase shift for a single ring device will be always lower than 360 degrees with this configuration, but this can be solved by using multi-stage resonators [11].

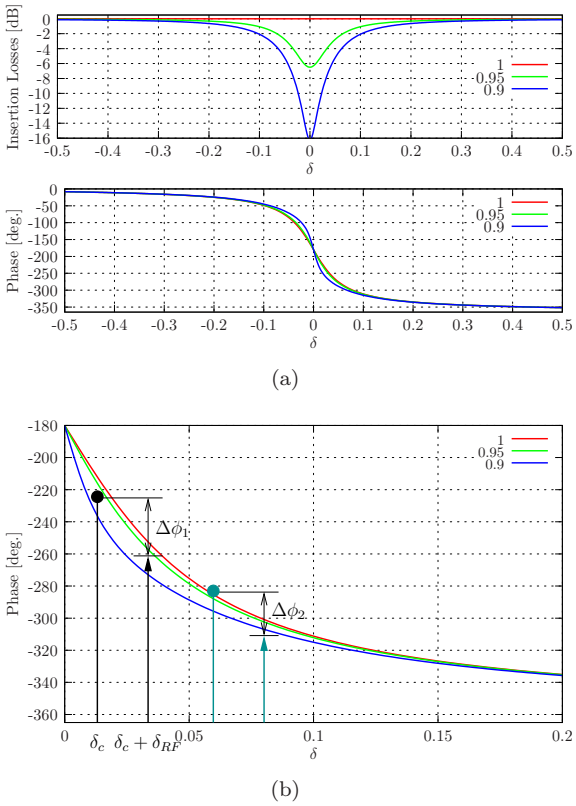

Figure 5.5: Power transmission and phase (a) responses of an all-pass single RR, for different round trip losses values and coupling constant $K = 0.25$ (loss-less coupler, $\gamma = 1$) vs. δ. (b) is a zoomed version of the phase with optical and RF carriers to illustrate the phase shifting principle.

The AWG frequency channel spacing must be designed to be equal to an integer multiple of the ring resonator FSR. Moreover their bandwidth must be at least equal to the ring resonator FSR as depicted in Fig. 5.8. A critical part of the design is the spectral alignment of the AWG multiplexer and demultiplexer. Either individual thermal tuning or an advanced design with a single 2Nx2 AWG in loopback configuration [107] can solve the problem. Fig. 5.9 shows the sketch of a linear array of antennas. The directional characteristics of a lineal N-isotropic-element phased array can be expressed through the array factor [108]:

$$FA(\Theta) = \sum_{n=0}^{N-1} I_n e^{j(k_z d_n + \alpha_n)} = \sum_{n=0}^{N-1} I_n e^{j(k d_n cos\Theta + \alpha_n)} \tag{5.8}$$

with I_n the current fed to each element, $k = 2\pi/\lambda$ with λ the RF wavelength, d_n the distance between elements of the array and Θ the angle of radiation. An

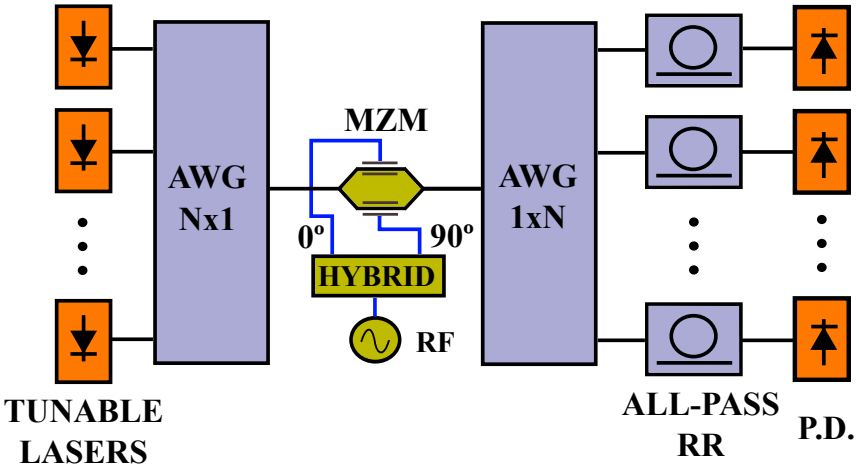

Figure 5.6: Schematic of the integrated beamformer.

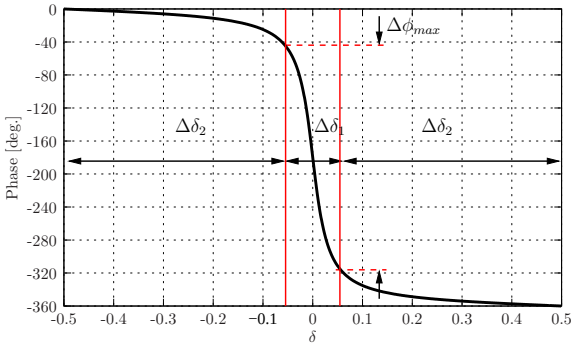

Figure 5.7: Ring resonator phase partitioning for the phase shifter design vs. δ.

equidistant array ($d_n = n \cdot d$) and a progressive phase are assumed for simplicity. Hence, considering the first element has null phase, $\alpha_n = n \cdot \alpha$. Therefore, the array factor can be expressed as:

$$FA(\psi) = \sum_{n=0}^{N-1} I_n e^{jn\psi} \tag{5.9}$$

with $\psi = kdcos\Theta + \alpha$ periodic, with period 2π.

A 4 element beamformer design based in a single ring all-pass section designed in Silicon-On-Insulator is presented. The design is based in a ring resonator with waveguide cross-section of 226 x 525 nm. reported by Dulkeith et al [72]. This waveguide has a group index of 4.25 for TE mode near 1.55 μm wavelength and propagation losses of 4 dB/cm. To start, the pair $\Delta\phi_{max}$ and f_{RF} are set to be to 270 degrees and 40 GHz respectively. One solution to partition the FSR

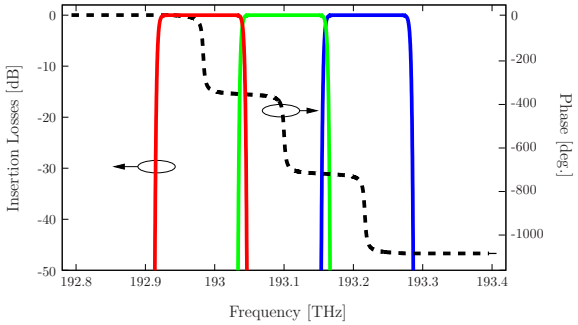

Figure 5.8: All-pass single ring resonator phase in 3 periods and flat-top designed AWG response in their corresponding channels.

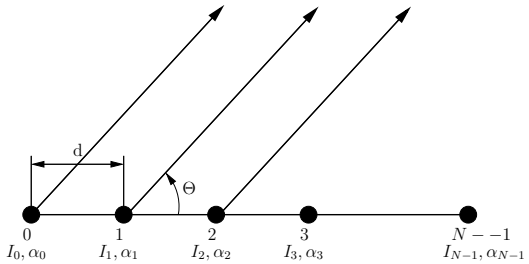

Figure 5.9: N-element linear array.

for simplicity can be $\Delta f_2 = \Delta f_1 = f_{RF} = 40GHz$ leading to a FSR of 120 GHz. Consequently, using eq. (5.7) the cavity length results in 587.83 μm. The coupling constant value must be chosen to match the phase shift of 270 degrees and 40 GHz bandwidth requirements. Using the formulation of [13] a value of K=0.3 is found.

Figure 5.10 shows the induced phase shift between the optical and RF signals while the laser is swept inside an AWG channel. A typical laser step of 10 pm (1.25 GHz) is assumed, though many commercially available tunable have smaller steps. The smaller the laser step, the higher the accuracy of the device beamforming, in terms of both the pointed direction and the available (discrete) set of directions. In Fig. 5.10 96 positions corresponding to 1.25 GHz steps within a 120 GHz range are shown. Note the aforementioned laser step trade-off, for instance from laser step 16 to 17 there is a phase increment of more than than 30 degrees. The AWGs passbands are designed [109] to have a bandwidth equal to the RR FSR as shown in Fig.5.8. The full device has been modelled with commercial software [110].

Tables 5.1 and 5.2 summarize the laser position of each channel as well as the RF phase detected in order to obtain the radiation directions of $\Theta = 30$ and $\Theta = 60$ degrees, that require a progressive phase shift of $\alpha = -155.84$ and $\alpha = -90$ degrees respectively.

Figure 5.11 shows the ideal radiation diagram of the 4 isotropic elements linear

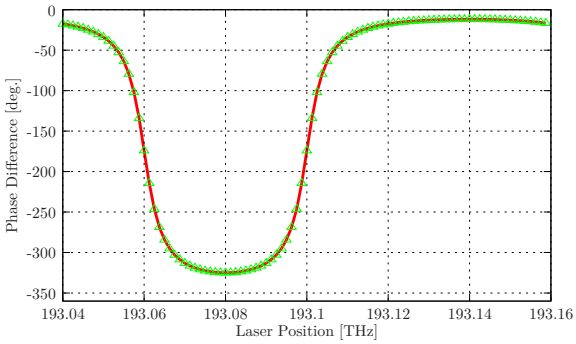

Figure 5.10: Induced phase shift for a 40 GHz RF signal in one channel vs laser position in the ring FSR. The triangle symbols indicate the tunable laser discrete steps.

$\Theta = 30$, $\alpha = -155.84$ degrees.				
Laser Number	1	2	3	4
f_c [THz]	193.04000	193.18000	193.31875	193.46125
Phase [deg.]	-17.5106	-174.1217	-324.8353	-133.9504
Losses [dB]	0.102	2.678	0.165	2.361

Table 5.1: Laser positions for the required phase shift and steering direction $\Theta = 30$ degrees.

array for several progressive phases and the diagram obtained with the simulated device. The main lobe angular mean deviation from theoretical calculations is 0.923 degrees but can easily improved by reducing the tunable laser step. Moreover, the diagram shows a reduced radiation efficiency in the main lobe due to the non-flat ring resonator power transfer function. This could be compensated if the device is implemented in InP technology, with a Semiconductor Optical Amplifier (SOA) placed before each photodetector.

$\Theta = 60$, $\alpha = -90$ degrees.				
Laser Number	1	2	3	4
f_c [THz]	193.05125	193.17875	193.30125	193.42750
Phase [deg.]	-38.6352	-133.9504	-214.2765	-302.9455
Losses [dB]	0.376	2.361	2.363	0.494

Table 5.2: Laser positions for the required phase shift and steering directions of $\Theta = 60$ degrees.

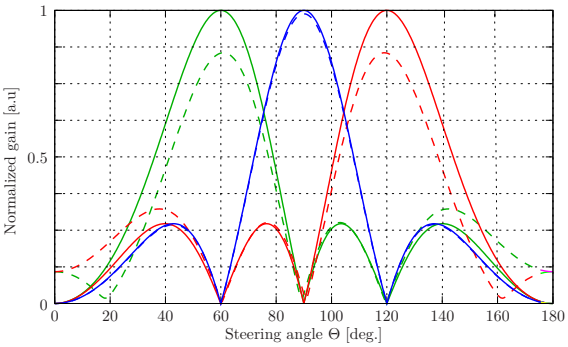

Figure 5.11: Radiation diagram vs. Θ [deg.] for a uniform linear 4 element array, for different α values and $d = \lambda/2$

5.3 Design and fabrication in SOI technology

The fabrication of these devices was included in the second run presented in the previous chapter. The all-pass racetrack resonator has been designed to have a free spectral range (FSR) of 0.75 nm at a wavelength of 1.55 μm and a coupling constant of $\kappa = 0.5$. The racetrack has a perimeter of 711 μm and a straight coupling section of 15 μm. The gap between the racetrack and the access waveguides is 200 nm. The coupling constant together with the expected propagation losses (around 3 dB/cm) will define the spectral width of the notch in resonance and the $\Delta\lambda_{FWHM}$.

These values have been calculated accordingly to have a $\Delta\lambda_{FWHM}$ and a phase transition that allows to accomplish the maximum phase shift required by design between the optical carrier and the RF subcarrier. At the same time, the on-resonance notch depth has been minimized to avoid extra insertion losses. The beamformer has been designed to introduce a maximum phase shift of 270 degrees for SSB modulated signals up to 40 GHz.

The AWG has been designed with 4 input and 4 output channels. The additional channels at the input side are used for testing purposes. The AWG channel spacing has been set to 3.2 nm and with a Gaussian response. The FSR of the AWG has been set to 22.4 nm, that is 7 times the channel spacing. This increased FSR will reduce the imbalance between channels in the AWG, at the expense of an increased footprint. With this channel spacing at least 4 resonances of the ring resonator are located within the passband of the AWG.

The devices were fabricated in a 200 mm SOI wafer with a Silicon layer thickness of 220 nm on top of a 2 μm BOX employing 193 nm deep UV lithography. The waveguides, the ring resonators and the AWG's star couplers have been defined with a deep etch process (220 nm). For the input/output grating couplers and for all the waveguide apertures to the slab region of the star couplers in the AWG, an extra shallow etch process (70 nm) has been employed to reduce the insertion

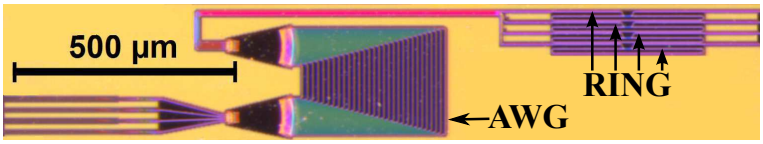

Figure 5.12: Micrograph of the fabricated device.

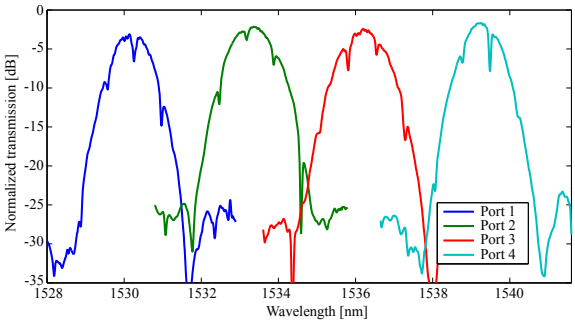

Figure 5.13: AWG and all-pass racetrack resonator combined spectral response

losses [111]. The AWG footprint is 250 μm x 515 μm using 5 μm waveguides bends. Fig. 5.12 shows a micrograph of the fabricated device. The inputs and outputs are routed from/to a grating coupler, not shown in the figure, to couple light into/out of the device. The fabrication process did not include thermo-optic heater, hence the all-pass resonators in this device cannot be individually tuned.

5.3.1 Characterization

The chip was tested using standard monomode fibers positioned at 80° angle of the chip surface, aligned to the Grating Couplers. The Grating Couplers have an efficiency of about 30%. A tunable laser was used to measure the transfer function of the AWG+resonator. All the measurements are normalized to the measurement of a reference straight waveguide on the same chip. Hence the results do not include the Grating Coupler losses and represent on-chip figures. Fig. 5.13 shows the power transfer function for each channel. The on-chip insertion losses are below 3 dB in the four channels and the non-uniformity between channels is 1 dB. The crosstalk in the worst case is 20 dB. In every passband of the AWG, at least four resonances of the all-pass racetrack resonator can be appreciated.

Fig. 5.14 shows a single channel characterization with the spectral and phase response. The phase characterization has been carried out with the modulation phase shift method [112]. From Fig. 5.14-b a 360° phase shift on every resonance of the all-pass ring resonator can be observed. With the current FSR, a maximum SSB RF modulation frequency of 40 GHz can be employed, achieving at most 270° phase shift between the optical carrier and the SSB RF sub-carrier.

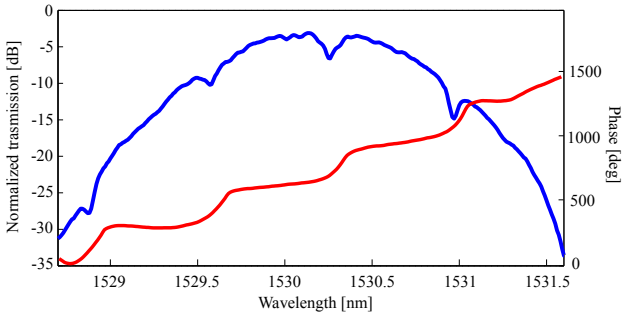

Figure 5.14: Amplitude and phase response in a single channel of the device.

5.4 Conclusions

Among the existing applications for CROW devices, the optical buffering was explored in a first term. This application was discarded given the fundamental limitations found. For this reason the work was focused to an application in the MWP field. A novel optical beamformer architecture based in an all-pass ring resonator has been presented where the reconfiguration accuracy and time depend on the tunable laser characteristics. The former is easily around 1 pm, therefore providing a nearly continuously tunable device, while the later is in the nanosecond time scale. The device can provide phase shifts up to 360 degrees with a multistage resonator design. To optically control the amplitude of the radiant elements, and hence the sidelobe level and null position in the radiation directions, the device can be completely designed in InP with semiconductor optical amplifiers. The AWG-based demultiplexer and the phase shifting sections have been fabricated in Silicon On Insulator and lately characterized. The measurements show a good agreement between design and fabrication.

Chapter 6
Conclusions and future work

6.1 Conclusions

The realization of all the objectives proposed at the beginning of this Ph.D. has been attained with the following contributions and conclusions:

- A TMM formalism has been developed in Chapter 2 for the analysis of CROW and SCISSOR structures. The apodization of the coupling coefficients in the unit cells of serial and parallel coupled resonator waveguide devices has been introduced in section 2.3 as a mean to improve the bandpass characteristic of their transfer functions. The apodization of both SCISSOR and CROW structures has been discussed for several windowing functions and sidelobe/ripples suppression in both structures demonstrated respectively. To conclude the chapter, in section 2.4 a novel synthesis algorithm based in the layer aggregation method has been adapted to coupled resonator optical waveguides. A procedure to link the contribution of each cavity to the impulse response at every time has been derived. The procedure has been applied to the synthesis of CROWs, starting from targeted transfer functions. An excellent match between the targeted and synthesized responses has been demonstrated for worst case convergence parameters.

- Chapter 3 reported a novel technique for controlling the coupling between the resonators in CROW structures. The technique, based in a longitudinal offset between resonators, alleviates the tight requirements in the fabrication stage typically limited by the lithographic resolution. The technique is most suitable for racetrack resonators given the inherent straight coupling section of this type of resonator. The sensitivity is increased critically by using the longitudinal offset technique despite the increase in the footprint of the final devices. The technique has been introduced in section 3.2 and demonstrated numerically through BPM in section 3.3 and through TMM simulations of several CROW devices in section 3.4.

- In chapter 4, the design, fabrication and characterization of CROW devices implementing the longitudinal offset technique has been presented. The details of the fabrication technology are given in section 4.2. In section 4.3, the CROW devices are decomposed in its constituent parts and individually analysed in detail. Finally, the results from two fabrication runs have been presented in section 4.4. The devices have been designed and fabricated in Silicon On Insulator through the ePIXfab platform. Both fabrication runs included CROW devices implementing the apodization through the longitudinal offset technique. In the first run the apodization is impressed over the cross coupling coefficient whilst in the second run is applied to the direct coupling coefficients. The results of the fabricated devices characterization have been compared with the theoretical predictions and are in excellent agreement. The technique has been patented through the Technology Transfer Office from the Universitat Politècnica de València at a national level and licensed to the UPV Spin-Off company VLC Photonics S.L.

- The last chapter of this thesis has been devoted to demonstrate the applications of CROW devices given the delay and phase-shifting characteristics of these structures. In a first term, the delay response of the CROW devices has been experimentally investigated through digital signal transmission experiments. The results matched those previously demonstrated by the work of Vlasov et al. [9] about optical buffers employing CROW devices. The results obtained showed the same limitations in terms of bandwidth and delay that make difficult the usage of CROWs as optical buffers. At the sight of these results, the research was focused in the field of microwave photonics. A novel optical beamformer architecture based in all-pass ring resonators has been presented. The device can provide phase shifts up to 360 degrees with a multi-stage resonator design. To optically control the amplitude of the radiant elements, and hence the sidelobe level and null position in the radiation directions, the device can be completely designed in InP with semiconductor optical amplifiers. The AWG-based demultiplexer and the phase shifting sections have been fabricated in Silicon On Insulator and lately characterized. The measurements show a good agreement between design and fabrication.

6.2 Future work

After the work developed in this thesis, there are some open research lines that may be continued:

- Study the fabrication reproducibility of the devices shown in Chapter 4:
  - Within-die non-uniformity
  - Non-uniformity over the wafer
  - Inter-wafer non-uniformity

- Develop robust coupling schemes tolerant to fabrication imperfections.
- Incorporate tuning elements to the CROW structures in order to compensate deviations in fabrication.
- Test the longitudinal offset technique in different fabrication platforms.

Appendices

Appendix A

Integrated optics devices modelling using High Performance Computing and parallel Finite Differences in the Time Domain algorithms

The fast and efficient exchange of information in actual society is recognized as one of the most important catalysts for development.The development and social adoption of the Internet as the principal mean for long distance fast communications, is supported by ground infrastructures that mainly rely on the exchange of light signals using optical fibers. The invention of the laser on the 60's, enabled the science of mastering light signals, processing and using them for ultra-long distance communications. Technology developments in the field are driven by daily increasing demands on the amount of information to be exchanged. Therefore, telecommunication providers face the trouble of squeezing their available infrastructure to the maximum. Moreover, more and more physical space is needed to settle information transmitters, receivers and rely data stations, with increasing electric power consumption. To cope this problem, the field of integrated optics [1] aims at grooming several functionalities for such data stations in the smallest space and with the minimum power consumption.

Integrated optics circuits are in shape devices similar to the widespread consumer electronics devices, as the printed circuit boards one can find inside a home computer. The very significant difference is that the latter use electric signals, whilst the former use optical signals to work with. This difference makes the subject of integrated optics a complex science involving from chemical and matter sciences and processes, to build the support boards for the circuits, to design engineering and signal processing to master the light therein.

Amongst the required steps to produce an integrated optics component, i.e. theoretical conception, device simulation and modelling, device design, component fabrication and characterization, device modelling plays a crucial role. The more precise and close to the physical phenomena taking place in these devices, the more efficient the device production cycle, from theory to availability, will be.

There is a vast variety of integrated optics devices [1], and therefore different modelling approaches [113] [114]. One of the most computationally intensive problems in this field is to model devices without assuming a preferential propagation direction for the light signals on the devices, also known as omni-directional propagation. This problem is usually addressed with Finite Differences in the Time Domain (FDTD) algorithm, that solve the Maxwell equations in a given computational discretized cell. The FDTD algorithm calculates iteratively the electromagnetic field components for all the computational cell points every time step. The computational requirements for these problems depend on the size of the cell and the nature of the devices being modelled. However, the FDTD algorithm can be parallelized, and therefore High Performance Computing (HPC) computer clusters can be used.

In this section we present the use of the FDTD software MEEP from MIT [115] applied to integrated optics devices. The modelled devices are subject of research in our research group within several research projects.

A.1 MEEP

MEEP is an open source software FDTD project. The acronym stands for "MIT Electromagnetic Equation Propagation". This software has been developed [115] at the Massachusetts Institute of Technology and it is maintained by Steven G. Johnson and others. Detailed information can be found in the MEEP MIT website [116]. To summarize briefly:

- Free software under the GNU/GPL.
- Simulation in 1d, 2d, 3d, and cylindrical coordinates.
- Distributed memory parallelism on any system supporting the MPI standard.
- Exploitation of symmetries to reduce the computation size.
- Arbitrary material and source distributions.
- Field analysis including flux spectra, frequency extraction, and energy integrals.
- Multi-parameter optimization, root-finding, integration, etcetera.

In general all the FDTD methods, and in particular MEEP, present some strengths as its versatility and its capability to obtain the response of the system over a wide range of frequencies with a single simulation. Another advantage is the possibility

Structure	Cell [μm]	Step size [μm]	# Points	Memory [GB]
DBR	100x5x5	0.020	3.125e8	19
Ring resonator	25x20x5	0.020	3.9e8	24
Grating Coupler	500x20x5	0.025	3.2e9	190

Table A.1: Memory usage of the examples.

to obtain the E and H fields everywhere in the computational cell as they evolve in time, providing animated displays of the electromagnetic field movement through the model that are very useful in understanding what is going on in the model, and helping to ensure that the model is working correctly.

But the FDTD methods present also some weaknesses. The main drawback of these techniques are that, since FDTD requires that the entire computational domain be gridded, the grid spatial discretization must be sufficiently fine to resolve the smallest geometrical feature in the model. This leads to very large computational cells which requires huge amount of computer memory and very long simulation times. For instance, models with long, thin features, are difficult to model in FDTD because the high spatial resolution needed and the relatively large simulation cell leads to very long computational times and large memory requirements.

In order to address this very demanding computing requirements, access to high performance computing facilities is needed.

A.2 Computational requirements

Since the computational cell is discretized in MEEP in a two/three dimensional mesh, the number of points in the mesh as well as the memory/process time consumption increases exponentially when increasing the program accuracy.

This grid of points has multiple instances during simulations and they are used to store different parameters of the simulation as the material permittivity, electric and magnetic fields, dispersive properties of the materials, etc. Let's assume we have a 100x100x100 points grid. That is $1 \cdot 10^6$ points. Each point is stored into a variable of type double, consuming 8 bytes, so one instance of the grid will be near 8 MB. Typically, 3D simulations keep in memory a minimum of 8 instances of the grid, therefore the needed resources grow exponentially with the grid size.

Table A.1 shows the approximated memory usage for the examples shown in the next section.

As described in the previous section, the FDTD method solves Maxwell equations for each point in the grid on each time step. Typically, six field components are stored for each grid point and each field component update requires at least eight floating point operations. Thus, a 100x100x100 grid will require 1 million of points or 6 million field components. One complete update of this grid requires 48.000.000 floating point operations (48 MFLOPS).

At the sight of this brief discussion, it is clear that a HPC cluster is required for these problems for several reasons. First a single computer may have not enough memory to host the computational cell. Second, even in the case the problem can be addressed with a single computer in terms of memory, the computation time needed depends on the devices being modelled. For instance, some devices require the light to recirculate several times for the final solution to converge. And last but not least, even in the case that computing time and memory usage could be copped with a single computer, a single simulation run does not happen to provide the final results in most of the cases, therefore parameter sweeps and/or optimization are needed, so reruns are usually performed.

A.3 Usage examples

The following examples are just a sample amongst all the problems for which FDTD and HPC is needed for integrated optics. Thought all these problems have analytic models counterpart, they rely on simplifications that in most of the cases do not hold. It is in those cases where brute force electromagnetic simulations are needed.

A.3.1 Grating couplers

Currently, the in/out coupling of light from PIC to an optical fiber remains a serious issue. The large difference in dimensions between the fiber and the waveguides on a chip causes high insertion losses and high packaging costs.

The commonly used solution to couple light into a sub-micrometer waveguide is to directly focus the beam from a lensed fiber onto the end of the sub-micrometer waveguide at the chip edge (butt coupling). This technique introduces coupling losses typically higher than 12 dB.

A solution to overcome this high coupling losses is to use grating couplers [117] followed by a taper to adjust the lateral size of the incident beam to the sub-micrometer waveguide width. A grating coupler is a periodic variation of the waveguide height along its length. Due to this variation, a fraction of the light contained in the waveguide is radiated to the external medium. The main advantage of a grating coupler is the possible use of test devices everywhere on the PIC without any cleavage.

It is interesting to improve the grating coupler design in order to maximize its coupling efficiency [75]. For instance, there is a strong dependence between the grating coupler period and the angle in which light is radiated [117]. This improvement in the design can be done using a simulation tool, as the FDTD method provided by the MEEP software.

In Fig. A.1 a 2D view of a grating coupler is shown. The different grey levels indicate different materials (air -white-, silica -grey- and silicon -black-). The waveguide is 220 nanometers height and 50 micrometers long, and the thickness

Figure A.1: 2D side view of a grating coupler.

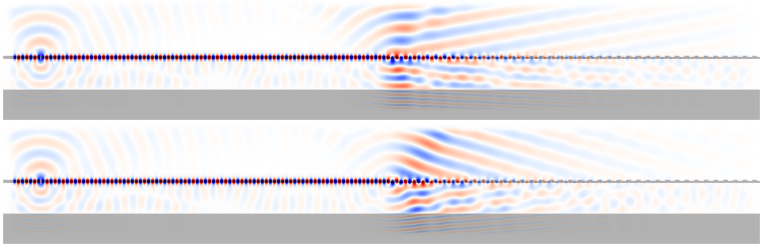

Figure A.2: 2D side view of light radiated from a grating coupler with period 540 nm (top) and 640 nm (bottom).

of the substrate layers is of 2 micrometers each. The grating coupler has a period of a few hundreds of nanometers and a depth of 70 nanometers.

In Fig. A.2 a 2D simulation of the EM fields radiated from a waveguide is shown, when the light arrives to the grating coupler. In this case, two different grating coupler periods have been chosen to illustrate the dependence of radiation angle on the period.

The dimensions of the 2D simulation cell are 50x10 microns and, in order to resolve the small features of the grating coupler, the resolution value is 25 nanometers. The amount of memory required to perform this simulation is of around 80 MB, and it takes around 10 minutes in a modest HPC cluster made up of 10 nodes.

This 2D simulation provides the designer a basic understanding about the behaviour of the device. However, in order to get a complete understanding of the device performance, a more realistic 3D simulation has to be carried out. In this case, the effect of the taper that adiabatically couples the light from the waveguide to the grating coupler must be included, so the dimensions of the simulation cell are increased up to 500x20x5 microns. For the same value of the resolution (25 nanometers), around 190 GB of memory is required, even exploiting the cell symmetries to reduce the computation size. So, in order to perform this kind of intensive simulations, the use of larger HPC cluster resources is needed.

A.3.2 Ring Resonators

An integrated optics ring resonator consists of a waveguide in a closed loop coupled to one or more input/output (or bus) waveguides as shown in Fig. A.3. Depending on the wavelength of the light and input waveguide used, constructive interference

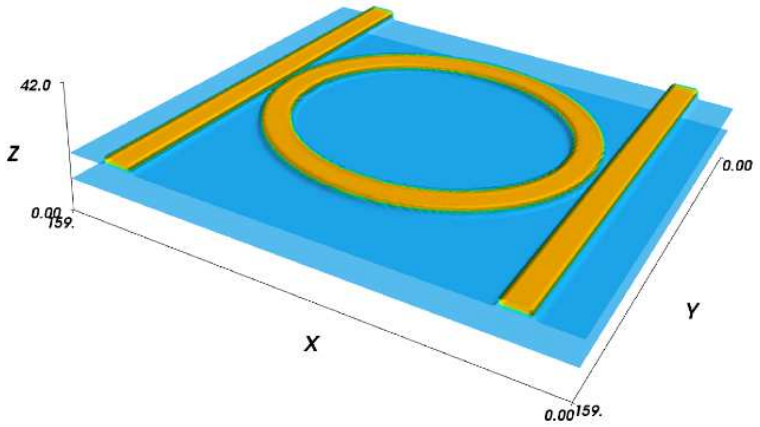

Figure A.3: 3D model of a ring resonator.

of the multiple round-trips within the ring happens at different output waveguides.

Devices composed of single or multiple micro ring resonator cavities can be exploited in a wide variety of classical applications including, amongst other: channel filtering in WDM systems [6], linear and nonlinear digital optics [8], optical buffering [51] and modulation [10], dispersion compensation [11], switching [12]. Furthermore, the range of applications can be extended to encompass the emergent field of quantum information processing [4]. Fig. A.4 shows a two-dimensional slice with a graphical representation of the electromagnetic fields inside the resonator. This problem was addressed with an HPC cluster with 100 nodes, cell size of 25x20x5 microns, grid resolution of 20 nanometers, total memory usage of 24 GB and solved in 59 hours.

Distributed Bragg Reflectors

Distributed Bragg Reflectors (DBRs) [118] in integrated optics are similar to Fiber Bragg Gratings (FBGs) [119] in optical fibers. These are key devices in optical networking, and used in a vast number of applications, ranging from simple WDM multi/demultiplexer to dispersion compensation. FBGs gratings are built in optical fibers by changing the refractive index in the core of fiber in a periodic fashion. The DBR is the integrated optics counterpart, and can be either a waveguide whose width is changed periodically between two values (uniform) or following a given pattern (apodized). Two examples of these are illustrated in Fig. A.5. Other DBRs are built keeping the waveguide width constant and slicing the waveguide

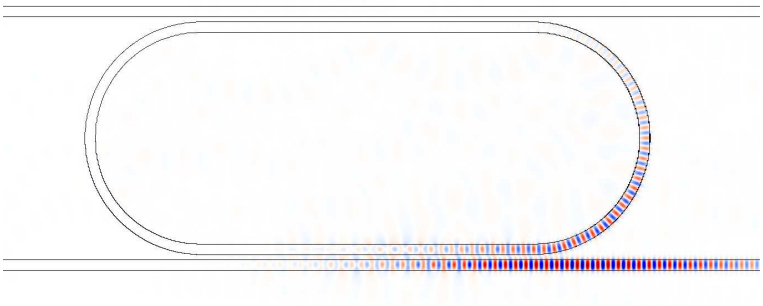

Figure A.4: Electromagnetic field representation in a racetrack resonator.

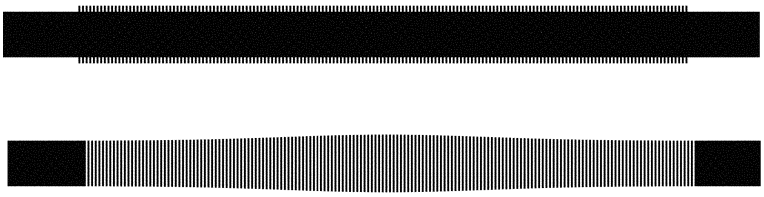

Figure A.5: Uniform and apodized DBRs.

vertically. When the slices do not go all through the waveguide height, FDTD is a handy and powerful tool to solve the problem, since an analytic approach might be complex and not precise. Fig. A.6 shows the spectral response of both uniform and apodized DBR filters calculated with MEEP. This problem was address with an HPC cluster with 50 nodes, cell size of 100x5x5 microns, grid resolution of 20 nanometers, total memory usage of 19 GB and solved in 30 hours.

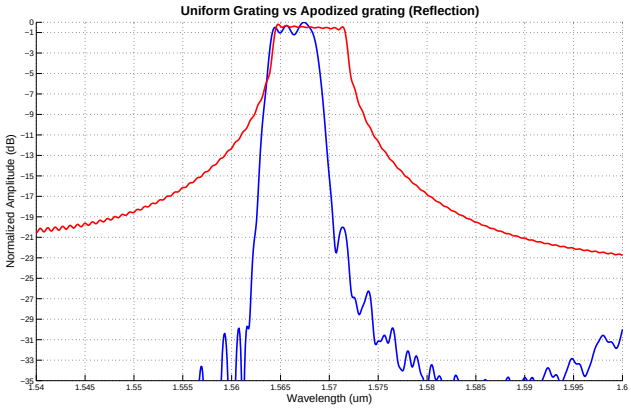

Figure A.6: Reflection spectrum of a uniform (red) and apodized (blue) DBR.

Appendix B
Characterization setup

The characterization of the fabricated devices was carried out in the facilities of the Optical and Quantum Communications Group from the Universitat Politècnica de València. The laboratory is equipped with state-of-the-art optical instrumentation as well as for RF. The bare-die characterization systems available at the time this thesis was written, allowed for butt-coupled chips characterization but not for vertical in/out coupling. In order to characterize the SOI devices provided with grating couplers, a vertical fiber setup was assembled. The reference setup employed was the one from the imec group from University of Gent in Belgium. The schematic of the setup is shown in Fig.B.1.

The setup, placed on top of a suspended table that absorbs the vibrations and eases the placement of components, will be detailed part by part. The most important components are pair of 3-axis nanopositioning stages as shown in Fig. B.3 where custom 10 degrees angled supports where placed. The fibers must have an inclination of 10 degrees with respect to vertical in order to maximize the coupling efficiency to the grating couplers and to minimize reflections into the fibers. This two stages will hold and position the input and output fiber with the required accuracy on top on the chip. In the middle of this two stages, another 3-axis stage was located in order to place the chip and it is shown in Fig. B.4. The chips are mounted on top of a vacuum chuck to avoid vibrations and undesired movements of the chips while performing the characterization.

To place the fibers in the appropriate position of the grating couplers, a microscope camera was added to the system (Fig.B.6). This vision system is comprised of a common CCTV color camera with an extension tube and a microscope objective chosen appropriately to provide the system the required magnification. The Field of View (FOV) of the system is approximately 500 x 800 microns. The vision system includes a 3 axis motorized stage for the displacement of the camera over the chip under test. The last component of the vision system is an LCD monitor placed inside the setup and used to show the camera images. In Fig.B.7 the image of a chip and the input and output fiber placed on top of it is shown. The inclina-

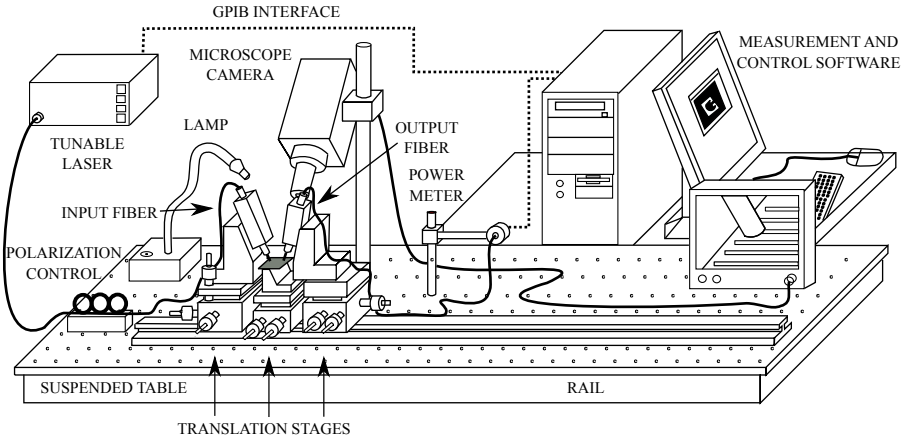

Figure B.1: Vertical fiber setup schematic

tion of the camera and the illumination system allows for an easy alignment in the vertical axis. The fibers produce a shadow that can be used as a reference in the vertical plane. When the fiber and its shadow are coincident, one can assume that the height is the appropriate for the measure, meaning that the fiber is almost touching the surface of the chip.

Every nanopositiong stage is mounted on top of rail to facilitate the movement and ensure the alignment of the different positioners. The full assembled setup is shown in Fig.B.2. All the components are assembled into a clean vault in order to keep dust clean the system. Also reduces the fiber vibrations induced by air currents. Fig.B.5 shows a closer look to the fibers located on top of the chip for the characterization.

Figure B.2: Vertical fiber setup

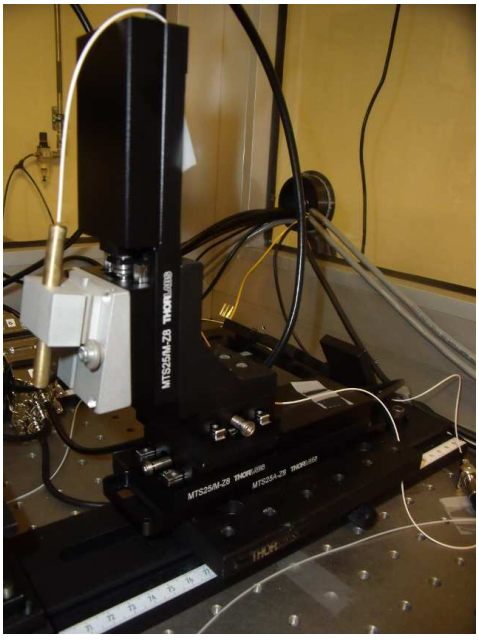

Figure B.3: 3-axis positioner with angled fiber support

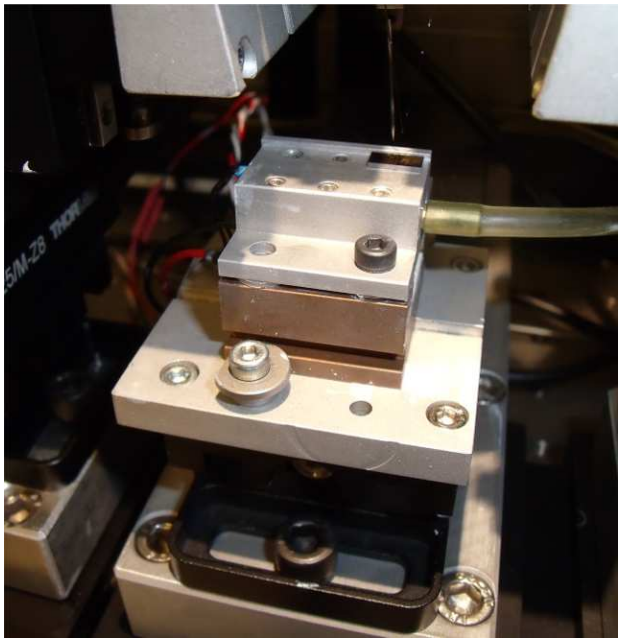

Figure B.4: Vacuum chuck

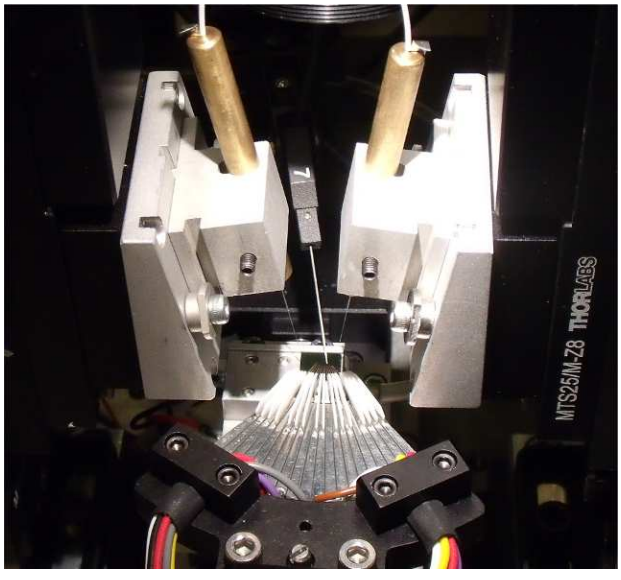

Figure B.5: Detail of the vertical fibers coupled to the chip

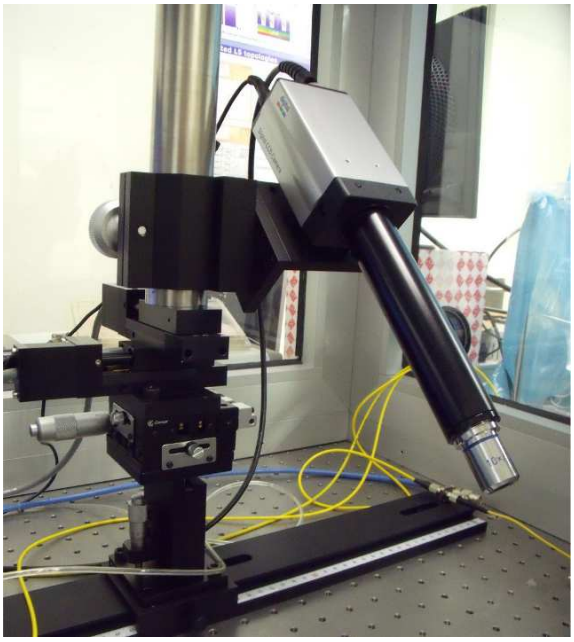

Figure B.6: Video camera with microscope objective

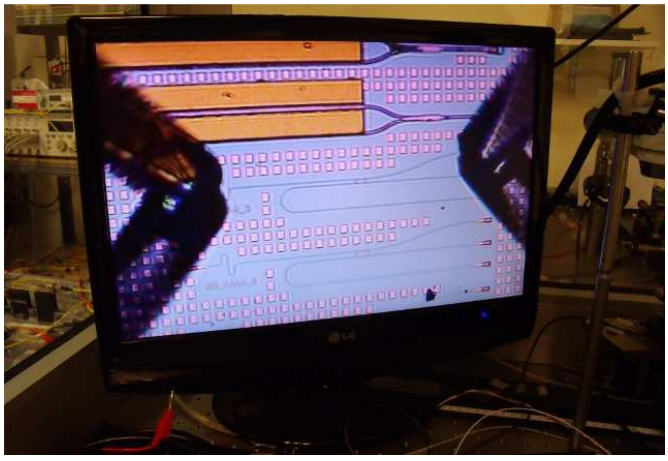

Figure B.7: LCD monitor showing the chip and fiber images.

Appendix C
List of publications

C.1 SCI Journal papers

1. J. Capmany, P. Muñoz, J. D. Doménech, and M. A. Muriel, "Apodized coupled resonator waveguides," *Optics Express*, vol. 15, no. 16, pp. 10196–10206, 2007.

2. J. D. Doménech, P. Muñoz, and J. Capmany, "The longitudinal offset technique for apodization of coupled resonator optical waveguide devices: concept and fabrication tolerance analysis," *Optics Express*, vol. 17, no. 23, pp. 21050–21059, 2009.

3. P. Muñoz, J. D. Doménech, and J. Capmany, "Synthesis of coupled resonator optical waveguides by cavity aggregation," *Optics Express*, vol. 18, no. 2, pp. 1600–160, 2010.

4. J. D. Doménech, P. Muñoz, and J. Capmany, "Transmission and group-delay characterization of coupled resonator optical waveguides apodized through the longitudinal offset technique," *Optics Letters*, vol. 36, pp. 136–138, 2011.

5. P. Muñoz, R. Garcia-Olcina, C. Habib, L. R. Chen, X. J. M. Leijtens, J. D. Doménech, M. Rius, J. Capmany, T. De Vries, M. J. R. Heck, L. Augustin, R. Notzel, and D. Robbins, "Multi-wavelength laser based on an Arrayed Waveguide Grating and Sagnac loop reflectors monolithically integrated on InP," *IET Optoelectronics*, vol. 5, 2011.

6. E. Xifre, J. D. Doménech, R. Fenollosa, P. Muñoz, J. Capmany, and F. Meseguer, "All silicon waveguide spherical microcavity device," *Optics Express*, vol. 19, pp. 3185–3192, 2011.

7. J. S. Fandiño, J. D. Doménech, P. Muñoz, and J. Capmany, "Integrated InP frequency discriminator for Phase-modulated microwave photonic links," *Opt. Express*, vol. 21, pp. 3726–3736, Feb 2013.

C.2 Conference papers

1. P. Muñoz, J. D. Doménech, M. D. Manzanedo, J. H. den Besten, and J. Capmany, "Design of arrayed waveguide sagnac interferometers for OTDM-WDM optical networks," in *Proc. of the V Reunion Española de Optoelectrónica, OPTOEL 2007*, pp. 99–104, 2007.

2. J. D. Doménech, P. Muñoz, and J. Capmany, "Apodized chirped coupled resonator optical waveguides," in *Proc. of the 10th anniversary international conference on transparent optical networks, ICTON, Vol. 4*, pp. 250–253, 2008.

3. J. D. Doménech, R. Garcia-Olcina, P. Muñoz, and J. Capmany, "Integrated optics devices modelling using High Performance Computing and parallel Finite Differences in the Time Domain algorithms," in *Proc. of the 3rd Iberian Grid Infrastructure Conference, IBERGRID 2009*, pp. 1–9, 2009.

4. J. D. Doménech, P. Muñoz, and J. Capmany, "Tunable microwave photoni phase shifter using an all-pass ring resonator filter," in *Proc. of the VI Reunion Española de Optoelectrónica, OPTOEL 2009*, pp. 159–163, 2009.

5. R. Garcia-Olcina, J. D. Doménech, P. Muñoz, and J. Capmany, "Apodized grating couplers in Silicon-On-Insulator," in *Proc. of the VI Reunion Española de Optoelectrónica, OPTOEL 2009*, pp. 65–68, 2009.

6. P. Muñoz, R. Garcia-Olcina, J. D. Doménech, M. Rius, J. Capmany, L. R. Chen, C. Habib, X. J. M. Leijtens, T. de Vries, M. J. R. Heck, L. M. Augustin, R. Notzel, and D. J. Robbins, "Multi-wavelength laser based on an arrayed waveguide grating and Sagnac loop reflectors monolithically integrated on InP," in *Proc. Of the European Conference on Integrated Optics (ECIO), Cambridge,(U.K.)*, 2010.

7. J. D. Doménech, M. Rius, J. Mora, P. Muñoz, and J. Capmany, "Microwave photonics beamformer based on ring resonators and arrayed waveguide gratings," in *Proc. Of the European Conference on Integrated Optics (ECIO), Cambridge,(U.K.)*, 2010.

8. P. Muñoz, R. Garcia-Olcina, J. D. Doménech, M. Rius, J. Sancho, J. Capmany, L. R. Chen, C. Habib, X. J. M. Leijtens, T. de Vries, M. J. R. Heck, L. M. Augustin, R. Notzel, and D. J. Robbins, "InP monolithically integrated label swapper device for spectral amplitude coded optical packet networks," in *Postdealine Paper, presented at the European Conference on Integrated optics ECIO 2010, Cambridge, UK*, 2010.

9. J. D. Doménech, M. Rius, P. Muñoz, and J. Capmany, "Apodized coupled resonator optical waveguides using the longitudinal offset technique," in *Proc. of the European Conference on Integrated Optics (ECIO), Cambridge,(U.K.)*, 2010.

10. E. Xifre, R. Fenollosa, J. D. Doménech, M. Rius, P. Muñoz, J. Capmany, and F. Meseguer, "All silicon waveguide spherical microcavity device," in *Proc. Of the European Conference on Integrated optics (ECIO), Cambridge,(U.K.)*, 2010.

11. J. D. Doménech, P. Muñoz, and J. Capmany, "Apodization of coupled resonator optical waveguide devices through a longitudinal offset technique," in *Proc. of the SPIE Photonics Europe 2010, Brussels,(BE)*, 2010.

12. J. D. Doménech, P. Muñoz, and J. Capmany, "Discretely tunable microwave photonics beamformer based on ring resonators and arrayed waveguide gratings," in *Proc. of the SPIE Photonics Europe 2010, Brussels,(BE)*, 2010.

13. J. D. Doménech, P. Muñoz, and J. Capmany, "Experimental demonstration of the longitudinal offset technique for the apodization of coupled resonator optical waveguide devices," in *Lasers and Electro-Optics/Quantum Electronics and Laser Science Conference: 2010 Laser Science to Photonic Applications, CLEO/QELS 2010, art. no. 5500898, (2010)*, 2010.

14. E. Xifre, J. D. Doménech, R. Fenollosa, P. Muñoz, J. Capmany, and F. Meseguer, "Add-drop filter based on silicon spherical microcavities," in *Conferencia Española de Nanofotonica (CEN 2010)*, 2010.

15. J. D. Doménech, P. Muñoz, R. Garcia-Olcina, X. Leijtens, D. Robbins, T. Vries, and J. Capmany, "Design and fabrication of a narrow band phase shift enabled optical beamformer monolithically integrated on InP," in *Proc. of the VII Reunion Española de Optoelectrónica, OPTOEL 2011*, pp. 1–4, 2011.

16. J. D. Doménech, P. Muñoz, I. Artundo, J. Capmany, P. Dumon, and W. Bogaerts, "Design, fabrication and characterization of a narrow bandwidth microwave photonics beamformer in a SOI platform," in *Proc. of the 16th European Conference on Integrated Optics (ECIO), Sitges,(Spain)*, 2012.

17. J. S. Fandiño, J. D. Doménech, P. Muñoz, and J. Capmany, "Design and experimental characterization of an InP photonic integrated circuit working as a receiver for frequency-modulated direct-detection microwave photonic links," in *Proc. of SPIE Integrated Optics: Devices, Materials, and Technologies XVII*, pp. 862708–862708–8, 2013.

C.3 Papers in other journals

1. P. Muñoz, J. D. Doménech, . Zheng Lu, C. Habib, and J. Capmany, "Multifunctional optical devices and subsystems integrated on a chip," *Waves*, vol. 1, 2009.

2. P. Muñoz, J. D. Doménech, A. I, C. Habib, X. J. M. Leijtens, T. De Vries, D. Robbins, J. H. Den Besten, L. R. Chen, and J. Capmany, "Application specific photonic integrated circuits through generic integration, a novel paradigm in photonics," *Waves*, vol. 3, 2011.

Bibliography

[1] R. G. Hunsperger, *Integrated Optics*. Springer Verlag, 5th ed., September 2002.

[2] C. Dragone, "An N*N optical multiplexer using a planar arrangement of two star couplers," *Photonics Technology Letters*, vol. 3, pp. 812–815, Sept. 1991.

[3] B. Little, S. Chu, H. Haus, J. Foresi, and J.-P. Laine, "Microring resonator channel dropping filters," *Journal of Lightwave Technology*, vol. 15, pp. 998–1005, June 1997.

[4] K. Vahala, "Optical microcavities," *Nature*, vol. 424, pp. 839–846, 2003.

[5] C. K. Madsen and G. Lenz, "Optical all-pass filters for phase response design with applications for dispersion compensation," *IEEE Photonics Technology Letters*, vol. 10, pp. 994–996, July 1998.

[6] J. Capmany and M. Muriel, "A new transfer matrix formalism for the analysis of fiber ring resonators: compound coupled structures for FDMA demultiplexing," *Journal of Lightwave Technology*, vol. 8, pp. 1904–1919, Dec. 1990.

[7] J. Lloret, J. Sancho, M. Pu, I. Gasulla, K. Yvind, S. Sales, and J. Capmany, "Tunable complex-valued multi-tap microwave photonic filter based on single silicon-on-insulator microring resonator," *Opt. Express*, vol. 19, pp. 12402–12407, Jun 2011.

[8] V. Van, T. Ibrahim, P. Absil, F. Johnson, R. Grover, and P.-T. Ho, "Optical signal processing using nonlinear semiconductor microring resonators," *Selected Topics in Quantum Electronics, IEEE Journal of*, vol. 8, pp. 705–713, May/Jun 2002.

[9] F. Xia, L. Sekaric, and Y. Vlasov, "Ultra compact optical buffers on a silicon chip," *Nature Photonics*, vol. 1, pp. 65–71, 2007.

[10] H. Tazawa and W. Steier, "Analysis of ring resonator-based traveling-wave modulators," *Photonics Technology Letters, IEEE*, vol. 18, pp. 211–213, 1, 2006.

[11] C. Madsen, G. Lenz, A. Bruce, M. Cappuzzo, L. Gomez, and R. Scotti, "Integrated all-pass filters for tunable dispersion and dispersion slope compensation," *Photonics Technology Letters, IEEE*, vol. 11, pp. 1623–1625, Dec 1999.

[12] B. Little, S. Chu, W. Pan, and Y. Kokubun, "Microring resonator arrays for VLSI photonics," *Photonics Technology Letters, IEEE*, vol. 12, pp. 323–325, Mar 2000.

[13] J. E. Heebner, R. W. Boyd, and Q.-H. Park, "SCISSOR solitons and other novel propagation effects in microresonator-modified waveguides," *J. Opt. Soc. Am. B*, vol. 19, no. 4, pp. 722–731, 2002.

[14] A. Yariv, Y. Xu, R. K. Lee, and A. Scherer, "Coupled-resonator optical waveguide: a proposal and analysis," *Optics Letters*, vol. 24, no. 11, pp. 711–713, 1999.

[15] P. Cross and H. Kogelnik, "Sidelobe supression in corrugated-waveguide filters," *Optics letters*, vol. 1, pp. 43–45, 1977.

[16] E. Wooten, K. Kissa, A. Yi-Yan, E. Murphy, D. Lafaw, P. Hallemeier, D. Maack, D. Attanasio, D. Fritz, G. McBrien, and D. Bossi, "A review of lithium niobate modulators for fiber-optic communications systems," *Selected Topics in Quantum Electronics, IEEE Journal of*, vol. 6, no. 1, pp. 69–82, 2000.

[17] G. Maxwell and B. J. Ainslie, "Demonstration of a directly written directional coupler using uv-induced photosensitivity in a planar silica waveguide," *Electronics Letters*, vol. 31, no. 2, pp. 95–96, 1995.

[18] Y. Hibino, F. Hanawa, H. Nakagome, M. Ishii, and N. Takato, "High reliability optical splitters composed of silica-based planar lightwave circuits," *Lightwave Technology, Journal of*, vol. 13, no. 8, pp. 1728–1735, 1995.

[19] Y. Hibino, T. Kitagawa, K. Hill, F. Bilodeau, B. Malo, J. Albert, and D. Johnson, "Wavelength division multiplexer with photoinduced bragg gratings fabricated in a planar-lightwave-circuit-type asymmetric mach-zehnder interferometer on si," *Photonics Technology Letters, IEEE*, vol. 8, no. 1, pp. 84–86, 1996.

[20] H. Takahashi, S. Suzuki, K. Kato, and I. Nishi, "Arrayed-waveguide grating for wavelength division multi/demultiplexer with nanometre resolution," *Electronics letters*, vol. 26, no. 2, pp. 87–88, 1990.

[21] X. Duan, Y. Huang, Y. Cui, J. Wang, and C. M. Lieber, "Indium phosphide nanowires as building blocks for nanoscale electronic and optoelectronic devices," *Nature*, vol. 409, no. 6816, pp. 66–69, 2001.

[22] R. Nagarajan and M. Smit, "Photonic integration," *IEEE LEOS Newsletter*, vol. 21, no. 3, pp. 4–10, 2007.

[23] G. T. Reed, *Silicon Photonics: The State of the Art*. John Wiley & Sons, Ltd, 2008.

[24] "ePIXfab, the European Silicon Photonics Platform." http://www.epixfab.eu/.

[25] "Optoelectronic System Integration in Silicon." http://opsisfoundry.org/.

[26] "Joint European Platform for InP-based Photonic Integrated Components and Circuits (JePPIX).." http://www.jeppix.eu/.

[27] "LioniX, microfluidics and integrated optics." http://www.lionixbv.nl/.

[28] "PhoeniX B.V, solutions for micro and nano technologies." http://www.phoenixbv.com/.

[29] "Interuniversity microelectronics centre." http://www.imec.be/.

[30] "Laboratoire d'électronique des technologies de l'information." http://www-leti.cea.fr/.

[31] "IHP - Innovations for High Performance Microelectronics." http://www.ihp-microelectronics.com/.

[32] A. Oppenheim, R. Schafer, and J. Buck, *Discrete-time signal processing*. Prentice-Hall, 1999.

[33] D. Pastor, J. Capmany, B. Ortega, V. Tatay, and J. Marti, "Design of apodised linearly chirped fiber gratings for dispersion compensation," *Journal of Lightwave Technology*, vol. 14, pp. 2581–2588, 1996.

[34] J. Capmany, M. Muriel, and S. Sales, "Highly accurate synthesis of fiber and waveguide Bragg gratings by an impedance reconstruction layer-aggregation method," *Quantum Electronics, IEEE Journal of*, vol. 43, pp. 889–898, Oct. 2007.

[35] S. Somekh, E. Garmire, A. Yariv, H. Garvin, and R. Hunsperger, "Channel optical waveguide directional couplers," *Applied Physics Letters*, vol. 22, no. 1, pp. 46–47, 1973.

[36] A. Yariv, "Universal relations for coupling of optical power between microresonators and dielectric waveguides," *Electronics Letters*, vol. 36, no. 4, pp. 321–322, 2000.

[37] J. E. Heebner, P. Chak, S. Pereira, J. E. Sipe, and R. W. Boyd, "Distributed and localized feedback in microresonator sequences for linear and nonlinear optics," *J. Opt. Soc. Am. B*, vol. 21, no. 10, pp. 1818–1832, 2004.

[38] J. Poon, J. Scheuer, S. Mookherjea, G. Paloczi, Y. Huang, and A. Yariv, "Matrix analysis of microring coupled resonator optical waveguides," *Optics Express*, vol. 12, pp. 90–103, Jan. 2004.

[39] C. K. Madsen and J. Zhao, *Optical Filter Design and Analysis: A Signal Processing Approach*. New York, NY, USA: John Wiley & Sons, Inc., 1st ed., 1999.

[40] Y. Landobasa and M. Chin, "Defect modes in micro-ring resonator arrays," *Optics Express*, vol. 13, pp. 7800–7815, 2005.

[41] E. Peral, J. Capmany, and J. Marti, "Iterative solution to the Gel'Fand-Levitan-Marchenko coupled equations and application to synthesis of fiber gratings," *Quantum Electronics, IEEE Journal of*, vol. 32, pp. 2078–2084, Dec 1996.

[42] R. Feced, M. Zervas, and M. Muriel, "An efficient inverse scattering algorithm for the design of nonuniform fiber Bragg gratings," *Quantum Electronics, IEEE Journal of*, vol. 35, pp. 1105–1115, Aug 1999.

[43] L. Poladian, "Simple grating synthesis algorithm," *Opt. Lett.*, vol. 25, no. 11, pp. 787–789, 2000.

[44] J. Skaar, L. Wang, and T. Erdogan, "On the synthesis of fiber Bragg gratings by layer peeling," *Quantum Electronics, IEEE Journal of*, vol. 37, pp. 165–173, Feb 2001.

[45] J. Skaar, L. Wang, and T. Erdogan, "Synthesis of thick optical thin-film filters with a layer-peeling inverse-scattering algorithm," *Appl. Opt.*, vol. 40, no. 13, pp. 2183–2189, 2001.

[46] A. Rosenthal and M. Horowitz, "Inverse scattering algorithm for reconstructing strongly reflecting fiber Bragg gratings," *Quantum Electronics, IEEE Journal of*, vol. 39, pp. 1018–1026, Aug. 2003.

[47] Y. Landobasa, S. Darmawan, and M.-K. Chin, "Matrix analysis of 2-D microresonator lattice optical filters," *Quantum Electronics, IEEE Journal of*, vol. 41, pp. 1410–1418, Nov. 2005.

[48] D. L. MacFarlane and E. M. Dowling, "Z-domain techniques in the analysis of Fabry-Perot étalons and multilayer structures," *J. Opt. Soc. Am. A*, vol. 11, no. 1, pp. 236–245, 1994.

[49] A. Melloni and M. Martinelli, "Synthesis of direct-coupled-resonators bandpass filters for WDM systems," *Lightwave Technology, Journal of*, vol. 20, pp. 296–303, Feb 2002.

[50] R. Orta, P. Savi, R. Tascone, and D. Trinchero, "Synthesis of multiple-ring-resonator filters for optical systems," *Photonics Technology Letters, IEEE*, vol. 7, pp. 1447–1449, Dec. 1995.

[51] F. Xia, M. Rooks, L. Sekaric, and Y. Vlasov, "Ultra-compact high order ring resonator filters using submicron silicon photonic wires for on-chip optical interconnects," *Optics Express*, vol. 15, no. 19, pp. 11934–11941, 2007.

[52] K. Ebeling, *Integrated Optoelectronics*. Springer-Verlag, 1993.

[53] H. Yamada, T. Chu, S. Ishida, and Y. Arakawa, "Si photonic wire waveguide devices," *Selected Topics in Quantum Electronics, IEEE Journal of*, vol. 12, no. 6, pp. 1371–1379, 2006.

[54] Y. Shi, S. He, and S. Anand, "Ultracompact directional couplers realized in inp by utilizing feature size dependent etching," *Opt. Lett.*, vol. 33, pp. 1927–1929, Sep 2008.

[55] F. Xia, L. Sekaric, and Y. A. Vlasov, "Mode conversion losses in silicon-on-insulator photonic wire based racetrack resonators," *Optics Express*, vol. 14, no. 9, pp. 3872–3886, 2006.

[56] A. Yen, A. Tritchkov, J. P. Stirniman, G. Vandenberghe, R. Jonckheere, K. Ronse, and L. Van den hove, "Characterization and correction of optical proximity effects in deep ultraviolet lithography using behavior modeling," *Journal of Vacuum Science Technology B: Microelectronics and Nanometer Structures*, vol. 14, no. 6, pp. 4175–4178, 1996.

[57] M. Popovic, C. Manolatou, and M. Watts, "Coupling-induced resonance frequency shifts in coupled dielectric multi-cavity filters," *Opt. Express*, vol. 14, pp. 1208–1222, Feb 2006.

[58] S. Selvaraja, W. Bogaerts, P. Dumon, D. Van Thourhout, and R. Baets, "Subnanometer linewidth uniformity in silicon nanophotonic waveguide devices using cmos fabrication technology," *Selected Topics in Quantum Electronics, IEEE Journal of*, vol. 16, no. 1, pp. 316–324, 2010.

[59] W. Bogaerts, R. Baets, P. Dumon, V. Wiaux, S. Beckx, D. Taillaert, B. Luyssaert, J. V. Campenhout, P. Bienstman, and D. V. Thourhout, "Nanophotonic waveguides in Silicon-on-Insulator fabricated with CMOS technology," *Journal of Lightwave Technology*, vol. 23, no. 1, p. 401, 2005.

[60] K. Saitoh and M. Koshiba, "Full-vectorial finite element beam propagation method with perfectly matched layers for anisotropic optical waveguides," *J. Lightwave Technol.*, vol. 19, p. 405, Mar 2001.

[61] D. Geuzebroek and A. Driessen, *Ring-Resonator-Based Wavelength Filters*, vol. 123 of *Springer Series in Optical Sciences*. Springer Berlin Heidelberg, 2006.

[62] W. W. Hu, K. Sarveswaran, M. Lieberman, and G. H. Bernstein, "Sub-10 nm electron beam lithography using cold development of poly(methylmethacrylate)," *Journal of Vacuum Science & Technology B: Microelectronics and Nanometer Structures*, vol. 22, no. 4, pp. 1711–1716, 2004.

[63] T. Barwicz, M. A. Popović, M. R. Watts, P. T. Rakich, E. P. Ippen, and H. I. Smith, "Fabrication of add-drop filters based on frequency-matched microring resonators," *J. Lightwave Technol.*, vol. 24, p. 2207, May 2006.

[64] S. Selvaraja, P. Jaenen, W. Bogaerts, D. Van Thourhout, P. Dumon, and R. Baets, "Fabrication of photonic wire and crystal circuits in Silicon-on-Insulator using 193-nm optical lithography," *Lightwave Technology, Journal of*, vol. 27, no. 18, pp. 4076–4083, 2009.

[65] T. Spuesens, L. Liu, T. De Vries, P. Romeo, P. Regreny, and D. Van Thourhout, "Improved design of an inp-based microdisk laser heterogeneously integrated with SOI," in *Group IV Photonics, 2009. GFP 09. 6th IEEE International Conference on*, pp. 202–204, 2009.

[66] K. Yamada, *Silicon Photonic Wire Waveguides: Fundamentals and Applications*, vol. 119 of *Topics in Applied Physics*. Springer Berlin Heidelberg, 2011.

[67] P. Dumon, W. Bogaerts, V. Wiaux, J. Wouters, S. Beckx, J. Van Campenhout, D. Taillaert, B. Luyssaert, P. Bienstman, D. Van Thourhout, and R. Baets, "Low-loss soi photonic wires and ring resonators fabricated with deep uv lithography," *Photonics Technology Letters, IEEE*, vol. 16, no. 5, pp. 1328–1330, 2004.

[68] S. Lardenois, D. Pascal, L. Vivien, E. Cassan, S. Laval, R. Orobtchouk, M. Heitzmann, N. Bouzaida, and L. Mollard, "Low-loss submicrometer silicon-on-insulator rib waveguides and corner mirrors," *Opt. Lett.*, vol. 28, pp. 1150–1152, Jul 2003.

[69] Q. Xu, D. Fattal, and R. G. Beausoleil, "Silicon microring resonators with 1.5-μm radius," *Opt. Express*, vol. 16, pp. 4309–4315, Mar 2008.

[70] K. D. Vos, I. Bartolozzi, E. Schacht, P. Bienstman, and R. Baets, "Silicon-on-insulator microring resonator forsensitive and label-free biosensing," *Opt. Express*, vol. 15, pp. 7610–7615, Jun 2007.

[71] "MPB, The MIT Photonic Bands." http://ab-initio.mit.edu/wiki/index.php/MIT_Photonic_Bands.

[72] E. Dulkeith, F. Xia, L. Schares, W. M. J. Green, and Y. A. Vlasov, "Group index and group velocity dispersion in silicon-on-insulator photonic wires," *Opt. Express*, vol. 14, no. 9, pp. 3853–3863, 2006.

[73] S. Darmawan and M. K. Chin, "Critical coupling, oscillation, reflection, and transmission in optical waveguide-ring resonator systems," *J. Opt. Soc. Am. B*, vol. 23, pp. 834–841, May 2006.

[74] R. Fortenberry, "Enhanced wavelength resolution chromatic dispersion measurements using fixed sideband technique," in *Optical Fiber Communication Conference, 2000*, vol. 1, pp. 107–109 vol.1, 2000.

[75] D. Taillaert, F. V. Laere, M. Ayre, W. Bogaerts, D. V. Thourhout, P. Bienstman, and R. Baets, "Grating couplers for coupling between optical fibers and nanophotonic waveguides," *Japanese Journal of Applied Physics*, vol. 45, no. 8A, pp. 6071–6077, 2006.

[76] J. Capmany, P. Munoz, J. D. Domenech, and M. A. Muriel, "Apodized coupled resonator waveguides," *Optics Express*, vol. 15, pp. 10196–10206, Aug. 2007.

[77] F. Morichetti, A. Canciamilla, M. Martinelli, A. Samarelli, R. M. D. L. Rue, M. Sorel, and A. Melloni, "Coherent backscattering in optical microring resonators," *Applied Physics Letters*, vol. 96, no. 8, p. 081112, 2010.

[78] J. Scheuer, J. K. S. Poon, G. T. Paloczi, and A. Yariv, "Coupled resonator optical waveguides (crow)," *Proc. SPIE 5735, Advanced Optical and Quantum Memories and Computing II*, pp. 52–59, 2005.

[79] R. Tucker, P.-C. Ku, and C. Chang-Hasnain, "Slow-light optical buffers: capabilities and fundamental limitations," *Lightwave Technology, Journal of*, vol. 23, no. 12, pp. 4046–4066, 2005.

[80] N. Fontaine, J. Yang, Z. Pan, S. Chu, W. Chen, B. E. Little, and S. J. B. Yoo, "Continuously tunable optical buffering at 40 gb/s for optical packet switching networks," *J. Lightwave Technol.*, vol. 26, pp. 3776–3783, Dec 2008.

[81] L. Y. Mario and M. K. Chin, "Optical buffer with higher delay-bandwidth product in a two-ring system," *Opt. Express*, vol. 16, pp. 1796–1807, Feb 2008.

[82] J. Capmany and D. Novak, "Microwave photonics combines two worlds," *Nature Photonics*, vol. 1, pp. 319–330, 2007.

[83] D. Marpaung, C. Roeloffzen, R. Heideman, A. Leinse, S. Sales, and J. Capmany, "Integrated microwave photonics," *Laser & Photonics Reviews*, pp. n/a–n/a, 2013.

[84] R. Adar, M. Serbin, and V. Mizrahi, "Less than 1 db per meter propagation loss of silica waveguides measured using a ring resonator," *Lightwave Technology, Journal of*, vol. 12, no. 8, pp. 1369–1372, 1994.

[85] B. Howley, Y. Chen, X. Wang, Q. Zhou, Z. Shi, Y. Jiang, and R. T. Chen, "2-bit reconfigurable true time delay lines using 2× 2 polymer waveguide switches," *Photonics Technology Letters, IEEE*, vol. 17, no. 9, pp. 1944–1946, 2005.

[86] G. Lenz, B. Eggleton, C. K. Madsen, and R. Slusher, "Optical delay lines based on optical filters," *Quantum Electronics, IEEE Journal of*, vol. 37, no. 4, pp. 525–532, 2001.

[87] M. Rasras, C. Madsen, M. Cappuzzo, E. Chen, L. Gomez, E. Laskowski, A. Griffin, A. Wong-Foy, A. Gasparyan, A. Kasper, J. Le Grange, and S. Patel, "Integrated resonance-enhanced variable optical delay lines," *Photonics Technology Letters, IEEE*, vol. 17, no. 4, pp. 834–836, 2005.

[88] L. Zhuang, C. G. H. Roeloffzen, R. Heideman, A. Borreman, A. Meijerink, and W. van Etten, "Single-chip ring resonator-based 1 times; 8 optical beam forming network in cmos-compatible waveguide technology," *Photonics Technology Letters, IEEE*, vol. 19, no. 15, pp. 1130–1132, 2007.

[89] A. Melloni, F. Morichetti, C. Ferrari, and M. Martinelli, "Continuously tunable 1 byte delay in coupled-resonator optical waveguides," *Opt. Lett.*, vol. 33, pp. 2389–2391, Oct 2008.

[90] J. Cardenas, M. A. Foster, N. Sherwood-Droz, C. B. Poitras, H. L. R. Lira, B. Zhang, A. L. Gaeta, J. B. Khurgin, P. Morton, and M. Lipson, "Wide-bandwidth continuously tunable optical delay line using silicon microring resonators," *Opt. Express*, vol. 18, pp. 26525–26534, Dec 2010.

[91] P. Morton, J. Cardenas, J. Khurgin, and M. Lipson, "Fast thermal switching of wideband optical delay line with no long-term transient," *Photonics Technology Letters, IEEE*, vol. 24, no. 6, pp. 512–514, 2012.

[92] Q. Chang, Q. Li, Z. Zhang, M. Qiu, T. Ye, and Y. Su, "A tunable broadband photonic rf phase shifter based on a silicon microring resonator," *Photonics Technology Letters, IEEE*, vol. 21, no. 1, pp. 60–62, 2009.

[93] W. Xue, S. Sales, J. Capmany, and J. Mørk, "Microwave phase shifter with controllable power response based on slow-and fast-light effects in semiconductor optical amplifiers," *Optics letters*, vol. 34, no. 7, pp. 929–931, 2009.

[94] W. Xue, S. Sales, J. Capmany, and J. Mørk, "Wideband 360 microwave photonic phase shifter based on slow light in semiconductor optical amplifiers," *Opt. Express*, vol. 18, no. 6, pp. 6156–6163, 2010.

[95] J. Lloret, G. Morthier, F. Ramos, S. Sales, D. V. Thourhout, T. Spuesens, N. Olivier, J.-M. Fédéli, and J. Capmany, "Broadband microwave photonic fully tunable filter using a single heterogeneously integrated iii-v/soi-microdisk-based phase shifter," *Opt. Express*, vol. 20, pp. 10796–10806, May 2012.

[96] P. Morton and J. Khurgin, "Microwave photonic delay line with separate tuning of the optical carrier," *Photonics Technology Letters, IEEE*, vol. 21, no. 22, pp. 1686–1688, 2009.

[97] S. Chin, L. Thévenaz, J. Sancho, S. Sales, J. Capmany, P. Berger, J. Bourderionnet, and D. Dolfi, "Broadband true time delay for microwave signal processing, using slow light based on stimulated brillouin scattering in optical fibers," *Opt. Express*, vol. 18, pp. 22599–22613, Oct 2010.

[98] M. Burla, D. Marpaung, L. Zhuang, C. Roeloffzen, M. R. Khan, A. Leinse, M. Hoekman, and R. Heideman, "On-chip cmos compatible reconfigurable optical delay line with separate carrier tuning for microwave photonic signal processing," *Opt. Express*, vol. 19, pp. 21475–21484, Oct 2011.

[99] M. Frankel, P. Matthews, R. Esman, and L. Goldberg, "Practical optical beamforming networks," *Optical and Quantum Electronics*, vol. 30, no. 11-12, pp. 1033–1050, 1998.

[100] D. Adams and C. Madsen, "A novel broadband photonic RF phase shifter," *IEEE Journal of Lightwave Technology*, vol. 26, no. 15, pp. 2712–2717, 2008.

[101] Q. Chang, Q. Li, Z. Zhang, M. Qiu, T. Ye, and Y. Su, "A tunable broadband photonic RF phase shifter based on a silicon microring resonator," *IEEE Photonics Technology Letters*, vol. 21, no. 1, pp. 60–62, 2009.

[102] G. Cocorullo and I. Rendina, "Thermo-optical modulation at 1.5 μm in silicon etalon," *Electronics Letters*, vol. 28, no. 1, pp. 83–85, 1992.

[103] V. Almeida and M. Lipson, "Optical bistability on a silicon chip," *Opt. Letters*, vol. 29, no. 20, pp. 2387–2389, 2004.

[104] J. D. Domenech, P. Muñoz, and J. Capmany, "Tunable microwave photonic phase shifter using an all-pass ring resonator filter," in *VI Reunion Española de Optoelectronica (OPTOEL 09)* (E. MALAGA, ed.), 2009.

[105] G. Alibert, F. Delorme, P. Boulet, J. Landreau, and H. Nakajima, "Subnanosecond tunable laser using a single electroabsorption tuning super structure grating," *IEEE Photonics Technology Letters*, vol. 9, no. 7, pp. 895–897, 1997.

[106] G. Meslener, "Chromatic dispersion induced distortion of modulated monochromatic light employing direct detection," *Quantum Electronics, IEEE Journal of*, vol. 20, pp. 1208–1216, Oct 1984.

[107] P. Munoz, J. D. Domenech, M. Manzanedo, J. Den Besten, E. Verdumen, and J. Capmany, "Design of arrayed waveguide sagnac interferometers for OTDM-WDM optical networks," *5th Reunión Española de Optoelectrónica*, 2007.

[108] S. Schelkunoff, "A mathematical theory of linear arrays," *Bell System Technical Journal*, vol. 22, no. 1, pp. 80–107, 1943.

[109] P. Munoz, D. Pastor, and J. Capmany, "Modeling and design of arrayed waveguide gratings," *IEEE Journal of Lightwave Technology*, vol. 20, no. 4, pp. 661–674, 2002.

[110] "Vpiphotonics." VPItransmissionMaker/VPIcomponentMaker Version 8.0, VPIsystems Inc., www.vpiphotonics.com.

[111] W. Bogaerts, P. Dumon, D. Van Thourhout, D. Taillaert, P. Jaenen, J. Wouters, S. Beckx, V. Wiaux, and R. Baets, "Compact wavelength-selective functions in silicon-on-insulator photonic wires," *Selected Topics in Quantum Electronics, IEEE Journal of*, vol. 12, pp. 1394 –1401, nov.-dec. 2006.

[112] D. Derickson, *Fiber Optic Test and Measurement*. Prentice Hall PTR, 1998.

[113] J. VanRoey, J. van derDonk, and P. E. Lagasse, "Beam-propagation method: analysis and assessment," *J. Opt. Soc. Am.*, vol. 71, pp. 803–810, Jul 1981.

[114] A. Taflove and S. C. Hagness, *Computational Electrodynamics: The Finite-Difference Time-Domain Method*. MA, 2000.

[115] A. Farjadpour, D. Roundy, A. Rodriguez, M. Ibanescu, P. Bermel, J. D. Joannopoulos, S. G. Johnson, and G. Burr, "Improving accuracy by subpixel smoothing," *Optical letters in press*, 2006.

[116] "MEEP, free finite-difference time-domain (FDTD) simulation software package developed at MIT." http://ab-initio.mit.edu/wiki/index.php/Meep.

[117] L. Vivien, D. Pascal, S. Lardenois, D. Marris-Morini, E. Cassan, F. Grillot, S. Laval, J.-M. Fédéli, and L. E. Melhaoui, "Light injection in soi microwaveguides using high-efficiency grating couplers," *J. Lightwave Technol.*, vol. 24, pp. 3810–3815, Oct 2006.

[118] K. J. Kasunic, "Design equations for the reflectivity of deep-etch distributed Bragg reflector gratings," *J. Lightwave Technol.*, vol. 18, p. 425, Mar 2000.

[119] F. Ouellette, "All-fiber filter for efficient dispersion compensation," *Opt. Lett.*, vol. 16, pp. 303–305, Mar 1991.